



McGlone, Andrew William (2019) *Polycrystalline diamond micro-electromechanical systems (MEMS) for passive micro-rheology and sensor applications*. PhD thesis.

<https://theses.gla.ac.uk/73011/>

Copyright and moral rights for this work are retained by the author

A copy can be downloaded for personal non-commercial research or study, without prior permission or charge

This work cannot be reproduced or quoted extensively from without first obtaining permission in writing from the author

The content must not be changed in any way or sold commercially in any format or medium without the formal permission of the author

When referring to this work, full bibliographic details including the author, title, awarding institution and date of the thesis must be given

Enlighten: Theses

<https://theses.gla.ac.uk/>
research-enlighten@glasgow.ac.uk

Polycrystalline Diamond Micro- Electromechanical Systems (MEMS) for Passive Micro-Rheology and Sensor Applications

By

Andrew William McGlone

September 2018

Submitted in fulfilment of the requirements for the
Degree of Doctor of Philosophy
to the
School of Engineering
University of Glasgow

In all chaos
There is a cosmos
In all disorder
A secret order

Carl Jung

Abstract

Owing to its unique mechanical and electrical properties, diamond is an attractive candidate for use in micro-electro-mechanical systems (MEMS) devices. This thesis pertains to the development, fabrication and characterisation of polycrystalline diamond (PCD) micro-electromechanical systems (MEMS) devices for passive micro-rheology and sensor applications. Intrinsic PCD and boron doped PCD (BDD) materials are investigated.

Micro-rheology is the study of soft matter rheological properties, often performed by observing interactions with mechanical devices, such as micro-cantilevers, at the micro scale. In order to overcome significant fluid dampening, these devices are actuated at or around their resonant frequency, and several measurements are taken at different frequencies to build a data set. We present an intrinsic diamond-based micro-cantilever micro-rheometer device, the passively actuated thermal fluctuations of which can be characterised in a fluid at least up to the viscosity of water (8.90×10^{-4} Pa.s). A possible data analysis method to extract a fluid's viscoelastic properties from the power spectrum of the thermal fluctuations of a device submerged in the fluid is also presented. This method negates the requirement for measurements at multiple actuation frequencies and provides useable data up to the sample rate of the data acquisition system.

Intrinsic PCD cantilevers for passive micro-rheology were fabricated from polished (~3 nm Ra) 500 nm thick PCD on Silicon <100> substrate films. Cantilever dimensions range from 5 μm to 150 μm in length and 1 μm to 4 μm in width, the highest height/width/length ratio cantilevers yet reported. PCD samples were patterned using electron beam lithography and highly anisotropic diamond etching was achieved using an RIE Ar/O₂ plasma etching method. A new fabrication process to minimize cantilever undercut is presented. The thermal fluctuations of the free-standing cantilever structures in air and water at room temperature were successfully captured by a laser Doppler vibrometer system. Resonant frequencies of devices are presented, ranging from 38 - 554 kHz in air and 42 - 148 kHz in water, comparable to that of similar single crystal diamond devices.

PCD micro-cantilevers have been investigated extensively in different sensor applications. Recently, boron-doped diamond micro cantilevers exhibiting piezoresistive behavior have been fabricated from multi-layer PCD material. We present a boron-doped PCD micro-cantilever piezoresistive sensor fabricated from a single layer of BDD thin film on silicon. BDD material was electrically characterised and found to be electrically stable for up to at least 60 seconds within the I/V ranges investigated. BDD micro-cantilevers were fabricated from polished (~3 nm Ra) 480 nm thick BDD on Silicon <100> substrate films. The U-shaped cantilever's dimensions ranged from 60 μm to 110 μm in length with legs 4 μm in width. The deflection sensitivity of the fabricated cantilever devices is reported, ranging from 0.029 $\text{m}\Omega/\Omega\text{-}\mu\text{m}$ to 0.063 $\text{m}\Omega/\Omega\text{-}\mu\text{m}$. An analysis of the nature of the piezoresistive mechanism in the BDD devices is presented.

Acknowledgements

There are countless people in my life that have helped and supported me on my journey over the last 4 years. I first would like to thank my family for their continued support. Mum & dad, Jo & Lesley, thank you for being there for me and I hope I have made you all proud.

I have been blessed with some of the best friends that anyone could ever wish for. In no particular order I would like to thank: Pete & Allan; my bandmates and brothers in arms. Thanks for all the pizza, gin & patter; Kev Lynch, I'm so pleased you're following in my electronic footsteps! Al Doherty, thank you for all the lunchtime food & therapy sessions, you have always been wise beyond your years. Rick, I'd never had made it this far without your help. Thank you all for putting up with me, particularly over the last year or so.

My partner Jesse, you've had to cope with the best and worst of me over the last 4 years. Thank you for your unflinching love and support.

I didn't expect to make many friends at university as a mature student, and how pleasant it was to be proven wrong - David, we made it! Good luck wherever your PhD takes you, I wish you the very best in life. Kev Crawford, your knowledge, experience and friendship made it so easy for David and I to get started 4 years ago, and for that I am eternally grateful.

Thank you to the technical staff at the JWNC for your expertise and professionalism, and thanks to Rab & Julien for all your help with measurements up on level 8.

Thank you to Dr Oliver Williams and the Diamond Foundry research group at Cardiff University for supplying material and providing invaluable feedback.

Finally, thank you to my supervisory team; Dave, Manlio & Phil.

Manlio, thank you for your patience in teaching and helping me understand micro-rheology. I enjoyed learning from you and will miss our engaging discussions.

Dave, you always knew exactly the right thing to say to get the best out of me, and that's what makes you a great supervisor. I feel privileged to have been a part of the N.E.D.D.S. group, but mainly to have been one of your students.

Conference Proceedings

McGlone, A. W., Williams, O. A., Tassieri, M, Dobson, P and Moran, D. A. J.

Investigation into the Minimum Feature Size for Reactive-Ion Etched (RIE) Micro and Nano-Scale Polycrystalline Diamond Mechanical Resonators

Poster, MRS Fall Meeting: Materials Research Society, Boston MA, USA, 29 Nov - 4 Dec 2015

McGlone, A. W., Williams, O. A., Tassieri, M, Dobson, P and Moran, D. A. J.

Investigation into the Minimum Feature Size for ICP etched Micro and Nano-Scale Polycrystalline Diamond Mechanical Resonators

Poster, De Beers Diamond Conference, University of Warwick, 11-14th July 2016

List of Abbreviations

PCD	Polycrystalline Diamond
BDD	Boron-Doped Polycrystalline Diamond
MEMS	Micro-electromechanical Systems
IC	Integrated Circuit
POC	Point of Care
SEM	Scanning Electron Microscope
DOF	Degree of Freedom
MSD	Mean Squared Displacement
NMSD	Normalised Mean Squared Displacement
PAF	Position Autocorrelation Function
NPAF	Normalised Position Autocorrelation Function
PSD	Power Spectral Density
SNR	Signal-to-Noise Ratio
SAW	Surface Acoustic Wave
FCC	Face Centred Cubic
HPHT	High Pressure High Temperature
CVD	Chemical Vapour Deposition
MPCVD	Microwave Plasma Chemical Vapour Deposition
HFCVD	Hot Filament Chemical Vapour Deposition
GF	Gauge Factor
AFM	Atomic Force Microscopy
FEA	Finite Element Analysis
UV	Ultra Violet
EBL	Electron Beam Lithography
TLM	Transmission Line Measurement
RIE	Reactive Ion Etching
ICP	Inductively Coupled Plasma
RF	Radio Frequency

LDV	Laser Doppler Vibrometer
CMP	Chemical-Mechanical Polishing
DANL	Displayed Average Noise Level

Contents

	Pages
1. <u>Introduction</u>	<u>1-7</u>
2. <u>Cantilever Beam Theory & Diamond Material Properties</u>	<u>8-41</u>
2.1. Statics	
2.2. Vibration & Dynamics	
2.3. Dampening	
2.4. Vibration Analysis	
2.5. Diamond as a prospective material for MEMS	
2.6. Diamond Material Comparison Table	
2.7. Chapter Summary	
3. <u>Literature Review</u>	<u>42-56</u>
3.1. Cantilever Hydrodynamics	
3.2. Cantilever Micro-Rheology	
3.3. Diamond MEMS	
3.4. Thesis Aims	
4. <u>Fabrication Methods</u>	<u>57-73</u>
4.1. Lithography	
4.2. Thin Film Deposition & Lift Off	
4.3. Etching Processes	
4.3.1. Diamond Plasma Etching	
4.3.2. Silicon Plasma Etching	
4.3.3. Silicon Wet Etching	
4.4. Wire Bonding	
4.5. Chapter Summary	

5. <u>Characterisation Equipment & Methods</u>	74-85
5.1. Laser Doppler Vibrometry	
5.2. Surface Profiling	
5.3. Transmission Line Measurements	
5.4. Scanning Electron Microscopy	
5.5. Chapter Summary	
6. <u>Fabrication Results</u>	86-112
6.1. Intrinsic PCD Micro-cantilever	
6.2. Piezoresistive Micro-Cantilevers from Boron Doped PCD - Material Characterisation	
6.3. Boron-doped PCD Cantilever Fabrication	
6.4. Chapter Summary	
7. <u>Device Characterisation Results I</u>	113-146
7.1. Cantilever Thermal Response	
7.2. Cantilever Thermal Response in Water	
7.3. Reducing Cantilever Stiffness	
7.4. Device Summary	
7.5. Data Analysis Verification	
7.6. Chapter Summary	
8. <u>Characterisation Results II</u>	147-158
8.1. Characterising Piezoresistive Cantilevers	
8.2. Nature of Piezoresistivity in Cantilevers	
8.3. Contact Deformation in Undercut Area	
8.4. Chapter Summary	
9. <u>Conclusions & Future Work</u>	159-162

Appendix A. MATLAB Code for Data Analysis

Chapter 1: Introduction

Microelectromechanical systems (MEMS) were first introduced commercially in the 1980s as a way of interacting with the world on the microscopic level [1.1]. MEMS devices consist of a free moving mechanical structure interacting with external forces through means of actuation or static deflection, and integrated electronic detection. MEMS devices have been successfully incorporated into many areas of science and technology, including but not limited to: RF filters and optical switching used in telecommunications, accelerometers used in consumer electronics such as mobile telephones and electronic game controllers, accelerometers as airbag actuators in the automotive industry, micro-scale energy harvesting, bio-medical technologies such as lab on chip, bio-mass detection and molecular sorting [1.2][1.3][1.4]. MEMS is an area of engineering that is being researched, developed and applied continuously. MEMS devices have the advantage of being low cost, low power, ultra-sensitive, and have the ability to interact with the world on a sub-microscopic level. There exists no single standard MEMS fabrication procedure or high-level functional design tools and design methodology is steered by fabrication limitations and process constraints, with many techniques derived from the extensively-researched integrated circuit (IC) fabrication field.

Advancements in MEMS technology has allowed for device deployment in areas of biotechnology [1.5]. MEMS offer the functionality of larger sophisticated biological sensing and detection methods in a smaller package that is low power, has higher sensitivity and greater resolution whilst using minimal material resources. These advantages make MEMS devices ideal candidates for point of care (POC) diagnostics applications. POC devices have the advantage of being time efficient: samples need not be transported to testing areas and results are returned immediately to the operator for diagnosis. The devices can be used *in situ*: this is ideal for applications in areas where there is no access to advanced medical infrastructure, or in situations where a sample may degrade over time if transported to a laboratory [1.6].

An area of biotechnological research that could be advantaged by the incorporation of MEMS is the field of micro-rheology [1.7]. Rheology is the study of the flow of matter, and micro rheology focuses on the properties of soft matter at microscopic scale lengths. In traditional bulk rheology, rotating parallel plates apply a stress or strain on soft matter placed between them and the resulting feedback on the rotating motor is measured. The data captured of the movement of the motor can be mathematically related to the fluid properties of the matter. This method is limited to only bulk material samples ranging upwards of tens of millilitres, and is a time consuming process, sometimes taking days to complete a single measurement [1.8]. The more recently developed area of micro-rheology involves observing the migration of micron-sized tracer particles, commonly silica beads, through a soft matter sample, typically on the microliter scale.

There are two main branches of the micro-rheology discipline - passive and active. Passive methods use the inherent thermal energy present in the soft matter to drive the motion of optically or magnetically trapped tracer particles, and the particle trajectory is captured by high speed video tracking. In active systems, the tracer particle's trajectory is caused by an external force applied by the optical or magnetic trap. Micro-rheology improves on bulk rheology by allowing for small, microliter sample sizes, less time consuming measurements and the ability to measure microscopic scale length phenomena [1.9]. MEMS devices have been investigated as an alternative to these micro-rheology methods. Free end cantilever devices have been used to characterise fluid properties, however these devices are limited to data at only the frequency at which the measurement is

taken. Results are inconsistent with other established micro-rheology methods, often showing orders of magnitude in variation between the reported results and known values [1.5][1.10]-[1.12].

MEMS have also been applied as biological sensors using several different methods. The frequency shift method requires monitoring the resulting shift in resonant frequency of a vibrating cantilever due to mass loading by a foreign body. The higher the resonant frequency, the greater the mass resolution that can be achieved. Sub-femtogram resolution has been realised by this method [1.5]. Another common method of biological detection is by cantilever static deflection. This involves the observation of displacement as the cantilever becomes increasingly stressed during mass loading of the cantilever's surface [1.13].

The most common materials used for MEMS devices are silicon based. This can be attributed to the extent of established fabrication methods for this material and relative low cost [1.14]. However, increasingly demanding applications require a material that is more robust and can operate at higher frequencies [1.15]. Owing to its unique mechanical properties and its bio-inertness, polycrystalline diamond (PCD) is an attractive alternative candidate material for use in MEMS devices. Despite being significantly cheaper than single crystal diamond to produce, PCD retains the inherent mechanical properties such as high acoustic velocity, chemical and biological inertness and thermal stability [1.15]. These attributes have been exploited in devices such as ultra-sensitive mass detectors, surface acoustic wave devices and bio-sensors [1.16]-[1.18]. One of the advancements in PCD production is the ability to dope the material during growth with foreign atoms to tune the conductivity. Doping of diamond with boron makes the material conductive dependant on the doping concentration. Boron-doped diamond also exhibits piezoresistive behaviour which makes it a suitable candidate for sensor development e.g. the resistivity of a PCD film will vary depending upon strain. The gauge factor of boron doped PCD (BPCD) (the change in resistance versus strain applied) is similar to that of piezoresistive silicon and is more thermally stable [1.19], [1.20].

	Silicon	Silicon Carbide	Natural Diamond	Polycrystalline Diamond
Young's Modulus (GPa)	131	440	1220	1050
Thermal Conductivity (W/cm.K)	1.5	5	22	20

Table 1.1 Textbook values for Young's modulus and thermal conductivity in common MEMS materials and natural diamond. High young's modulus coupled with relative low mass density gives diamond a high acoustic velocity. High thermal conductivity reduces intrinsic energy loss in vibrating structures [1.21], [1.22].

A primary aim of this work was to demonstrate the potential for micro-rheology principles and data analysis techniques to be applied to a nano-scale PCD MEMS device. The design, fabrication and thermally driven motion of free-end cantilever beam structures submerged in soft matter was investigated and is reported on. The use of such a MEMS device would negate the need for powerful optical traps that can potentially heat the sample locally, and also have the potential for higher frequency operation. The methods investigated here show the potential to extract data across a large frequency range from a single measurement with greater accuracy than other cantilever type devices.

Static deflection forms the basis of operation for devices further investigated in this thesis, specifically the design, fabrication and characterisation of a BDD cantilever type MEMS POC device for biological organism detection. Cantilever deflection sensitivity in BDD devices and geometrical considerations are explored.

The main focus of this thesis is the development of PCD and BDD MEMS devices for both POC micro-rheology and micro-organism detection applications. **Chapter 2** will provide an in-depth discussion on the theoretical background of the material and the physics underpinning device operation. In **Chapter 3** a review of relevant literature is provided to inform the reader of the current state-of-the art. **Chapter 4** details the fabrication processes investigated and developed in order to

manufacture diamond MEMS devices. **Chapter 5** explains the tools and methods used to characterise the diamond material and devices. **Chapter 6** presents fabrication results and process development achieved by the author, including dry and wet etching methods, metallisation, free standing device release and some material characterisation. **Chapter 7** and **Chapter 8** present characterisation results for the devices detailed in **Chapter 6**, including the characterisation of thermal fluctuations in air and water of PCD microcantilevers, and the piezoresistive effect in BDD micro-cantilevers. **Chapter 9** concludes this thesis with some discussion regarding the results and suggestions of future work.

References

- [1.1] J. W. Judy, "Microelectromechanical systems (MEMS): fabrication , design and Applications," *Smart Materials and Structures*, vol. 10, pp. 1115-1134, 2001.
- [1.2] H. Jin, J. Zhou, X. He, W. Wang, H. Guo, S. Dong, D. Wang, Y. Xu, J. Geng, J. K. Luo, and W. I. Milne, "Flexible surface acoustic wave resonators built on disposable plastic film for electronics and lab-on-a-chip applications." *Scientific Report*, vol. 3, no. 2, p. 2140, 2013.
- [1.3] D. Arecco, "Analysis and preliminary characterization of a MEMS cantilever-type chemical sensor," *Worcester Plytechnic*, Thesis, December, 2003.
- [1.4] O. Sidek, M. Miskam, H. Khaleed, and M. Alias, "Optimal Design of Capacitive Micro Cantilever Beam Accelerometer," *Modern Applied Science*, vol. 3, no. 9, pp. 16-28, 2009.
- [1.5] V. Agache, G. Blanco-Gomez, M. Cochet, and P. Caillat, "Suspended nanochannel in MEMS plate resonator for mass sensing in liquid," *IEEE International Conference on MEMS*, pp. 157-160, 2011.
- [1.6] S. L. Karsten, M. C. Tarhan, L. C. Kudo, and D. Collard, "Talanta Point-of-care (POC) devices by means of advanced MEMS," *Talanta*, vol. 145, pp. 55-59, 2015.

- [1.7] E. Lemaire, B. Caillard, M. Youssry, and I. Dufour, "High frequency viscoelastic measurements of fluids based on microcantilever sensing : New modeling and experimental issues," *Sensors and Actuators A: Physical*, Vol 201, pp. 230-240, 2014.
- [1.8] G. Foffano, J. S. Lintuvuori, A. N. Morozov, K. Stratford, M. E. Cates, and D. Marenduzzo, "Bulk rheology and microrheology of active fluids," *European Physics Journal E*, 35:98, 2012.
- [1.9] M. Tassieri, F. Del Giudice, E. J. Robertson, N. Jain, B. Fries, R. Wilson, A. Glidle, F. Greco, P. A. Netti, P. L. Maffettone, T. Bicanic, and J. M. Cooper, "Microrheology with Optical Tweezers : solutions 'at a glance'" *Scientific Reports*, vol5, pp. 1-6.
- [1.10] A. Arneodo, L. Streppa, P. Argoul, F. Argoul, A. Arneodo, L. Streppa, P. Argoul, F. A. Passive, A. Arneodo, L. Streppa, P. Argoul, and F. Argoul, "Passive microrheology of soft materials with atomic force microscopy" *Applied Physics Letters*, Vol 108 pp. 0-4, 2016.
- [1.11] M. Youssry, E. Lemaire, B. Caillard, A. Colin, and I. Dufour, "On-chip characterization of the viscoelasticity of complex fluids using microcantilevers," *Measurement Science and Technology*, vol. 23, no. 12, p. 125306, 2012.
- [1.12] C. Riesch, E. K. Reichel, F. Keplinger, and B. Jakoby, "Characterizing Vibrating Cantilevers for Liquid Viscosity and Density Sensing," *Journal of Sensors*, vol. 2008, pp. 11-13, 2008.
- [1.13] L. G. Carrascosa, M. Moreno, M. Álvarez, and L. M. Lechuga, "Nanomechanical biosensors: A new sensing tool," *Trends in Analytic Chemistry*, vol. 25, no. 3, pp. 196-206, 2006.
- [1.14] N. Technologies, S. Editor, and J. Ramsden, "Handbook of Silicon Based MEMS Materials and Technologies." *Elsevier*, 2010.
- [1.15] O. Auciello and C. Gudeman, "Are diamonds a MEMS best friend?" *IEEE Microwave Magazine*, vol. 8, no. 6, pp. 61-75, 2007.
- [1.16] T. Bautze, S. Mandal, O. A. Williams, P. Rodière, T. Meunier, and C. Bäuerle, "Superconducting nano-mechanical diamond resonators," *Carbon*, vol. 72, pp. 100-105, 2014.

- [1.17] J. Song, J. Sung, and H. Chang, "SAW Filter with AlN on Diamond" *Diamond and Related Materials*, pp. 1-13, 2008.
- [1.18] V. Mortet, O. a. Williams, and K. Haenen, "Diamond: A material for acoustic devices," *Applied Material Science*, vol. 205, no. 5, pp. 1009-1020, 2008.
- [1.19] J. Zhang, J. W. Zimmer, R. T. Howe, and R. Maboudian, "Characterization of boron-doped micro- and nanocrystalline diamond films deposited by wafer-scale hot filament chemical vapor deposition for MEMS applications," *Diamond and Related Materials*, vol. 17, pp. 23-28, 2008.
- [1.20] N. L. Privorotskaya, H. Zeng, S. Member, J. A. Carlisle, R. Bashir, and W. P. King, "Piezoresistive Microcantilevers From Ultrananocrystalline Diamond," *Journal of MEMS*, vol. 19, no. 5, pp. 1234-1242, 2010.
- [1.21] E. V Ivakin, A. V Sukhodolov, V. G. Ralchenko, A. V Vlasov, and A. V Khomich, "Measurement of thermal conductivity of polycrystalline CVD diamond by laser-induced transient grating technique," *Quantum Electronics*, Vol 32:4, 2002.
- [1.22] C. J. H. Wort and R. S. Balmer, "Diamond as an electronic material," *Mater. Today*, vol. 11, no. 1, pp. 22-28, 2008.

Chapter 2: Cantilever Beam Theory & Diamond Material Properties

MEMS devices consist of a moving mechanical structure and integrated electronic readout. There are two modes of operation for a MEMS device: static mode and dynamic mode. In static mode, the displacement of the mechanical part of the device driven by some unknown external force is electronically monitored. The resulting displacement can be related to the magnitude of the force exerted on the device. In dynamic mode, the mechanical part of the device is excited in a vibrational manner and the vibrations monitored. Changes in the frequency and magnitude of the vibrations contain information about the nature of the device's environment. The following chapter contains background information on the nature of static and dynamic motion of cantilever beam-based MEMS, including the physics pertaining to cantilever deflection and numerical analyses used to evaluate environmental information from the devices. Synthetic diamond, in its intrinsic and doped forms, is also interrogated as a material for MEMS devices.

2.1 Statics

The cantilever bridge, in classic form, is a rigid structure, typically a beam or pole, anchored at one end.

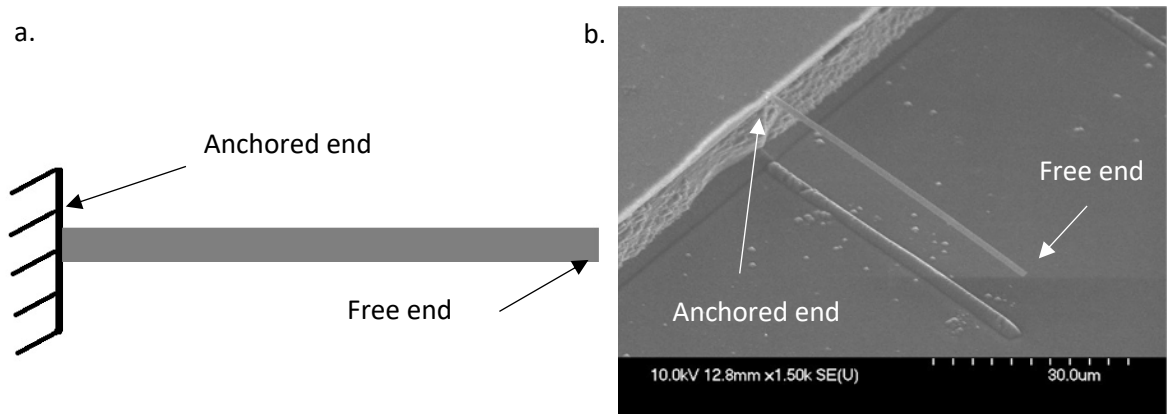


Figure 2.1.1 Cantilever Beam schematic (a) and scanning electron microscope (SEM) image of polycrystalline diamond micro cantilever (b) showing anchored and free ends.

By applying a force, or load, the cantilever structure starts to deform. If the cantilever construction is homogenous, it will experience equal amounts of tensile and compressive stress as shown in **Figure 2.1.2**. The nature of the deformation depends on the physical dimensions of the cantilever, the mechanical properties of the material that the cantilever is made from, and the area on the cantilever where the load is applied. In the simplest case, we can observe a point load placed at the free end of the cantilever:

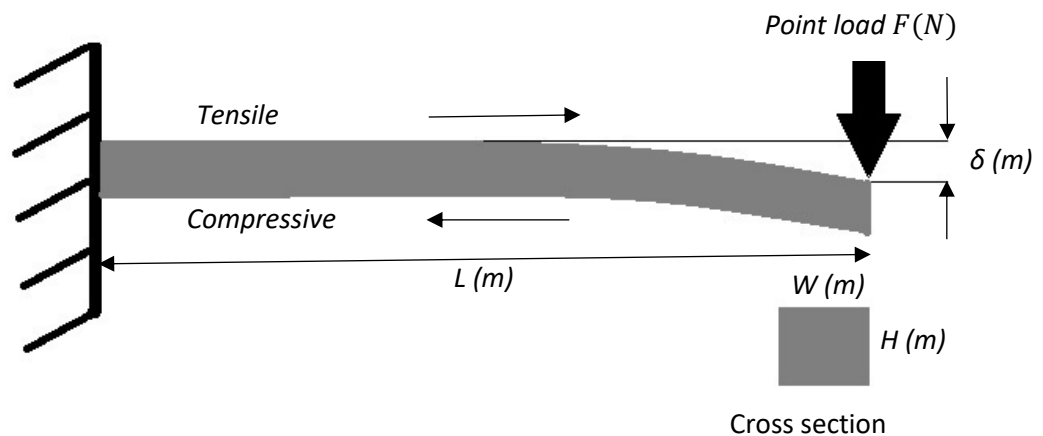


Figure 2.1.2 Cantilever Beam under Point Load

Figure 2.1.2 shows a simple cantilever beam with dimensions length L , width W , and height H , being deflected by a point load. Typically, for a MEMS device, these dimensions would be somewhere in the order of tens of micrometres. The relationship between these dimensions and deflection δ in meters is [2.1]:

$$\delta = \frac{F}{k} = \frac{FL^3}{3EI} \quad (2.1.1)$$

Where F is the force applied to the end of the cantilever, I is the area moment of inertia, and E is the modulus of elasticity. k is defined as the stiffness constant of the cantilever beam. The area moment of inertia for a rectangular cross section is expressed as [2.2]:

$$I = \frac{WH^3}{12} \quad (2.1.2)$$

The modulus of elasticity is the material's the Young's modulus and concerns the material's tendency to deform when acted upon by an exterior force. It is defined as the ratio of tensile stress to tensile strain. The higher the Young's modulus the less the structure will deflect for a given load. To find the deflection at any point, x , along the length of the cantilever under a point load we can modify **Equation 2.1.1** to [2.1]:

$$\delta = \frac{Fx^2}{6EI} (3L-x) \quad (2.1.3)$$

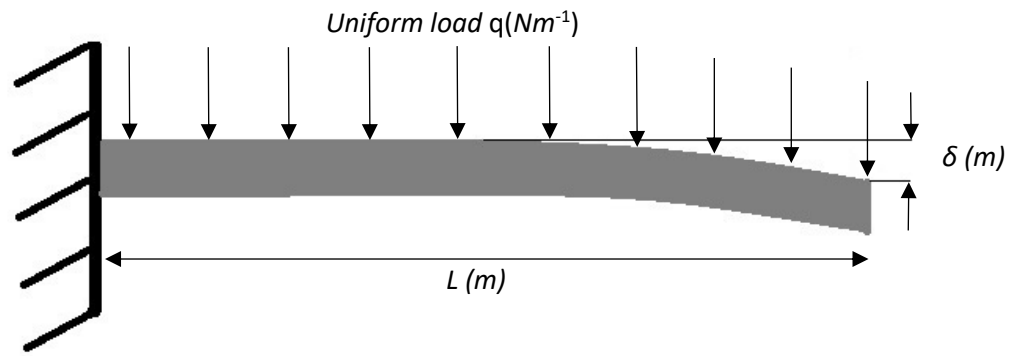


Figure 2.1.3 Cantilever Beam under Uniform Load

In the case of a uniformly distributed load, q , as in **Figure 2.1.3**, the equation governing the deflection δ at the free end is:

$$\delta = \frac{qL^4}{8EI} \quad (2.1.4)$$

And the deflection at any point, x , along the uniformly loaded cantilever is described by:

$$\delta = \frac{qx^2}{24EI} (6L^2 - 4Lx - x^2) \quad (2.1.5)$$

Load distribution is not limited to uniform and point. In the case of MEMS devices, loads can be distributed in a multitude of other forms including triangular, trapezoidal, parabolic, or most likely a combination of all these instances. However, distributed loads can be represented by a resultant point load somewhere along the length of the cantilever. The exact distribution of loading on a MEMS device can be difficult to determine, but from a detected displacement it is possible to evaluate the total load on a device and force exerted. These methods are particularly relevant to device calibration and characterisation.

2.2 Vibration and Dynamics

Many MEMS devices are concerned with the oscillatory behavior of their mechanical parts. We now turn to look at the cantilever beam in the context of a vibratory system: oscillatory motion and the forces associated.

There are two classes of vibration to be considered: free and forced. Free vibration occurs due to the inherent forces present in a system owing to mechanical and geometrical properties, in absence of any external subtractive forces. Free vibration systems will oscillate at one or more of the natural (or resonant) frequencies of the system, which is again determined by certain inherent mechanical and geometrical factors.

Forced vibrations are due to some external force acting upon the system. If the force is periodic then the forced vibrations will occur at the frequency of the applied force. If the applied force happens to correspond with the natural frequency of the system, the phenomenon known as resonance occurs. The excitation of the system increases exponentially at resonance and massive relative magnitude oscillations occur. Later in this chapter we will also be discussing oscillations that do not occur at the natural frequency of the system, known as harmonics.

For some of the devices reported in this body of work (see **Chapter 6**), we will be discussing the vibration of their mechanical parts owing to thermal fluctuations. These vibrations are classed as forced, the force coming from colliding particles surrounding the device owing to the inherent thermal energy present in the particles.

We can consider classical mass spring damper system with one degree of freedom (DOF) as a model from which to approach the free vibrations of a harmonic system:

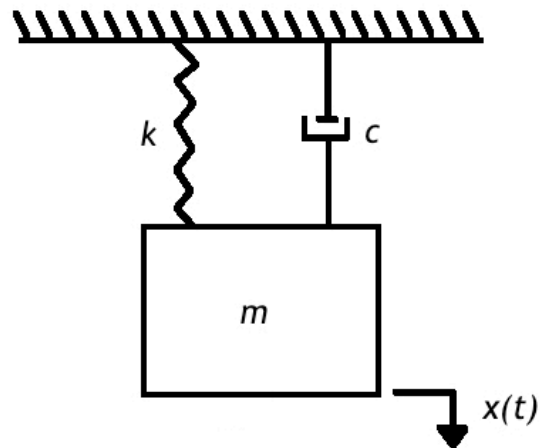


Figure 2.2.1. Mass Spring Damper System

With m being the mass of the system, k the spring stiffness constant, c the dampening of the system, assumed in the free vibration scenario to be 0 (undamped), and $x(t)$ the displacement of mass, m at time, t . The zero of the x coordinate system is located where the spring is at equilibrium. If the mass is moved from the equilibrium position and released, the mass will begin to oscillate around the equilibrium point at the natural frequency of the system. If we take the system at an arbitrary position x and apply Newton's second law, we obtain [2.3]:

$$\sum F = ma = -kx \quad (2.2.1)$$

The force acting on the mass is the spring constant force trying to regain equilibrium. **Equation 2.2.1** can be expressed as:

$$-\frac{kx}{m} = \frac{d^2x}{dt^2} \quad (2.2.2)$$

And defining constant

$$\omega^2 = \frac{k}{m} \quad (2.2.3)$$

Equation 2.2.2 can be written as

$$\frac{d^2x}{dt^2} + \omega^2x = 0 \quad (2.2.4)$$

This is a homogenous second-order linear differential equation with the general solution [2.3]:

$$x(t) = A \cos(\omega t + \theta) \quad (2.2.5)$$

Where A is the amplitude of the oscillation, ω the angular frequency and θ the phase angle. With no damping coefficient present in the free vibration system, the oscillations will continue until acted upon by an external force.

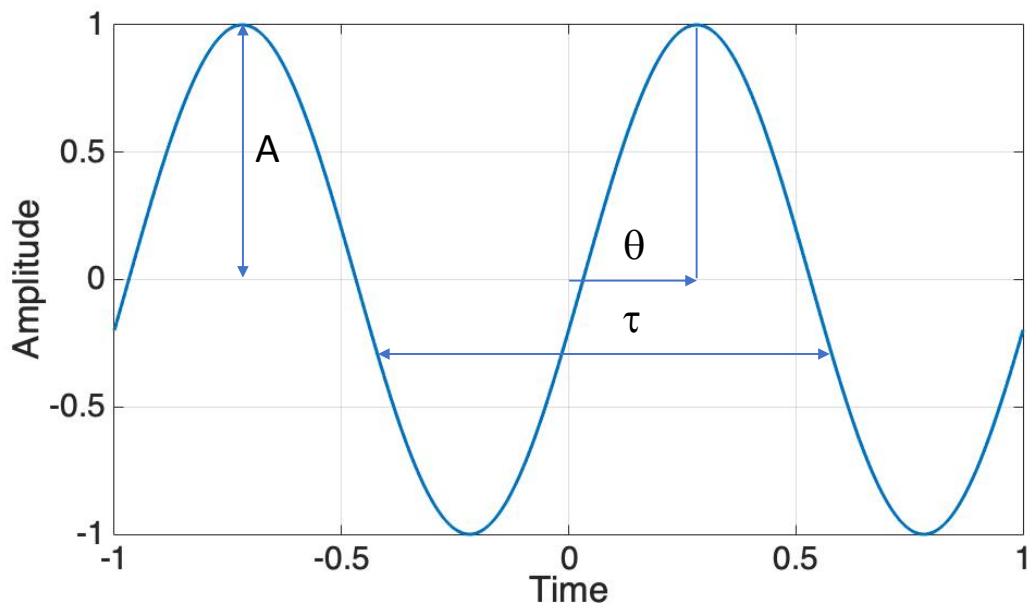


Figure 2.2.2. Graphical Representation of $x(t) = A \sin(\omega t + \theta)$. A represents the amplitude of the oscillations (normalised to 1 here), θ represents a phase shift, and τ is the period of oscillations.

The period of the oscillations for **Equation 2.2.5** is:

$$\tau = \frac{2\pi}{\omega} \quad (2.2.6)$$

And once again substituting **Equation 2.2.3** we find an expression for the period:

$$\tau = 2\pi \sqrt{\frac{m}{k}} \quad (2.2.7)$$

Given that frequency is 1/period we can write the natural frequency of the oscillations as such [2.3]:

$$f = \frac{1}{2\pi} \sqrt{\frac{k}{m}} \quad (2.2.8)$$

In the case of the free vibrations of a cantilever beam, the mathematical model is more complex as we must consider the higher modes of vibration. Higher modes of vibration are vibrations that take place at a higher frequency than the fundamental frequency. The free vibrations of the cantilever beam can be explained by the Euler-Bernouli beam theory, a simplification of the linear theory of elasticity presented in the late 18th century [2.5].

We can start the analysis from the equation of motion for a cantilever beam as described by Meirovitch [2.4]:

$$\frac{d^2}{dx^2} \left\{ EI(x) \frac{d^2 Y(x)}{dx^2} \right\} = \omega^2 m(x) Y(x) + q(x) \quad (2.2.9)$$

Where E is the modulus of elasticity of the beam, I the second moment of inertia of the beam cross section, $Y(x)$ is the displacement of the beam in the Y direction at distance x from the fixed end, ω is the circular natural frequency, $q(x)$ is a transverse load on the beam and m is the mass of the cantilever per unit length where:

$$m = \rho A \quad (2.2.10)$$

ρ is the density of the material and A , the area. We can make two assumptions that simplify Equation 2.2.9: in a homogenous beam EI is independent of x , and in the case of free vibration the transverse load q is 0. If we introduce the constant β defined as:

$$\beta = \left(\frac{\omega^2 m}{EI} \right)^{\frac{1}{4}} \quad (2.2.11)$$

Then we can write the equation for the free vibrations of a uniform cantilever beam as:

$$\frac{d^4 Y(x)}{dx^4} - \beta^4 Y(x) = 0 \quad (2.2.12)$$

Given the following boundary condition for a fixed end cantilever beam [2.5]:

$$\begin{aligned} &\text{at the fixed end of the beam; } x = 0, Y(x) = 0, \frac{dY(x)}{dx} = 0 \\ &\text{at the free end of the beam; } x = L, \frac{d^2 Y(x)}{dx^2} = 0, \frac{d^3 Y(x)}{dx^3} = 0 \end{aligned} \quad (2.2.13)$$

The general solution for **Equation 2.2.8** becomes:

$$Y(x) = A_1 \cosh(\beta_n x) + A_2 \sinh(\beta_n x) + A_3 \cos(\beta_n x) + A_4 \sin(\beta_n x) \quad (2.2.14)$$

Where

$$\beta_n = \left(\frac{\omega_n^2 m}{EI} \right)^{\frac{1}{4}} \quad (2.2.15)$$

A_1, A_2, A_3, A_4 are constants and ω_n are the natural frequencies of the beam. The solutions are only non-trivial when:

$$1 + \cosh(\beta_n L) \cos(\beta_n L) = 0 \quad (2.2.16)$$

The first three non-trivial solutions, or Eigenvalues are:

$$\beta_1 L = 1.88, \beta_2 L = 4.69, \beta_3 L = 7.85 \quad (2.2.17)$$

And the corresponding natural frequencies can be written as:

$$\omega_1 = \beta_1^2 \sqrt{\frac{EI}{mL^4}}, \omega_2 = \beta_2^2 \sqrt{\frac{EI}{mL^4}}, \omega_3 = \beta_3^2 \sqrt{\frac{EI}{mL^4}} \quad (2.2.18)$$

The shape of the displacement of the beam at each natural frequency is called the mode shape, and can be shown by the formula [2.6]:

$$Y(x) = A_n \{ (\sin(\beta_n L) - \sinh(\beta_n L)) (\sin(\beta_n x) - \sinh(\beta_n x)) + (\cos(\beta_n L) - \cosh(\beta_n L)) (\cos(\beta_n x) - \cosh(\beta_n x)) \} \quad (2.2.19)$$

The first three natural frequency mode shapes of a cantilever beam with arbitrary dimensions and mechanical properties are displayed in **Figure 2.2.3** below. Theoretically, in a continuous system, there will be an infinite number of natural frequencies and associated eigenvalues. In real terms, a cantilever's modes of vibration will be limited by energy losses internally from friction and also external loading by environmental factors.

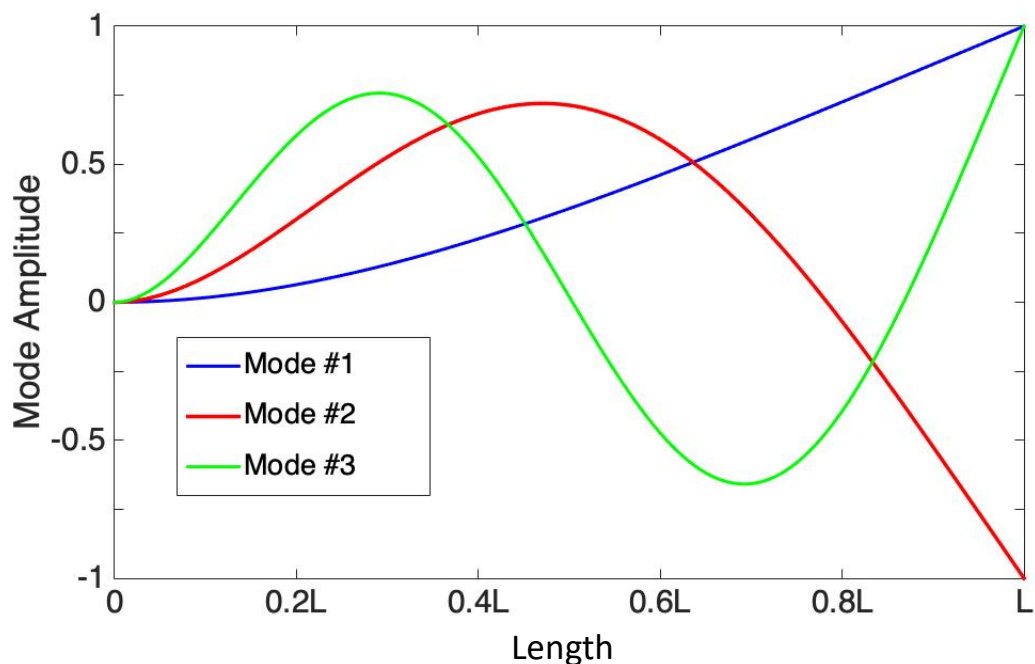


Figure 2.2.3. MATLAB generated plot of cantilever mode shapes for the first three modes for a cantilever beam of arbitrary dimensions. 1st mode (blue), 2nd mode (red) and 3rd mode (green).

2.3 Dampening

So far, we have investigated the cantilever beam in terms of static deflection and free vibratory conditions. These models are useful as a starting point in predicting the behavior of devices. However, MEMS applications are typically concerned with characterizing the external forces acting upon the device. In this section we will be describing the theoretical model of a suspended structure with a single degree of freedom with external dampening forces and how we can extract the dampening contributions to the system. Strictly speaking, we will be looking at damped motion in the context of a device submerged in viscous solutions and also solutions having viscous and elastic components (viscoelastic).

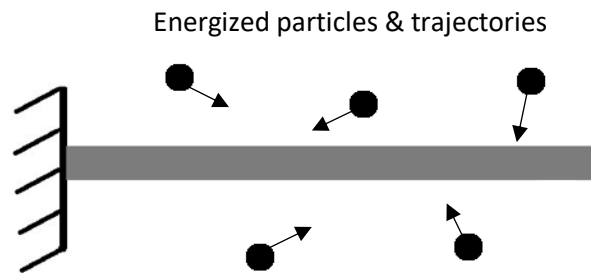


Figure 2.3.1 Schematic of cantilever submerged in a thermal bath showing energised particles with random trajectories.

Consider the condition of a cantilever submerged in a thermal bath as shown in **Figure 2.3.1**. The particles surrounding the cantilever are driven to random fluctuations owing to the thermal energy present in the system. The randomly fluctuating particles bombard the cantilever beam exerting a stochastic force on the structure causing it to also fluctuate. The maximum amplitude of the beam fluctuations is governed by the stiffness of the cantilever beam k . The stiffness, the thermal energy and the cantilever's fluctuations are related by the Equipartition theorem [2.7]:

$$\frac{1}{2}k_bT = \frac{1}{2}k\langle x^2 \rangle$$

(2.3.1)

where k_b is Boltzmann's constant, T is the absolute temperature, k the cantilever stiffness and $\langle x^2 \rangle$ the variance of the cantilever tip. By appealing to this principle, we can determine k without the need of any prior knowledge of the system's geometries, once the variance is measured.

In the case of the submerged MEMS cantilever, energy is dissipated by liquid motion induced by the cantilever oscillations. Consequently, contributions of higher modes of vibration are negligible and we can assume the presence of only the fundamental mode. If the deflections of the cantilever tip are small with respect to the cantilever dimensions, with minimal fluid interaction, it has been shown that the cantilever's dynamic behavior can be approximated by the simple harmonic oscillator model [2.8].

The motion of a thermally driven damped cantilever beam with mass, m stiffness, k stochastic thermal forces, ξ_T and constant viscous drag coefficient, γ can then be described by the following Langevin equation [2.3]:

$$m\ddot{X} + \gamma\dot{X} + kX = \xi_T \quad (2.3.2)$$

where X is the deflection measured at the tip of the cantilever beam. In the case of a highly damped MEMS cantilever, the inertia force is negligible when compared to the dampening force [2.9]. X will be a random variable dependent on ξ_T and the friction coefficient γ is related to both the cantilevers physical dimensions and the viscosity of the surrounding fluid via the Stokes drag law, where η is the Newtonian (constant) viscosity:

$$\gamma = \beta\eta \quad (2.3.3)$$

The drag force coefficient parameter β can be calibrated from measurements taken for a fluid of known viscosity for specific device dimensions. In the case of a trapped sphere in a viscous solution the drag force coefficient is [2.9]:

$$\gamma = 6\pi r\eta \quad (2.3.4)$$

Extensive prior research has been published by various authors on the determination of the drag force coefficient for a submerged cantilever with varying degrees of accuracy, and factors such as frequency, the viscosity of the fluid to be characterised, and interaction between the surfaces of the device and the fluid's molecular structure under vibratory conditions play a large part in the various definitions. A more thorough interrogation of these methods will be discussed in the forthcoming **Literature Review** chapter.

This method for determining viscosity hold true for Newtonian fluids, however no fluid is exclusively Newtonian in nature, so further steps must be considered when determining the properties of non-Newtonian or complex fluids.

When deformed, a purely Newtonian fluid will not return to its original state, as it is purely viscous. In contrast, non-Newtonian material has both a viscous and elastic component. There exists a restoring force due the inherent elasticity. Therefore, we must define a mathematical model that includes this restoring force. Tassieri *et al* approach this problem by providing a solution to a generalized Langevin equation describing the trajectory of a trapped particle suspended into a non-Newtonian fluid in terms of either its mean squared displacement (MSD) or its position autocorrelation function (PAF) [2.9]. In their case, the generalized Langevin equation has the following form:

$$m\vec{a}(t) = \vec{f}_r(t) - \int_0^t \xi(t-\tau)\vec{v}(\tau)d\tau - k\vec{r}(t) \quad (2.3.5)$$

Where m is the mass of the particle, $\vec{a}(t)$ is its acceleration, $\vec{v}(\tau)$ its velocity, k the stiffness of the trap and $\vec{f}_r(t)$ is the term representing the stochastic thermal forces driving the motion of the particle. The integral term is the viscous force

acting on the particles and contains ξ that is a generalized time dependent memory function, which accounts for the viscoelastic nature of the complex fluid. Given that both the submerged cantilever and trapped sphere system share the dynamics of a simple harmonic oscillator, it should be possible to apply the above solution to the cantilever system [2.10][2.11]. Therefore, in **Equation 2.3.5**, the velocity term becomes the velocity of the cantilever tip and the trap stiffness term becomes the stiffness of the cantilever beam. The solution presented by Tassieri et al relates the materials complex shear modulus $G^*(\omega)$ to the Fourier transformed normalized MSD ($\Pi(\tau)$) and/or normalized PAF ($A(\tau)$) [2.12]:

$$G^*(\omega) \frac{\beta}{k} = \left(\frac{1}{i\omega\hat{\Pi}(\omega)} - 1 \right) = \left(\frac{1}{i\omega\hat{A}(\omega)} - 1 \right)^{-1} = \frac{\hat{A}(\omega)}{\hat{\Pi}(\omega)} \quad (2.3.6)$$

B is the same friction coefficient from **Equation 2.3.4**. The complex modulus is a complex number made up of the terms $G'(\omega) + iG''(\omega)$ which are the storage and loss moduli respectively. They relate to the elastic energy stored in the material and the viscous dissipation of energy. The complex modulus can be defined as the ratio of the Fourier transform of the stress to the Fourier transform of the strain of the system [2.9].

$$G^*(\omega) = \frac{\hat{\sigma}(\omega)}{\hat{\epsilon}(\omega)} \quad (2.3.7)$$

For a constrained system, the normalised MSD and normalised PAF obey to the following relationship [2.12]:

$$\Pi(\tau) + A(\tau) = 1 \quad (2.3.8)$$

It is important to note at this point that the autocorrelation function of the thermal fluctuations of a trapped particle has the form:

$$A(\tau) = e^{-\lambda\tau} \tag{2.3.9}$$

Which is a single decaying exponential where $\lambda = k/B\eta$. This relates to the relaxation time of the surrounding fluid. Again, we can make the assumption that the motion of the tip of a heavily damped cantilever can be approximated as a trapped particle and therefore will also have a similar single exponential decay term dependent on the cantilever geometry and stiffness. The measurement procedure and the analysis of both the MSD and the PAF will be discussed in the forthcoming **Vibration Analysis** section of this chapter.

The stress-strain relationship in a non-Newtonian fluid can be mechanically modeled as a network of springs and dampers, with the springs exclusively representing the elastic component of the material and the dampers exclusively representing the viscous component. A common configuration is the Kelvin-Voigt and model shown in **Figure 2.3.1**, where the elastic and viscous components act in parallel on the system [2.9].

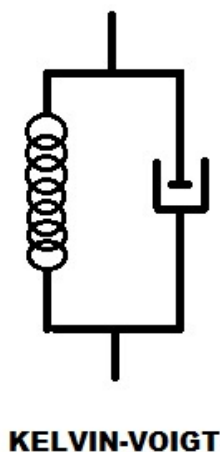


Figure 2.3.2 Kelvin-Voigt model describing the elastic and viscous components of a non-Newtonian fluid. The spring on the left represents the elastic component and the dashpot on the right represents the viscous component. The two components act in parallel with each other.

In the Kelvin-Voigt model the spring and damper experience the same deformation for an applied stress. This model can be analyzed to show the relationship between stress and strain in a system with viscous and elastic components. This is the case which Tassieri *et al* use to model a trapped particle in a viscous fluid: the stiffness of the spring represents the stiffness of the trap and the damper represents the dampening of the surrounding fluid. In the case of a MEMS cantilever, the spring stiffness represents the stiffness of the cantilever beam.

In the case of the Kelvin-Voigt model we can write two expressions to describe the total strain ε and the total stress σ [2.9].

$$\begin{aligned}\varepsilon &= \varepsilon_E = \varepsilon_v \\ \sigma &= \sigma_E + \sigma_v\end{aligned}\tag{2.3.10}$$

Where subscripts E and v donate the spring and dampening components. As the spring is purely elastic we can write its stress component as:

$$\sigma_E = G\varepsilon\tag{2.3.11}$$

Where G is the elastic constant proportional to the material's Young's Modulus. Similarly, for the dampening component which is exclusively viscous, we know that stress is directly proportional to strain rate, so we can express the viscous component as:

$$\sigma_v = \eta \frac{\partial \varepsilon}{\partial t}\tag{2.3.12}$$

Where η is the Newtonian viscosity of the viscous contribution. We can then write the total stress as:

$$\sigma(t) = G\varepsilon_E + \eta \frac{\partial \varepsilon}{\partial t} \quad (2.3.13)$$

If we then take the Fourier transform of **Equation 2.3.13** we find the expression:

$$\hat{\sigma}(\omega) = G\hat{\varepsilon}(\omega) + \eta i\omega\hat{\varepsilon}(\omega) \quad (2.3.14)$$

Rearranging we can write:

$$\frac{\hat{\sigma}(\omega)}{\hat{\varepsilon}(\omega)} = G + \eta i\omega \quad (2.3.15)$$

which is the Fourier transform of the stress divided by the Fourier transform of the strain. This is the definition of the complex modulus as written in **Equation 2.3.7**. Thus, the Kelvin-Voigt mechanical model represents a viscoelastic material that has a frequency independent elastic modulus G and a frequency dependent viscous modulus $\eta\omega$. The homogeneous solution of **Equation 2.3.13** in the time domain is:

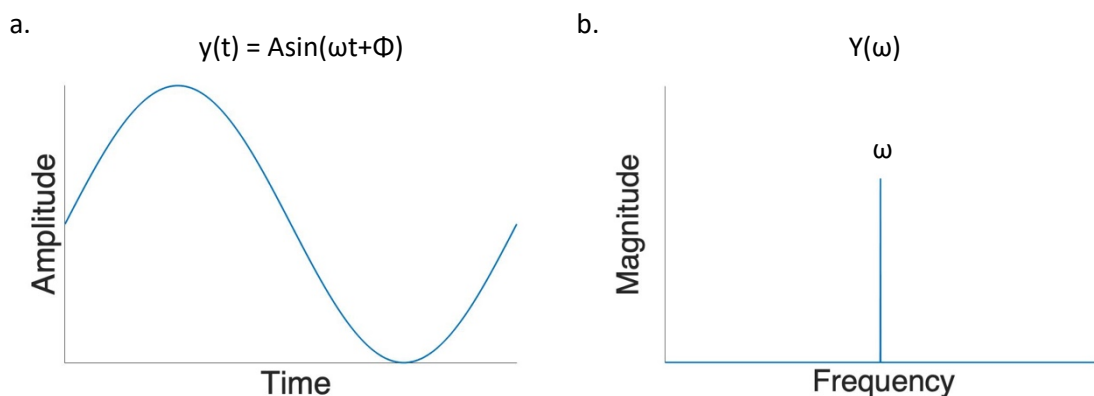
$$\varepsilon(t) = \varepsilon_0 e^{-\lambda t} \quad (2.3.16)$$

Where λ is the characteristic relaxation time of the mechanical system. This is the same as the single decaying exponential term found in **Equation 2.3.9**. This again shows that the Kelvin-Voigt model is a suitable model for the motion of a trapped particle or damped cantilever in a viscous solution.

2.4 Vibration Analysis

When characterising vibrating MEMS we must consider the displacement of the mechanical contribution of the system. From measurements of mechanical displacement, we can use a set of analytical tools to extract the behaviour of the system. The methods used to take actual displacement measurements of MEMS devices will be covered in **Chapter 5** of this thesis. For the purpose of reviewing analysis techniques, we will be looking at sinusoidal functions to approximate the motion of a harmonic mechanical system.

Consider a sinusoidal function of the form $y(t) = \sin(\omega t + \Phi)$ where $\omega = 2\pi \times$ frequency and Φ is the phase angle of the signal. If we take the Fourier transform of $y(t)$ this reveals the frequency spectrum of the signal:



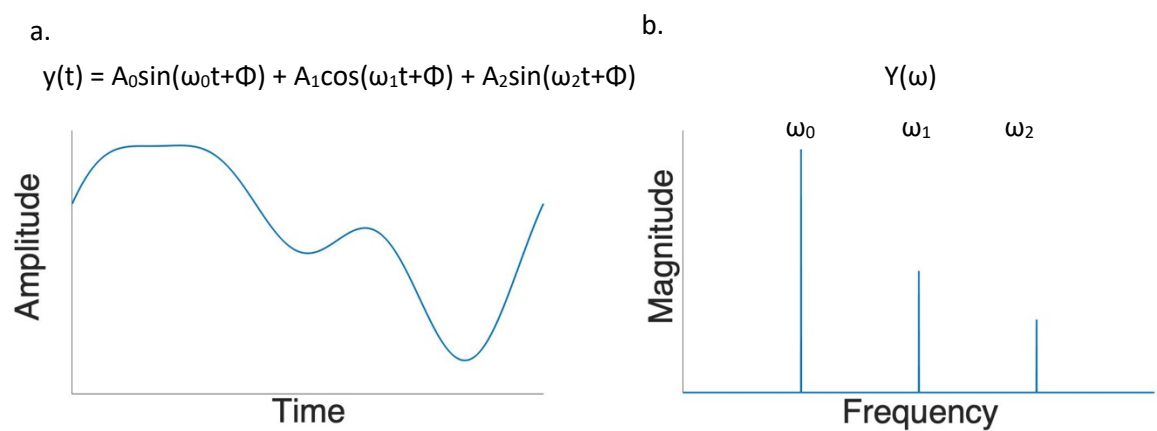
Figures 2.4.1a & b. Sinusoidal function (a), $y(t) = A\sin(\omega t + \Phi)$ and its Fourier transform $Y(\omega)$, (b).

The Fourier transform has the mathematical form:

$$Y(\omega) = \int_{-\infty}^{\infty} y(t)e^{i\omega t} dt$$

(2.4.1)

The Fourier transform of a periodic signal is complex in nature and contains the frequency magnitude of the signal and the phase angle. This reveals the fundamental frequency ω_0 of the system. In the case of harmonic mechanical systems there exists not only a fundamental frequency, but also higher modes of vibration known as harmonics. The signal is a sum of the different sine and cosine terms representing the different harmonics. The Fourier transform of a harmonic oscillator reveals the higher frequency modes. The higher frequency modes are related to the fundamental mode by integer values. The first mode ω_1 will be twice the frequency value of ω_0 , the second mode ω_2 will be twice the value of ω_0 and so on as shown in **Figure 2.4.2**.



Figures 2.4.2 a & b. Sinusoidal function (a), $y(t) = A_0\sin(\omega_0t + \Phi) + A_1\cos(\omega_1t + \Phi) + A_2\sin(\omega_2t + \Phi)$ containing multiple frequencies ω_0 , ω_1 and ω_2 , and (b), the Fourier transform of $y(t)$, $Y(\omega)$. The Fourier transform allows identification of the multiple frequency components.

In the case of a MEMS resonator we have to build up a time series of data as a set of measurements of the displacement of the device across a finite time period. These individual measurements are called samples. The sample rate of the time series is the rate at which the samples are acquired. This acquisition rate limits the range of frequencies that can be shown in the Fourier transform of the signal. The upper bounds of the frequency range in the Fourier transform is half the acquisition rate of the time series. This is known as the Nyquist frequency and exists owing to an effect known as aliasing. If the signal is not adequately sampled as in **Figure 2.4.3** then the signal could be misinterpreted as in **Figure 2.4.4**,

which introduces errors or artefacts in the frequency domain. Hence, the samples must be acquired at least at twice the frequency of interest. This is known as the Nyquist rate.

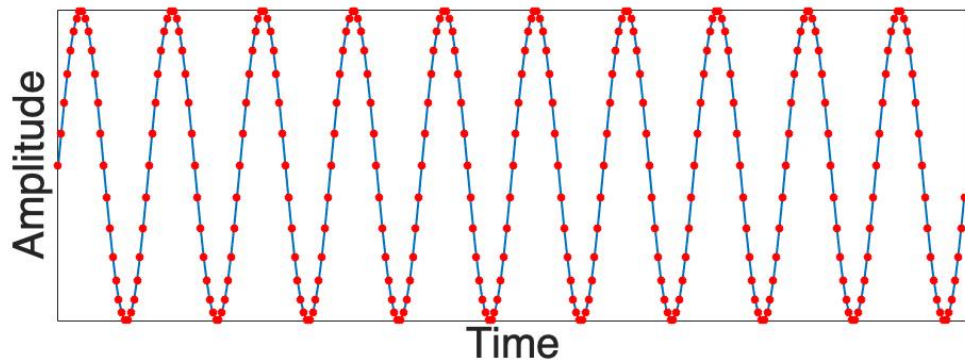


Figure 2.4.3. Signal sampled (red dots) at an adequate sample rate i.e. greater than twice the frequency of interest.

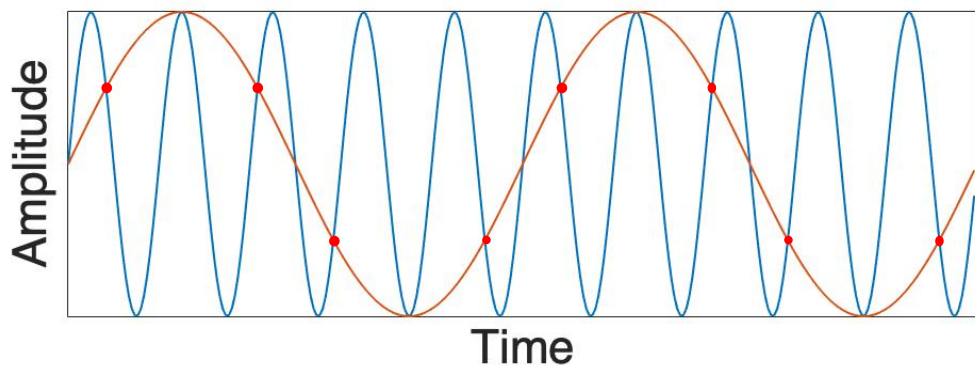


Figure 2.4.4. Signal sampled at an inadequate sample rate (red dots) i.e. less than twice the frequency of interest, and the corresponding misinterpreted signal due to aliasing errors shown in orange.

We can use the Fourier transform of a signal to estimate how the energy in the system is distributed. If we take the square of the magnitude of the frequency spectrum we lose the phase information and are left with the power spectral density (PSD). The unit of the PSD is power per frequency.

$$\text{PSD} = |Y(\omega)|^2 \tag{2.4.2}$$

The total power in the signal is given by the area under the PSD curve which, in accordance with Parseval's theorem, is equal to the variance of the time series [2.13]. By dividing by the total power or variance we can normalise the data [2.12].

We can accurately estimate the total power present in a MEMS cantilever's displacement signal by taking an average of many measurements of the power spectrum and integrating the area under the PSD curve, or we can take a sufficiently long-time measurement of the cantilever's displacement and calculate the variance by squaring the displacement and taking the average.

An important analysis technique when relating the motion of a MEMS cantilever to its surroundings is the position autocorrelation function (PAF). The PAF of a cantilever tip is the cross correlation of its displacement time series signal with itself and describes the cantilever's movement at high and low frequency and can be normalised by the variance of the signal (NPAF). The NPAF takes the mathematical form [2.12]:

$$A(t) = \frac{\langle x(t_0)x(t_0 + \tau) \rangle}{\langle x^2 \rangle} \quad (2.4.3)$$

Where $x(t)$ is the cantilever tip position, $x(t+\tau)$ is the tip position after time lag τ and $\langle x^2 \rangle$ is the variance of the cantilever tip position. This can be related to the relaxation time of the fluid surrounding the cantilever as explained by Tassieri *et al* and covered in the previous section of this chapter. As described previously, the compound system of an overdamped cantilever tip in a Newtonian fluid can be approximately modelled as an ideal Kelvin-Voight mechanical system which has the characteristic relaxation time of a single decaying exponential. The normalised mean squared displacement (NMSD) $\Pi(t)$ of the cantilever tip is related to the NPAF of the tip by:

$$\Pi(t) + A(t) = 1 \quad (2.4.4)$$

The NPAF of a single decaying exponential function of the form $A(t) = e^{-\lambda t}$ is shown in Figure 2.4.5.

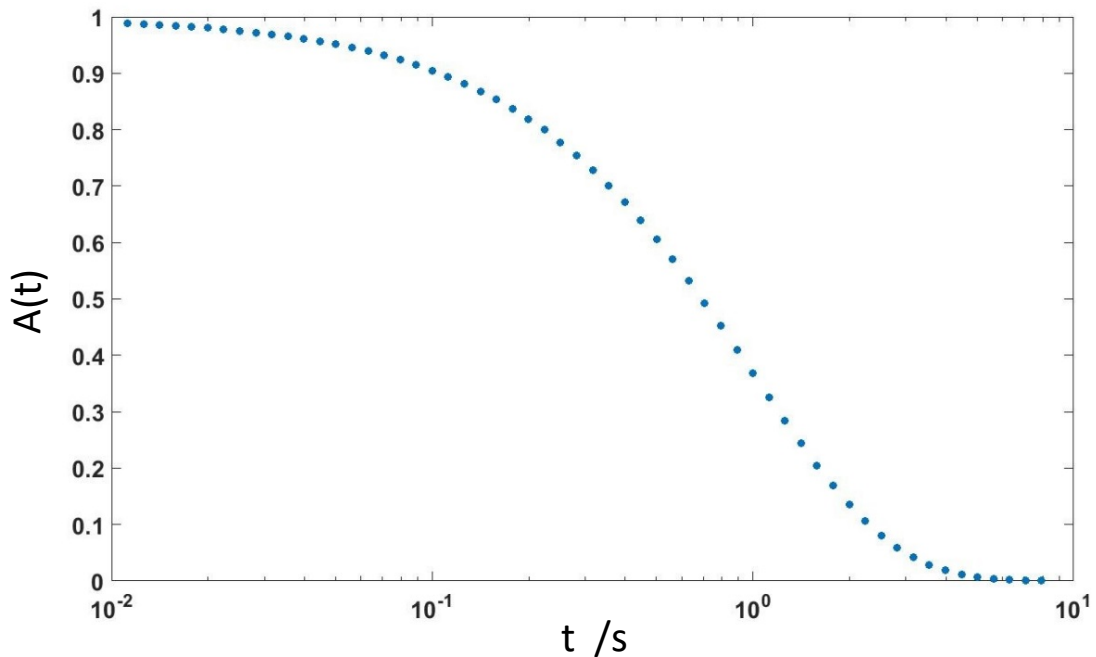


Figure 2.4.5. Normalised position autocorrelation function of the form $A(t) = e^{-\lambda t}$

One property of the PAF is that it is the Fourier transform of the PSD. As stated previously, when taking the PSD of the frequency spectrum, we take the magnitude squared of the signal and lose the phase information in the process. Similarly, we lose the phase information of the original signal when plotting the PAF. So, we may cross freely between the original time signal and the frequency spectrum, and between the PSD and the PAF. We cannot however reconstruct the original signal or frequency phase information from the PSD or NPAF alone.

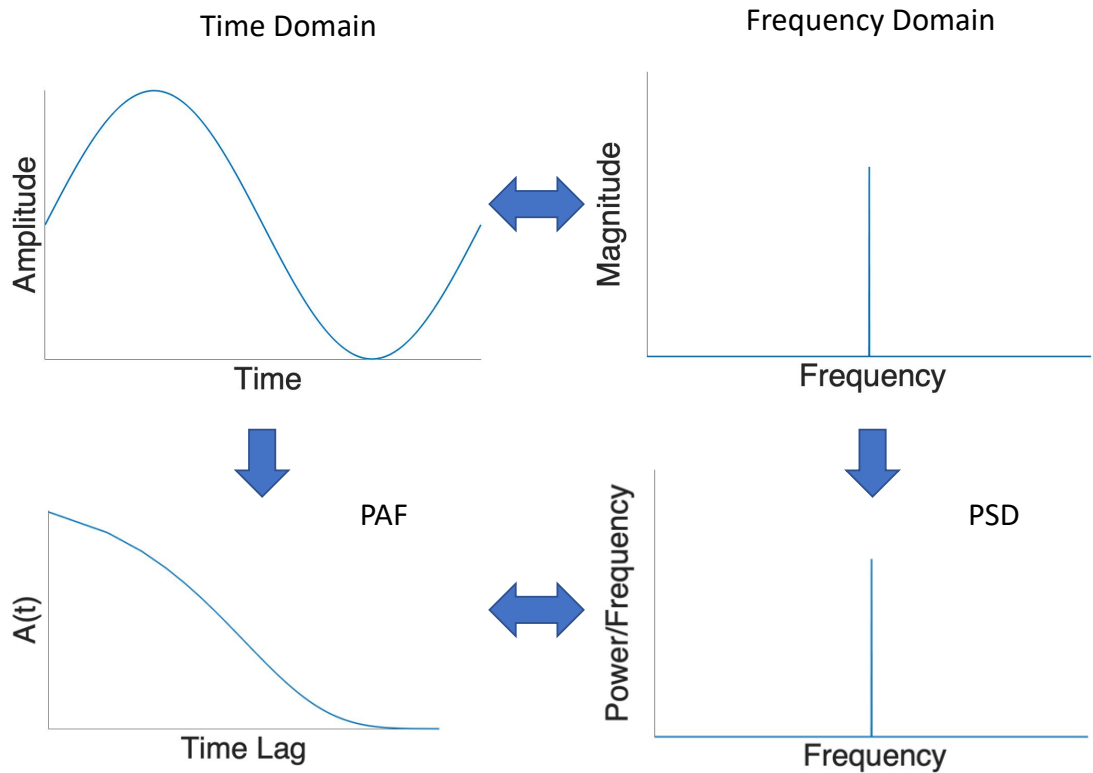
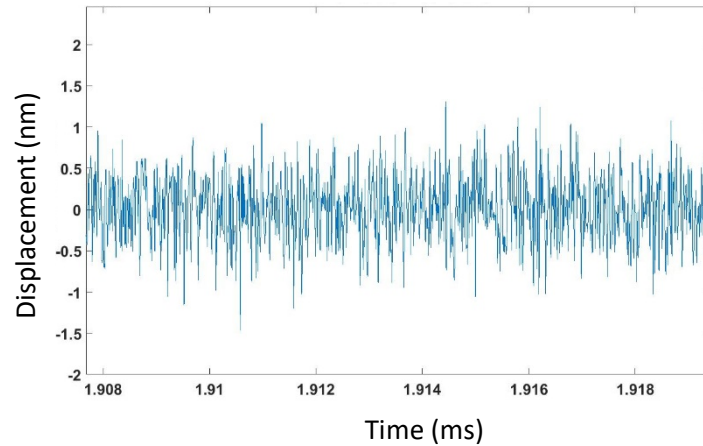


Figure 2.4.6. Plots showing the relationships between the time domain, frequency domain, PSD and PAF. One may move freely between the time and frequency domains, or the PSD the PAF. The original time series cannot be reconstructed from the PSD or the PAF without the original phase information.

Vibrating MEMS devices can be sorted into two classifications: passive and active. Active devices will have an actuator integrated into the design to drive the mechanical part that can take many different forms. Some common forms of device actuation include piezoelectric, magneto-motive, capacitive, or thermal bimorph [2.14],[2.15],[2.16],[2.17]. An analysis of some of these methods will be presented in **Chapter 3** of this thesis. Passive devices rely on the thermal excitation of the particles in the fluid or gas surrounding the device to drive the motion of the mechanical component. The trajectory of the thermally excited particles is Brownian in nature. The stochastic forces exerted on the device drive it to resonate, but also cause it to fluctuate randomly. This results in a noisy signal. If we take the Fourier transform of the noisy time series, we can still observe the harmonic components.

a.



b.

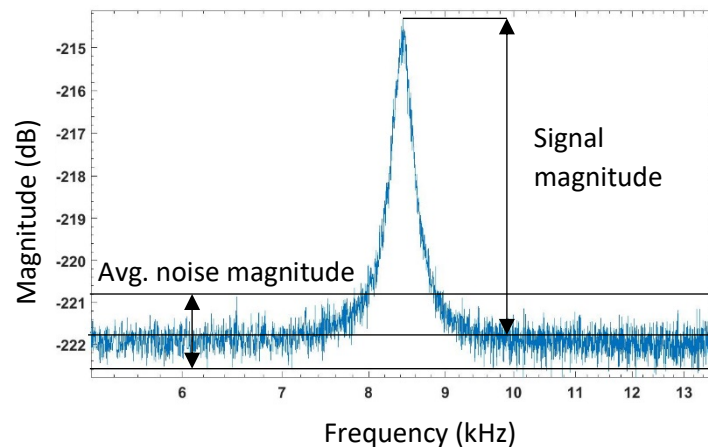


Figure 2.4.7 a & b MATLAB plot of the time series (a) and power spectrum (b) of a $1 \times 40 \times 0.5 \mu\text{m}$ MEMS PCD cantilever beam experiencing thermal fluctuations in air captured by the author. The signal-to-noise ratio is commonly expressed in decibels and can be obtained by subtracting the signal power from the average noise power: $\text{SNR}_{\text{dB}} = P_{\text{signal}(\text{dB})} - P_{\text{noise}(\text{dB})}$.

Figures 2.4.7 a & b show the time series and corresponding resonant peak of the displacement of a free end cantilever beam with the dimensions length $40 \mu\text{m}$, width $1 \mu\text{m}$, and thickness $0.5 \mu\text{m}$ experiencing thermal fluctuations suspended in air at room temperature. The ratio of the magnitude of the signal to the average magnitude of the noise floor of the measurement is defined as the signal to noise ratio (SNR) of the signal. It is commonly expressed in decibels and can be obtained by subtracting the signal power from the average noise power: $\text{SNR}_{\text{dB}} = P_{\text{signal}(\text{dB})} - P_{\text{noise}(\text{dB})}$. A higher SNR within a signal provides more useable information within the data. Typically, smaller devices will have a displacement closer to the noise floor of the measurement system and hence will suffer from a low SNR.

Another important aspect of MEMS resonant behaviour to note is the quality factor (Q) of the system.

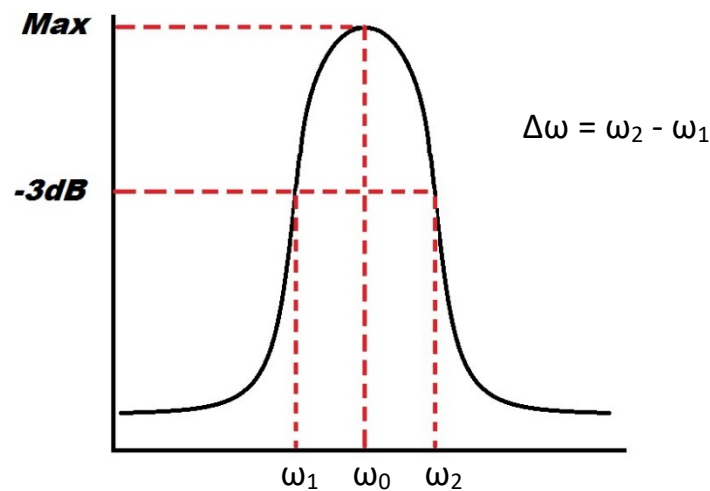


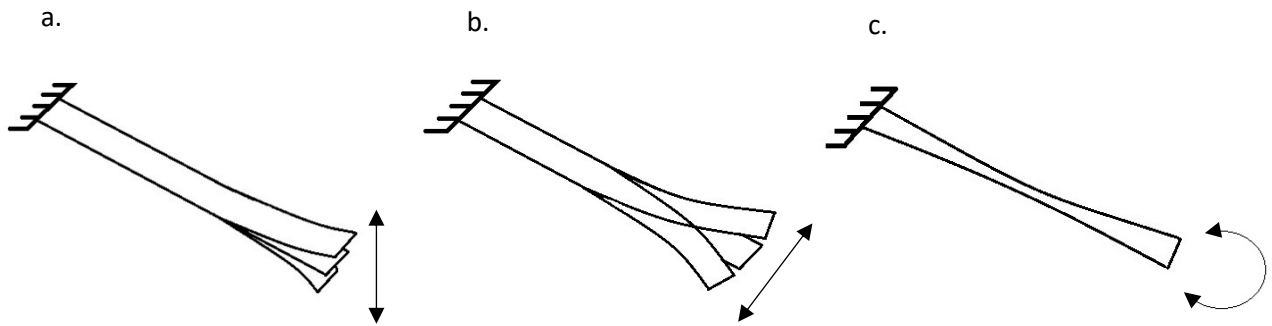
Figure 2.4.8. resonant peak showing -3dB bandwidth points. ω_1 & ω_2 are the lower and upper values respectively of the peak at -3dB down from the maximum peak value which occurs at ω_0 .

The Q of a resonant system can be described mathematically as:

$$Q = \frac{\omega_0}{\Delta\omega} \tag{2.4.5}$$

Where ω_0 is the resonant frequency and $\Delta\omega$ is the bandwidth of the signal at the half power, or -3dB point, as shown in **Figure 2.4.6**. The Q factor describes how damped a system is in terms of energy lost and energy stored. The higher the Q factor, the more energy is stored within the system. The lower the Q factor, the more energy is being lost, either from external dampening forces or from internal losses within the vibrating structure. MEMS devices with a higher Q factor and SNR will have a strongly defined resonant peak and thus are easier to detect.

In the case of MEMS resonant systems that are underdamped we will observe not only vertical displacement (known as flexural, or out-of-plane) but other different mechanical modes of vibration. The modes most commonly observed in MEMS cantilevers are lateral, or out-of-plane, which occurs laterally to the cantilever beam position and torsional, which occurs as a twisting motion along the length of the beam.



Figures 2.4.9 a, b & c. The flexural (a), lateral (b) and torsional (c) vibration modes of a free end cantilever beam.

Figure 2.4.9 a, b & c show the out-of-plane, in-plane and torsion modes of a free end cantilever beam. In a MEMS vibration system that is underdamped all the vibrational modes will have an impact on the data gathered, and evidence of their harmonic motion will be present in the frequency analysis of the device. If, however, there is a significant amount of dampening owing to external factors or the devices mechanical properties then the contributions from higher vibrational modes become insignificant.

2.5 Diamond as a prospective material for MEMS

Owing to its attractive mechanical and electrical properties, diamond is an attractive candidate for MEMS devices. Diamond's Young's modulus of up to 1220 GPa makes it the hardest material which is useful in applications where devices must withstand excessive shear forces [2.18]. The high Young's modulus coupled with its relatively low mass density of 3.5 g/cm^3 gives diamond a longitudinal

acoustic velocity of $19\,039\text{ m s}^{-1}$ making it an ideal material for devices such as resonators and surface acoustic wave (SAW) filters [2.19]. Diamond is also chemically and biologically inert; not only can it be applied in harsh environments with little device degradation, it will not interfere with any rare or fragile biological samples [2.20]. Another quality displayed by diamond is a high thermal conductivity of up to 21 W/cm.k , which is advantageous in terms of thermal management as a buildup of heat can potentially damage or destroy a device. Diamond exists as an allotrope of carbon where the atoms are arranged in a form known as face-centered cubic (FCC). Although diamond is not the only crystal structure of this form, the structure is known as the diamond lattice. The covalent bonds between carbon atoms in a diamond lattice are called sp^3 . It is the 3-dimensional sp^3 bonding structure that gives diamond its unique hardness and thermal properties.

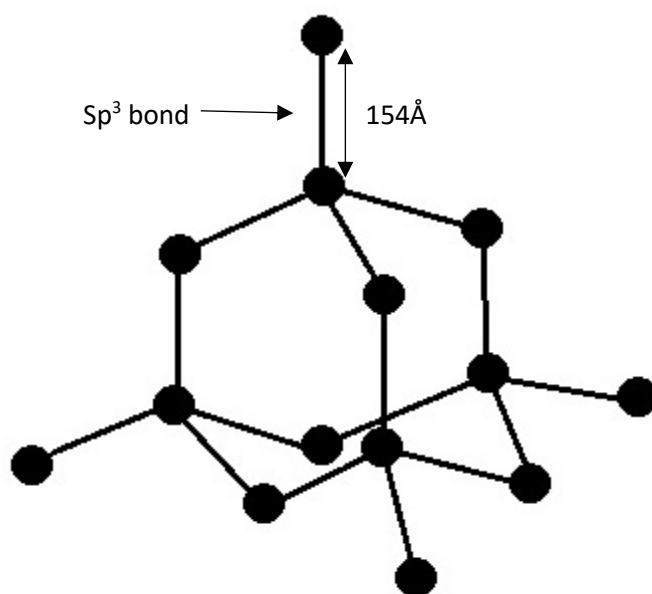


Figure 2.5.1 Diamond crystal lattice structure showing sp^3 bond length of 154 Å .

Although Diamond is found naturally in the earth's mantle, there exist synthetic manufacturing techniques including high pressure high temperature (HPHT) and chemical vapor deposition (CVD). Typically, HPHT involves diamond seeds pressed together with a high purity carbon source under high pressure and high temperature in order to recreate the conditions that produce diamonds naturally. This process is known to produce large diamonds and is popular with the gemstone industry and industrial applications where larger stones are beneficial. However,

owing to the large amounts of energy needed HPHT can be an expensive process. The development of the more cost-effective CVD process in recent years has made diamond a viable alternative material in the semiconductor and MEMS industries. In the CVD process, diamond seeds are prepared, typically on a silicon substrate, in a vacuum chamber and a hydrocarbon gas source is energized within the chamber. The hydrocarbon source can be energized by different methods including hot filament (HFCVD) and more recently microwave plasma (MPCVD). The carbon source, most commonly methane, decomposes and the carbon atoms are deposited onto the diamond seeds. The hydrogen source is important as the atomic hydrogen will selectively etch away the non-diamond carbon bonds, preparing the diamond to receive the carbon atoms in the diamond lattice configuration. The major advantages of CVD other than cost is the amount of control over the growth process available. Depending on the growth conditions parameters such as grain size, growth rate, thickness and area can be tailored for a specific purpose. In terms of mechanical properties, CVD diamond exhibits the same unique qualities as natural diamond such as high Young's modulus and high thermal conductivity. Diamond can be single crystal i.e. have a completely homogenous crystalline structure, or be poly-crystalline where regions of single crystal diamond known as grains are bound together by diamond-like carbon boundaries. The grain size can be controlled during the CVD growth by adjusting the flow rate of the carbon source during the process [2.21].

Intrinsic diamond is an excellent insulator owing to its large band gap. However, if during the CVD growth process a boron source is introduced into the growth chamber, a trace amount of boron atoms become present within the diamond lattice and the resulting boron doped diamond (BDD) will exhibit semiconductor to metallic conduction dependent on the doping concentration. The band structure describes the different energies that the electrons in a material can have. If the charge carriers are electrons the material is known as n-type and conduction occurs in the conduction band. If the carriers are holes, then the material is known as p-type and conduction occurs in the valence band. The band gap is the difference in energy levels between the valence band and the conduction band. Boron doped diamond has p-type conductivity. When a boron atom is introduced into the diamond lattice it acquires one of the carbon atom's electrons from the valence band. As a result, an extra hole becomes available. This increases the concentration of carriers in the valence band which can

contribute to current flow. For B-doped diamond, the activation energy of the doping decreases with doping concentration, resulting in semi-metallic conduction behavior at high boron doping concentrations [2.21].

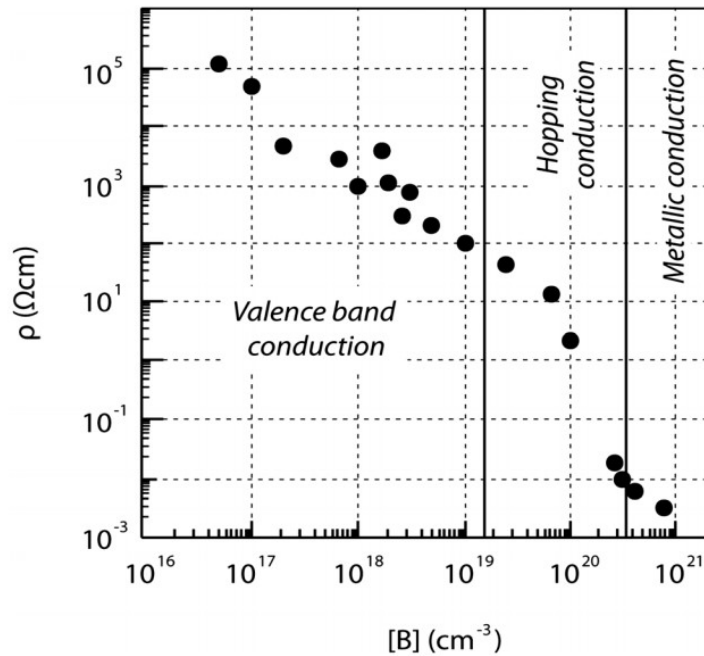


Figure 2.5.2. Resistivity as a function of boron content in BDD [2.22]

The resistivity of BDD is a function of the boron content as shown in **Figure 2.5.2**. Not only is BDD highly electrically conductive but it also exhibits piezoresistive qualities. That is, when subject to a mechanical stress or strain the resistivity will change. The combination of this and excellent mechanical properties makes BDD an ideal candidate for sensor applications, with the potential for devices to be fabricated of entirely of the same material. In BDD compressive stress increases conduction and tensile stress will decrease conduction. The figure of merit for a material's piezoresistivity is known as the gauge factor (GF) which is defined as the change in resistance ΔR for an applied strain ε [2.23]:

$$GF = \frac{\Delta R}{R} \cdot \frac{1}{\varepsilon} \quad (2.5.1)$$

With strain being defined as $\Delta L/L$: the total change in length of the structure divided by its original length. One of the piezoresistive mechanisms in BDD is known to be a result of the physical deformation in the crystal atomic structure causing a change in the material's band gap [2.21]. BDD exhibits a GF comparable with current silicon-based technologies. In a polycrystalline material, grain size has an effect on piezoresistance. It has been reported that the piezoresistive effect is larger in bulk grains than at the grain boundaries, hence, single crystal material will exhibit a more pronounced piezoresistive effect [2.24]. However, owing to the ease of fabricating with thin films (in comparison to bulk single crystal material), PCD remains the more attractive material for MEMS device fabrication.

2.6 Diamond Material Comparison Table

Material	Thermal Conductivity (W/cm.k)	Young's Modulus (GPa)	Gauge Factor Range
Single Crystal Diamond	24	1220	N/A
Poly-diamond	18-20	900-1220	N/A
B-doped Diamond	18-20	900-1220	30 - 1800
Single Crystal Silicon	1.57	190	30 - 1500
Silicon Nitride	0.19	385	N/A

Table 2.6.1 Table showing different diamond and silicon types, comparing some common material figures of merit [2.21][2.23][2.25].

2.7 Chapter Summary

In this chapter we have looked at the fundamental mechanics regarding cantilever beams and how they respond to different loading. We have determined the natural frequencies of free vibrational systems and applied the theory to cantilever type structures. The ability to determine the viscoelastic nature of a device's surroundings from measuring its displacement has been discussed. We have considered different aspects of vibration data analysis and how to apply these techniques to real displacement data. Diamond as a candidate for MEMS devices has been discussed, including its material and electrical properties in its intrinsic and boron doped forms along with material growth methods.

References

- [2.1] T. H. H. Bisplinghoff, R.L. Mar, J.W. Pian, *Statics of Deformable Solids*, First. Addison-Wesley, 1965.
- [2.2] R. C. Hibbeler, *Engineering Mechanics: Statics*, Second. Prentice Hall, 1974.
- [2.3] M. D. Thompson, W.T. Dahleh, *Theory of Vibration with Applications*. Pearson, 1997.
- [2.4] L. Meirovitch, *Analytical Methods in Vibrations*. Macmillan, 1967.
- [2.5] D. E. Newland, *Mechanical Vibration Analysis and Computation*. Longman Scientific and Technical, 1989.
- [2.6] J. R. Banerjee, "Explicit frequency equation and mode shapes of a cantilever beam coupled in bending and torsion," *Journal of Sound & Vibration*, vol. 224, no. 2, pp. 267-281, 1999.
- [2.7] J. Hutter and J. Bechhoefer, "Calibration of atomic force microscope tips," *Revised Scientific Instruments*, vol. 64, no. 7, p. 1868, 1993.

- [2.8] G Malegori, G Ferrini, " Tip-sample interactions on graphite studied using the wavelet transform", *Beilstein J Nanotechnol.* Vol 1: pp. 172-181, 2010.
- [2.9] M. Tassieri, "Microrheology with Optical Tweezers: Principles and Applications." *Pan Stanford Publishing*, 2016.
- [2.10] H. Butt, P. Siedle, K. Seifert, K. Fendler, T. Seeger, E. Bamberg, and A. L. Weisenhorn, "Scan speed limit in atomic force microscopy," *Journal of Microscopy*, vol. 169, pp. 75-84, 1992.
- [2.11] Y. Hirai, R. Mori, H. Kikuta, N. Kato, K. Inoue, and Y. Tanaka, "Resonance characteristics of micro cantilever in liquid," *Japanese Journal of Applied Physics*, vol. 37, no. 12 B, pp. 7064-7069, 1998.
- [2.12] M. Tassieri, R. M. L. Evans, R. L. Warren, N. J. Bailey, and J. M. Cooper, "Microrheology with optical tweezers: data analysis," vol. 115032, 2012.
- [2.13] T. King and A. F. Microscope, "Thermal cantilever calibration," *New Journal of Physics*, Vol. 2, no. 6, pp. 1-9, 2009.
- [2.14] A. Andrei, K. Krupa, M. Jozwik, P. Delobelle, L. Hirsinger, C. Gorecki, L. Nieradko, and C. Meunier, "AlN as an actuation material for MEMS applications. The case of AlN driven multilayered cantilevers," *Sensors Actuators*, vol. 141, pp. 565-576, 2008.
- [2.15] A. Boisen, S. Dohn, S. S. Keller, S. Schmid, and M. Tenje, "Cantilever-like micromechanical sensors," *Reports on Progress in Physics*, Vol 74, 2011.
- [2.16] O. Sidek, M. Miskam, H. Khaleed, and M. Alias, "Optimal Design of Capacitive Micro Cantilever Beam Accelerometer," *Modern Applied Science*, vol. 3, no. 9, pp. 16-28, 2009.
- [2.17] A. Hierlemann, O. Brand, C. Hagleitner, and H. Baltes, "Microfabrication Techniques for Chemical / Biosensors," *Proceeding of the IEEE* Vol. 91, no. 6, 2003.
- [2.18] O. A. Williams, a. Kriele, J. Hees, M. Wolfer, W. Müller-Sebert, and C. E. Nebel, "High young's modulus in ultra thin nanocrystalline diamond," *Chemical Physics Letters*, vol. 495, pp. 84-89, 2010.
- [2.19] J. Song, J. Sung, and H. Chang, "SAW Filter with AlN on Diamond," *Diamond and Related Materials*, Vol 1 pp. 1-13, 2008.

- [2.20] N. N. Efremow, M. W. Geis, D. C. Flanders, G. a. Lincoln, and N. P. Economou, "Ion-beam-assisted etching of diamond," *Journal of Vacuum Science and Technology*, Vol. 416, no. 1985, pp. 1-4, 1985.
- [2.21] R. S. Sussmann, *CVD Diamond for Electronic Devices and Sensors*. Wiley, 2009.
- [2.22] J. V. Macpherson, "A practical guide to using boron doped diamond in electrochemical research," *Physical Chemistry Chemistry Physics*, vol. 17, no. 5, pp. 2935-2949, 2015.
- [2.23] N. L. Privorotskaya, H. Zeng, S. Member, J. A. Carlisle, R. Bashir, and W. P. King, "Piezoresistive Microcantilevers From Ultrananocrystalline Diamond," *Journal of MEMS*, Vol. 19, no. 5, pp. 1234-1242, 2010.
- [2.24] M. Adamschik, R. Müller, P. Gluche, A. Flöter, W. Limmer, R. Sauer, and E. Kohn, "Analysis of piezoresistive properties of CVD-diamond films on silicon," *Diamond and Related Materials*, vol. 10, no. 9-10, pp. 1670-1675, 2001.
- [2.25] K. Takahata, *Micro Electronic and Mechanical Systems* IntechOpen, Croatia, Chapter 11 pp. 572, 2009.

Chapter 3: Literature Review

In recent history there have been advancements in the technological fields pertaining to cantilever based micro-rheology and polycrystalline diamond as material for MEMS devices. The following sub-chapters provide a brief history of the subject areas and an interrogation of recent published work relevant to the studies in this thesis.

3.1 Cantilever Hydrodynamics

The vibrations and frequency response of a cantilever beam in vacuum have been investigated extensively in literature and accurate models for their behaviour have been reported [3.1], [3.2]. However, when a cantilever is submerged in a fluid its behaviour becomes more complex than the vacuum model owing to the complex forces exerted on the cantilever structure by fluid-cantilever interaction. This interaction is known as the hydrodynamic force. It is the characterisation of the hydrodynamic force that becomes the main challenge for characterising the behaviour of submerged cantilever beams.

Some of the first innovators in characterising the cantilever beam hydrodynamic forces were Butt *et al* in their investigation of an atomic force microscopy scan speed limit [3.3]. Butt *et al* showed that a submerged cantilever could be approximately modelled as an equivalent mass-spring-damper system. They compared the piezo-electrically driven motion of triangular shaped silicon nitride cantilevers with varying dimensions (100-200 μm long) in a moderate vacuum, air, water, hexane and hexadecane. As expected, they observed dampening of the cantilever vibrations when submerged. They speculated that as the cantilever moves through the liquid, some of the liquid is dragged along with it. They modelled the fluid loading on the cantilever as an increased effective cantilever mass. Using their term for increased effective mass they calculated damping constants for their experimental cantilevers. Comparing these damping constants to the damping of a sphere moving in a liquid as per Stokes law [3.4] they were able to find the 'effective radii' of the cantilevers and found them to be in rough agreement with the dimensions of the cantilevers. This showed the potential for a submerged cantilever to be modelled as a sphere suspended in fluid, the mechanical model for which is a simple mass-spring-damper system as shown in **Figure 3.1.1**.

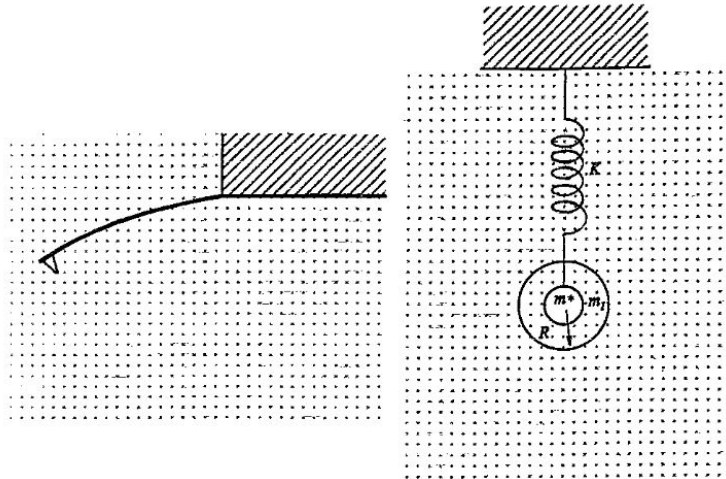


Figure 3.1.1 Submerged atomic force microscope (AFM) cantilever tip (left) and suspended sphere modelled as a spring with end mass (right) [3.3].

This method was verified and expanded on by Chen *et al* who also used the suspended sphere model to predict the resonance response of submerged atomic force microscope cantilevers [3.5]. They confirmed that the cantilever geometrical factor present in the hydrodynamic loading was constant in different mediums for any given cantilever. They also reported corrections that take into account that the hydrodynamic force loading is significantly greater in fluid than it is in gases.

The sphere suspended in fluid model was elaborated on by Hirai *et al* in their report on the resonance characteristics of micro cantilevers in liquid [3.6]. Hirai *et al* modelled their cantilever as not just one sphere but as a string of spheres, as demonstrated in **Figure 3.1.2**.

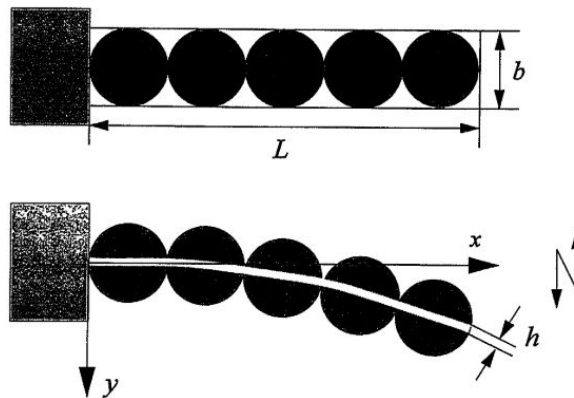


Figure 3.1.2 Schematic representation of the cantilever modelled as a string of spheres, as presented by *Hirai et al* [3.6].

This was based on an approach that models a vibrating plate as a string of spheres, with the diameter of the spheres relating to the width of the plate. This method allowed the hydrodynamic drag force to be calculated with greater accuracy. They observed the frequency spectrum of thermally excited silicon nitride cantilevers $\sim 200\text{-}400\ \mu\text{m}$ long in air, water and acetone. Their experimental results compared well to their numerically calculated results but observed that this method overestimates the hydrodynamic drag force when applied to microstructures at high frequencies.

Currently, the most widely accepted and applied model for characterising the hydrodynamic force on submerged cantilevers is that presented by Sader [3.7]. Sader introduced the hydrodynamic function, $\Gamma(\omega)$, as a general theory for the frequency response of cantilever beams of arbitrary dimension submerged in an arbitrary fluid. In contrast to the previously mentioned spherical methods, this method rigorously accounted for cantilever geometry. Sader stipulated some assumptions that must be true for this method to work: the cross section of the beam must be uniform over the beams length, the length of the beam greatly exceeds its nominal width, the beam is an isotropic linearly elastic solid and internal frictional effects are negligible, and the amplitude of vibration of the beam is far smaller than any length scale in the beam geometry. Given these assumptions, it would seem that Sader's method is ideal for characterising the hydrodynamic force on micro-cantilevers, however it is important to note that this, and the previous methods, apply only to Newtonian fluids.

3.2 Cantilever Micro-rheology

We now look at reported methods of extracting an arbitrary fluid's mechanical properties from submerged micro-cantilevers. Some of the main points of focus for researching micro-cantilevers for micro-rheology are the potential for revealing higher frequency data than conventional methods and the capacity to explore the properties of relatively small and potentially rare or precious samples. Micro-rheology also allows for rheological analysis of soft matter to be performed *in situ*. To date, reported methods almost exclusively rely on the work of Sader and utilise his hydrodynamic function in some form. Micro-cantilevers have been employed as *in-situ* rheometers for characterising complex fluids such as oils, and viscometers to varying degrees of success [3.8]. Atomic force microscopy (AFM) tools have also been used to observe cantilever-fluid (or soft-matter) interaction as well as to characterise the mechanical properties of cells [3.9].

Papi *et al* show in their study of fluid viscosity determination by atomic force microscopy that they were able to describe a method of relating fluid viscosity and cantilever resonant frequency using an approximation of Sader's hydrodynamic function [3.10]. Their calculations were dependent on two variable coefficients: α , dominated by the cantilever thickness and β , dominated by the cantilever width/thickness ratio. Their investigation revealed that a cantilever's resonant frequency is strictly characterised by its thickness, and that the cantilevers width/thickness ratio is a less sensitive parameter and can be approximated to a constant. Thus, by simulating a spread of β values and observing no significant change in a reference fluid's viscosity measurement, the parameter α could be measured by setting β at a constant value. Hence, by using a reference measurement in a fluid of known viscosity, further measurements required no knowledge of cantilever geometry. Their results compared favourably to previously published data [3.11], however, this method revealed fluid viscosity at only the resonant frequency of the cantilever and many measurements had to be taken to build a dataset across the frequency spectrum.

Maali *et al* expanded on Sader's work [3.12]. They showed experimentally that the theoretical hydrodynamic function was not able to account for energy dissipated by the liquid motion induced by the cantilever oscillation. As a result, they observed that at higher modes of vibration the measured fluid viscosity was

reduced when compared to the theoretical model. It was explained that this discrepancy could be due to the hydrodynamic function assuming that the cantilever oscillations are transverse only. This two-dimensional fluid interaction was interrogated, however no clear analytical solution for the problem was presented. In an attempt to understand a three-dimensional model, a numerical analysis using the three-dimensional Navier-Stokes equation was presented, and the solutions showed favourable qualitative comparison with experimental results. Belmiloud *et al* explored rheological behaviour with micro-cantilevers using Maali's parameters [3.13]. In their work, an analogy was made between cantilever beam dynamics in viscous fluid and a second order low pass filter. That is, the contribution of higher modes of vibration were considered negligible and the fundamental mode was considered dominant. This significantly simplified the transfer function of the system. The simplified transfer function was then used to extract the hydrodynamic drag force coefficients of the cantilever at different frequencies, from which the fluid viscosity and density were analytically extracted. Results for the rheological properties of silicone oils tested were in good agreement with known values within the explored frequency range, although the explored frequency range was only up to 600Hz - well within the range of conventional micro-rheology [3.14]. It is interesting to note that for these measurements it was possible to extract fluid properties without the need for a well-defined resonant peak in the cantilever frequency spectrum. This method can then be used for analysing fluids with a relatively high viscosity when compared to other methods that require a higher quality factor ($Q > 1$) in the cantilever response [3.15]. Youssry *et al* reported that they were able to take the methods employed by Belmiloud and by applying further modifications to the Maali parameters explored fluid properties up to 8kHz [3.8]. However, reported a relatively high error between their measurements and known values, and postulate issues regarding cantilever geometry non-uniformity as a result of their manufacturing process and possible irregularities with their experimental setup.

There is a clear trend in published data in the field of cantilever micro-rheology of trying to fit cantilever frequency response data to proposed models with varying results. It is apparent that as experiments extend into the high frequency range these models become inadequate at representing cantilever dynamics and continuous modifications to model parameters must be taken into account.

3.3 Diamond MEMS

Owing to its excellent mechanical and electrical properties, synthetic diamond has become a main contender for MEMS devices over the last few decades, including RF systems, sensors, resonators and switches. Advancements in CVD technology has driven down the cost of manufacturing, fuelling extensive research into next-generation diamond based devices as possible alternatives to silicon-based technologies [3.16], [3.17].

Sepulveda *et al* reported on high-performance polycrystalline diamond micro-resonators [3.18]. With comparable silicon-based resonators unsuitable for high-end RF MEMS applications, the study focused on the resonant frequency and quality factor of devices which are two of the defining factors in characterising resonator performance. The reported devices were polycrystalline diamond micro-cantilevers of width, thickness and length 10 μm , 0.6 μm and 100-500 μm . Their diamond films were grown by microwave plasma CVD and highly polished. The diamond was grown on a sacrificial SiO_2 layer which was wet etched to release the cantilevers. This helped minimise undercut. The diamond was etched in an oxygen based plasma with etch rates between 20 - 40 nm/min reported, yielding 90° anisotropic structures. The cantilevers were actuated by a piezoelectric transducer clamped to the substrate, and the devices were excited whilst subject to a vacuum at 1×10^{-5} torr to minimise air dampening. The devices were detected by a laser interferometer system. Q factors of up to 116000 were reported and resonant frequency up to 50 kHz. In comparison, the highest reported Q for similar silicon based devices was 5846 [3.19]. Tao *et al* improved on this high Q figure with similar devices fabricated from single-crystal diamond samples, also grown by CVD [3.20]. They reported Q factors exceeding one million for a device with dimensions width, thickness and length 12 μm , 0.66 μm and 240 μm . They presented a unique fabrication method: first the diamond sample was bonded front-side to a handle substrate. The diamond sample was then backside etched with an oxygen-chlorine based plasma to thin it down as low as 100nm retaining a surface roughness less than 1 nm Ra. The cantilevers were then patterned in the diamond membrane. The study compared the diamond devices to silicon devices with the same geometry and found a consistent Q factor increase of one or two

orders of magnitude. Gaidarzhy *et al* also reported high Q factors in their devices, but were able to achieve this at frequencies up to 1.441 GHz by employing a device with unique geometry as demonstrated in **Figure 3.3.1** [3.21].

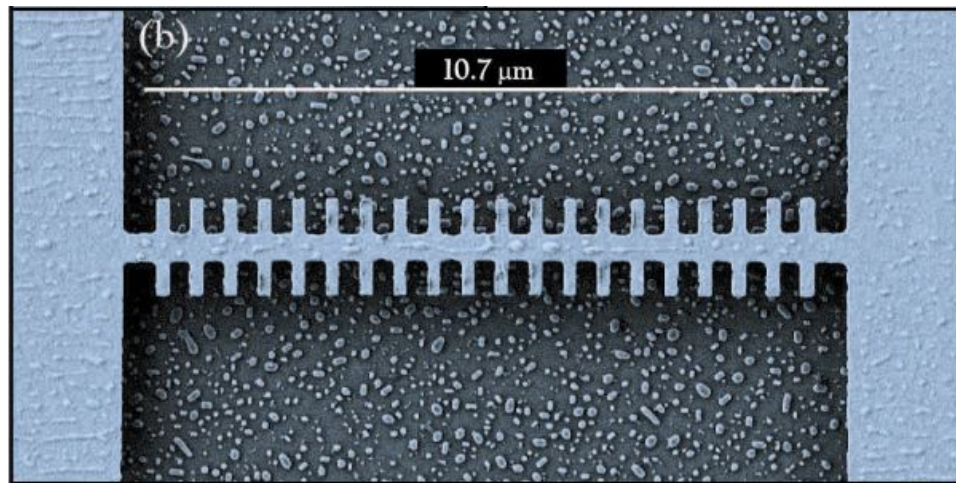


Figure 3.3.1 SEM image showing unique double clamped cantilever geometry employed by Gaidarzhy *et al* [3.21]. The smaller cantilevers were tuned to constructively interfere with the perpendicular main beam.

These devices, made from CVD polycrystalline diamond, exhibited an fQ product (resonant frequency \times Q factor) of 1.46×10^{13} , similar to the highest ever reported in literature for a micro-resonator made from any material [3.28]. This exemplified the mechanical properties of polycrystalline diamond and showed that there was no significant distinction between polycrystalline and single-crystal diamond mechanical properties for MEMS applications. Kara *et al* explored the nano-fluidics of single crystal diamond mechanical resonators [3.15]. Their devices were simple cantilever beam structures fabricated from single-crystal diamond, as shown in **Figure 3.3.2**. They hypothesised that the smooth and inert surface of single-crystal diamond would allow for reduced drag and therefore increase resonator performance under heavy fluid loading. Owing to fabrication issues around forming single-crystal suspended cantilever structures, their cantilevers were fabricated using focussed ion beam (FIB) technology. This resulted in a triangular beam cross section, also displayed in **Figure 3.3.2**.

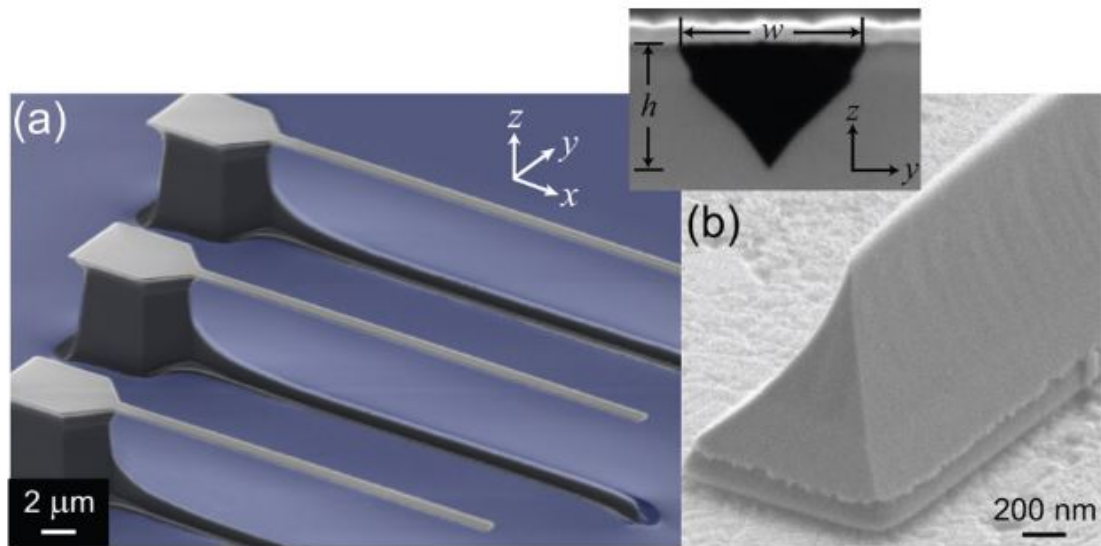


Figure 3.3.2 SEM images showing single crystal diamond simple cantilever design fabricated by FIB by *Kara et al.* Also shown is triangular beam cross section (insert) [3.15].

Their experimental procedure involved observing the cantilevers' thermal fluctuations in air and water and comparing the measured frequency and Q factor to their theoretical model (based on the Sader model). Their data was somewhat in good agreement with the theoretical model for frequency but underestimated Q factor. Discrepancies were attributed to cantilever geometry; their model was based on an oscillating cylinder and did not consider the triangular cantilever cross section (**Figure 3.3.2 inset**).

One of the more unique ways synthetic diamond has been implemented in MEMS devices is as a piezo-resistor. Diamond can be doped during the growth process with boron, and the resulting material may be both semi-conducting and piezo-resistive. This makes it an ideal candidate for MEMS sensor applications: displacement of mechanical parts made from doped diamond can be detected by monitoring its varying electrical resistance. The work of Darrel *et al* showcased a boron doped polycrystalline diamond pressure sensor [3.22]. Their device consisted of a 5 μm thick un-doped PCD membrane with boron doped PCD resistors deposited on the surface. Diamond growth was achieved by CVD. The change in current through the resistors was measured when the membrane was subject to an applied stress, and they found the gauge factor (the fractional change in the

resistance to fractional change in the length of a strain gauge) of their device to be approximately 7. Darrel *et al* also included data from single boron doped CVD piezo-resistors stressed on a silicon substrate, and from these resistors they found a correlation between a larger PCD grain size and larger gauge factor. They also reported an increase in CVD resistivity with temperature. Janssens *et al* more recently made a similar membrane pressure sensor device [3.23]. Theirs was significantly thinner, only 150 nm thick, and was made entirely of boron doped PCD. They concluded that the piezoresistive response of their membrane as a function of differential pressure was highly linear and sensitive, up to 0.6 %/bar, nearly a 50 % increase on previous reported values [3.24]. Kulha *et al* fabricated PCD piezo-resistors onto the base of silicon based cantilevers to form pressure sensors [3.25]. They made an extensive study into the sensor's parameters such as deformation sensitivity, contact resistance, and gauge factor and resistance temperature dependency. They found that the gauge factor increased as the boron doping level decreased, and that the gauge factor decreased with increasing temperature (Figure 3.3.3).

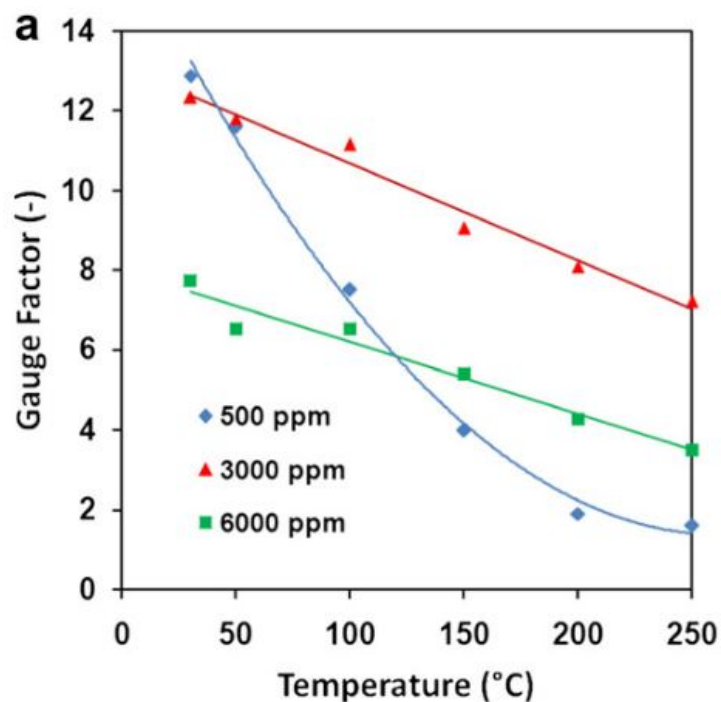


Figure 3.3.3 Plot showing gauge factor as a function of temperature in boron doped polycrystalline diamond piezoresistive cantilevers fabricated by Kulha *et al* [3.25].

They used finite element analysis (FEA) to model the stress distribution in the piezo-resistors and the gauge factor. The FEA results compared well to experimental results, however the simulations did not take into account the effect the added piezo-resistors had on the strain of the entire structure. The highest gauge factor recorded in this study was 12.6 which falls short when compared to similar silicon based devices which have gauge factor of + 20 [3.26]. Privorotskaya et al fabricated piezo-resistive cantilevers entirely from PCD, utilizing a sample comprising of an intrinsic PCD layer with a boron doped layer grown on top [3.27]. A device made exclusively from PCD retains all the favourable mechanical and electrical properties of diamond for use in applications, such as chemical inertness and thermal stability. Silicon devices may suffer from biocompatibility issues [3.28]. Their devices were U shaped suspended cantilever structures ranging from around 300-400 μm in length and 1 μm thick, as shown in **Figure 3.3.4**.

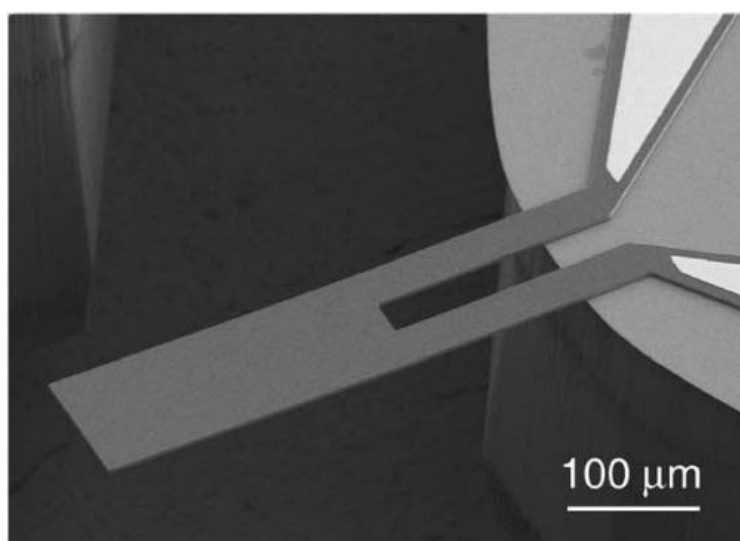


Figure 3.3.4 SEM image of U shaped boron doped ultrananocrystalline diamond cantilever fabricated by Privorotskaya *et al* [3.27]

The diamond material was patterned with SiO_2 and etched in an oxygen based plasma, with no specific etch rate reported. Ohmic contacts were formed using an Au/Cr stack, the Cr serving as an adhesion layer. A back-side through-wafer etching process was used to release the cantilever. They used a nano-positioner to deflect the cantilever beam and observe the change in resistance through the structure using a Wheatstone bridge circuit. They reported that their cantilever gauge factor was not significantly temperature dependent and that the piezo-resistive temperature coefficient for the devices was close to zero. This

contradicted previous reports including Kulha *et al*, and they stated that the reason for this was the significantly smaller grain size of the PCD used in the study. A deflection sensitivity of 0.19 m Ω / Ω per micrometre of deflection was reported for these devices.

3.4 Thesis Aims

A robust, low-cost micro-rheometer for *in-situ* characterisation of complex fluids across a range of frequencies is of significant interest to the field. It has been shown that polycrystalline diamond, in intrinsic and boron-doped form, retains many of the attractive mechanical and electrical properties of single crystal diamond, yet is cheaper to manufacture and can be produced as a thin film, making it easier for micro-processing.

Here we report on the investigation of polycrystalline diamond as a material for MEMS devices, specifically for passive micro-rheology and sensor applications. This includes the development of the fabrication and characterisation of two related devices: an intrinsic PCD micro-cantilever for passive micro-rheology, and a boron-doped PCD piezo-resistive micro-cantilever for sensor applications.

Device fabrication methods and process development pertaining to PCD-on-silicon samples, and subsequent device characterisation will be presented including:

- development of a top-side cantilever release process with minimal undercut
- analysis of the thermal fluctuations of intrinsic PCD micro-cantilevers in air and water
- a data analysis method for extracting a fluid's viscoelastic properties from the power spectrum of the thermal fluctuations of a submerged micro-cantilever
- electrical characterisation of boron-doped diamond samples
- characterisation and analysis of the piezoresistive effect in boron-doped PCD piezo-resistive micro-cantilevers

References

- [3.1] S. Timoshenko, *Vibration Problems in Engineering*, Second Edi. D. Van Nostrand Company, 1990.
- [3.2] M. D. Thompson, W.T. Dahleh, *Theory of Vibration with Applications*. Pearson, 1997.
- [3.3] H. Butt, P. Siedle, K. Seifert, K. Fendler, T. Seeger, E. Bamberg, and A. L. Weisenhorn, "Scan speed limit in atomic force microscopy," *Journal of Microscopy*, vol. 169, pp. 75-84, 1992.
- [3.4] M. Tassieri and P. S. Publishing, *Microrheology with Optical Tweezers: Principles and Applications*. Pan Stanford Publishing, 2016.
- [3.5] G. Y. Chen, R. J. Warmack, T. Thundat, D. P. Allison, and A. Huang, "Resonance response of scanning force microscopy cantilevers," *Review of Scientific Instruments*, Vol. 65, no. 8, pp. 2532-2537, 1994.
- [3.6] Y. Hirai, R. Mori, H. Kikuta, N. Kato, K. Inoue, and Y. Tanaka, "Resonance characteristics of micro cantilever in liquid," *Japanese Journal of Applied Physics*, vol. 37, no. 12 B, pp. 7064-7069, 1998.
- [3.7] C. P. Green and J. E. Sader, "Torsional frequency response of cantilever beams immersed in viscous fluids with applications to the atomic force microscope," *Journal of Applied Physics*, vol. 92, no. 10, pp. 6262-6274, 2002.
- [3.8] M. Youssry, B. Caillard, C. Ayela, C. Pellet, I. Dufour, and D. Int. Assoc. Sci. Technol, "Microrheology of Newtonian fluids using microcantilever," *NANA 2010*, pp. 540-546, 2016.
- [3.9] M. Lehrbette, A dos Santos, Y. Hari-Gupta, N. Fili, C. P. Toseland, I. A. T. Schapp, "Atomic Force Microscopy micro-rheology reveals large structural inhomogeneities in single cell-nuclei", *Scientific Reports*, Vol 7:8116, 2017.
- [3.10] M. Papi, G. Maulucci, G. Arcovito, P. Paoletti, M. Vassalli, and M. De Spirito, "Detection of microviscosity by using uncalibrated atomic force microscopy cantilevers," *Applied Physics Letters*, vol. 93, no. 12, 2008.

- [3.11] P. I. Oden, G. Y. Chen, R. A. Steele, R. J. Warmack, and T. Thundat, "Viscous drag measurements utilizing microfabricated cantilevers," *Applied Physics Letters*, vol. 68, no. 26, pp. 3814-3816, 1996.
- [3.12] A. Maali, C. Hurth, R. Boisgard, C. Jai, T. Cohen-Bouhacina, and J. P. Airm, "Hydrodynamics of oscillating atomic force microscopy cantilevers in viscous fluids," *Journal of Applied Physics*, vol. 97, no. 7, 2005.
- [3.13] N. Belmiloud, I. Dufour, A. Colin, and L. Nicu, "Rheological behavior probed by vibrating microcantilevers," *Applied Physics Letters*, vol. 92, no. 4, pp. 1-4, 2008.
- [3.14] M. Tassieri, F. Greco, P. A. Netti, P. L. Maffettone, and T. Bicanic, "Microrheology with Optical Tweezers: Measuring the relative viscosity of solutions 'at a glance'," *Scientific Reports* Vol 5, pp. 0-6, 2015.
- [3.15] V. Kara, "Nano fluidics of Single-Crystal Diamond Nanomechanical Resonators," *Nano Letters*, Vol 15 (12), pp 8070-8076, 2015.
- [3.16] O. Auciello and C. Gudeman, "Are diamonds a MEMS best friend?," *IEEE Microwave Magazine*, vol. 8, no. 6, pp. 61-75, 2007.
- [3.17] O. a. Williams, "Nanocrystalline diamond," *Diamond and Related Materials*, vol. 20, no. 5-6, pp. 621-640, 2011.
- [3.18] N. Sepúlveda, J. Lu, D. M. Aslam, S. Member, and J. P. Sullivan, "High-Performance Polycrystalline Diamond," *Journal of MEMS*, Vol. 17, no. 2, pp. 473-482, 2008.
- [3.19] S.-S. Li, Y.-W. Lin, Y. Xie, Z. Ren, and C. T.-C. Nguyen, "Micromechanical hollow-disk ring resonators," *IEEE International MEMS Conference*, pp. 821-824, 2004.
- [3.20] Y. Tao, J. M. Boss, B. A. Moores, and C. L. Degen, "Single-crystal diamond nanomechanical resonators with quality factors exceeding one million," *Nature Communications*, vol. 5, pp. 1-8, 2014.
- [3.21] A. Gaidarzhy, M. Imboden, P. Mohanty, J. Rankin, and B. W. Sheldon, "High quality factor gigahertz frequencies in nanomechanical diamond resonators," *Applied Physics Letters*, vol. 91, no. 20, pp. 1-5, 2007.

- [3.22] D. R. Wur, J. L. Davidson, S. Member, W. P. Kang, and D. L. Kinser, "Polycrystalline Diamond Pressure Sensor," *Journal of MEMS*, Vol. 4, no. 1, pp. 34-41, 1995.
- [3.23] S. D. Janssens, S. Drijkoningen, and K. Haenen, "Ultra-thin nanocrystalline diamond membranes as pressure sensors for harsh environments," *Applied Physics Letters*, Vol. 73107, pp. 2012-2016, 2016.
- [3.24] M. Deguchi, N. Hase, M. Kitabatake, H. Kotera, S. Shima, and M. Kitagawa, "Piezoresistive property of CVD diamond films," *Diamond and Related Materials*, vol. 6, no. 2-4, pp. 367-373, 1997.
- [3.25] P. Kulha, O. Babchenko, A. Kromka, M. Husak, and K. Haenen, "Design and fabrication of piezoresistive strain gauges based on nanocrystalline diamond layers," *Vacuum*, vol. 86, no. 6, pp. 689-692, 2012.
- [3.26] S. Yang and N. Lu, "Gauge factor and stretchability of silicon-on-polymer strain gauges," *Sensors (Switzerland)*, vol. 13, no. 7, pp. 8577-8594, 2013.
- [3.27] N. L. Privorotskaya, H. Zeng, S. Member, J. A. Carlisle, R. Bashir, and W. P. King, "Piezoresistive Microcantilevers From Ultrananocrystalline Diamond," *Journal of MEMS*, Vol. 19, no. 5, pp. 1234-1242, 2010.
- [3.28] W. Yang, O *et al* "DNA-modified nanocrystalline diamond thin- films as stable, biologically active substrates," *Nature*, pp. 253-258, 2002
- [3.29] Nguyen *et al* "MEMS technology for timing and frequency control," *IEEE Transactions on Ultrasonics Ferroelectrics and Frequency Control*, 54(2), 2007

Chapter 4: Fabrication Methods

The micro and nano-scale fabrication industry hinges on the ability to create features with metals, semiconductors and other materials with precision down to micro and nano-scale lengths. In order to achieve this, engineers must utilize state of the art fabrication techniques. There exists no standard fabrication method for MEMS devices, and many of the techniques applied in industry and research originate in the semiconductor industry. The fabrication methods and equipment described in this chapter pertain to the devices explored in this body of work. However, it is by no means an exhaustive list of methods and the field of fabrication continues to expand.

4.1 Lithography

In the device fabrication field, lithography is the method by which substrates can be patterned and serves as the basis for structuring materials on the micro and nano-scale. One of the most commonly used methods of lithography is photolithography. In photolithography, an ultra violet (UV) sensitive material called photoresist, or resist, is applied to a substrate. For application purposes, the resist is prepared as a solution with a solvent. An amount of resist is applied to the substrate via a pipette, and the substrate is spun at a pre-determined RPM to achieve a uniformly level application. Post-spinning, the sample and resist are baked on a hotplate or in an oven to evaporate the remaining solvent and solidify the resist. The final thickness of the resist depends on the viscosity of the resist and the spin speed. Areas of the resist are then selectively exposed to UV light by means of a hard mask placed between a light source and the resist coated substrate as shown in **Figure 4.1.1**. The substrate is then submerged in a solution known as developer which is used to affect the patterning. There exists two iterations of resist; positive and negative. When positive resist is exposed to UV light it becomes soluble in developer. Conversely, negative resist is soluble in developer and becomes insoluble upon UV light exposure. Once the unwanted resist has been removed by the developer the desired pattern remains on the substrate which can be used for further processing.

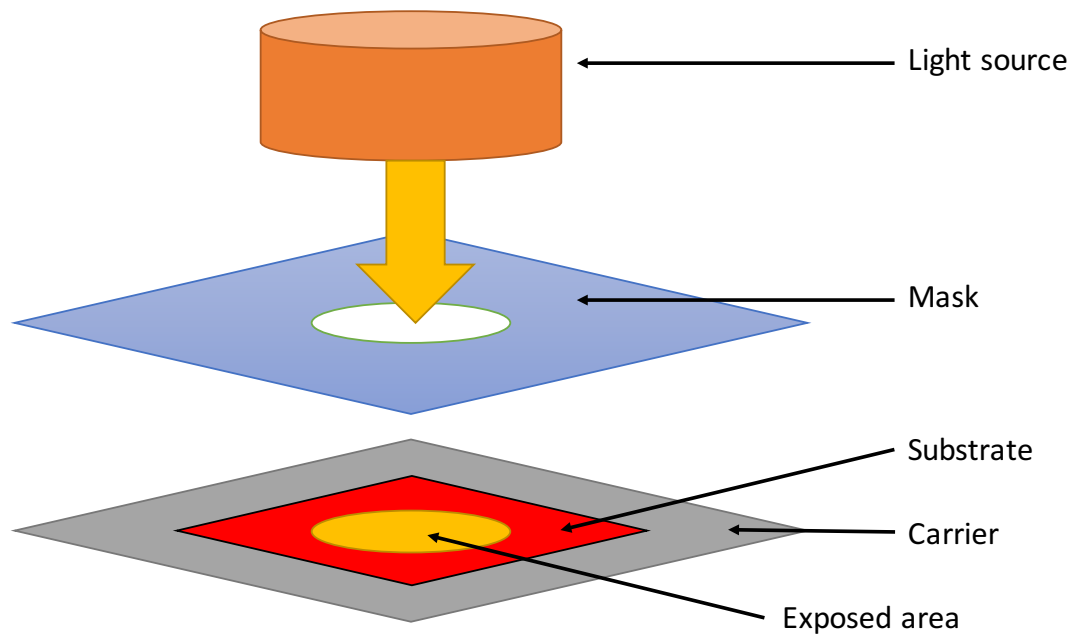


Figure 4.1.1 Diagram of photolithography process. The hard mask guides UV light onto a UV sensitive resist coated substrate.

The resolution of photolithography can be affected by several factors including: variation in overall resist thickness, non-uniformity in resist thickness, bake temperatures and exposure energies. However, in an ideal situation where the afore mentioned factors are optimized, the theoretical limit of photolithography is determined by the wavelength of the exposing light [4.1].

An alternative process, developed in the mid-20th century as the successor to photolithography, is electron beam lithography (EBL). EBL employs radiation sensitive resist which is exposed by a beam of electrons. One of the main benefits of EBL (in addition to the high-resolution factor) is that no mask is required to write patterns on the resist. Instead, the electron accelerator is controlled by computer software, and the pattern is built up as the electron beam scans across the substrate. This method lends itself well to designs that are frequently changing, wherein creating a new photo-mask each time would be impractical. Patterns can be created on computer aided design (CAD) software by the user and

passed to the EBL tool for processing. The user defines operating parameters such as the electron beam spot size, step size and exposure energy, or dose. The EBL tool directs the electron beam in a raster scan across the substrate, exposing each spot then moving by the predefined step and exposing again as demonstrated in **Figure 4.1.2**. One issue that can occur during the EBL process is charge trapping. This is where negative charge build-up can occur in an insulating substrate. This leads to beam deflection. To alleviate this, a conductive layer can be deposited over the resist. This helps dissipate the charge away from a concentrated area by providing the electrons with a path to ground [4.2]. Theoretically, nm resolution can be achieved by EBL, however the technique is still subject to the same previously mentioned processing limitations as photolithography. Owing to the high costs associated with EBL, photolithography is still a widely used manufacturing process for MEMS and semiconductor devices.

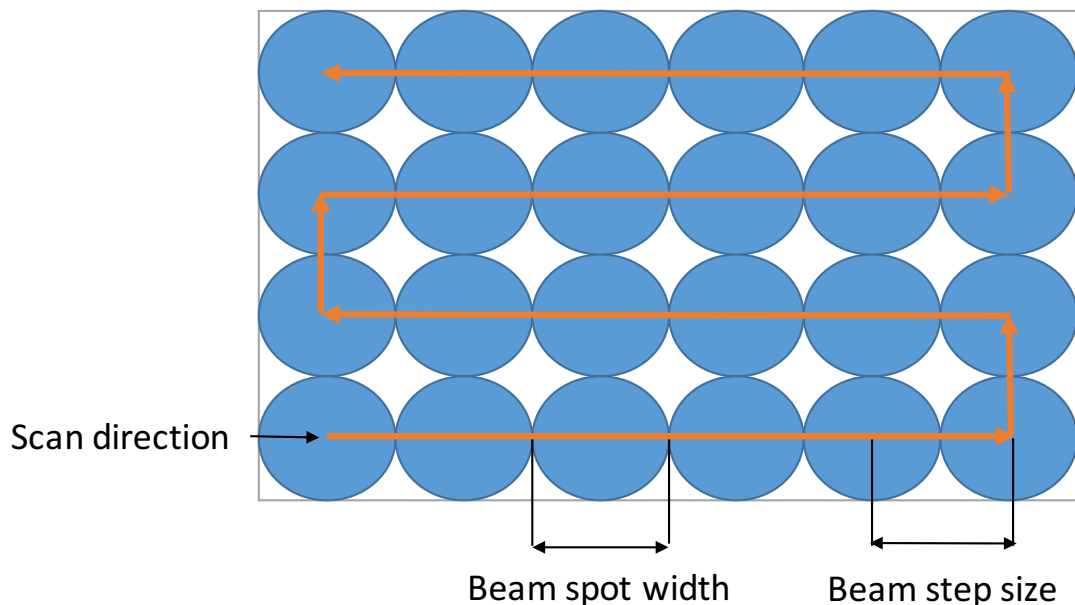


Figure 4.1.2 Diagram showing scan direction, step size and spot width during EBL execution.

With the exception of some preliminary photolithography experimentation, the devices in this study were fabricated exclusively using a Vistec VB6 EBL tool. Early process development revealed overexposure of patterns owing to substrate charging, as shown in **Figure 4.1.3a**. A 10 nm layer of Al was found to be a

sufficient charge dissipation layer to alleviate this issue. The result of this can be seen in **Figure 4.1.3b**.

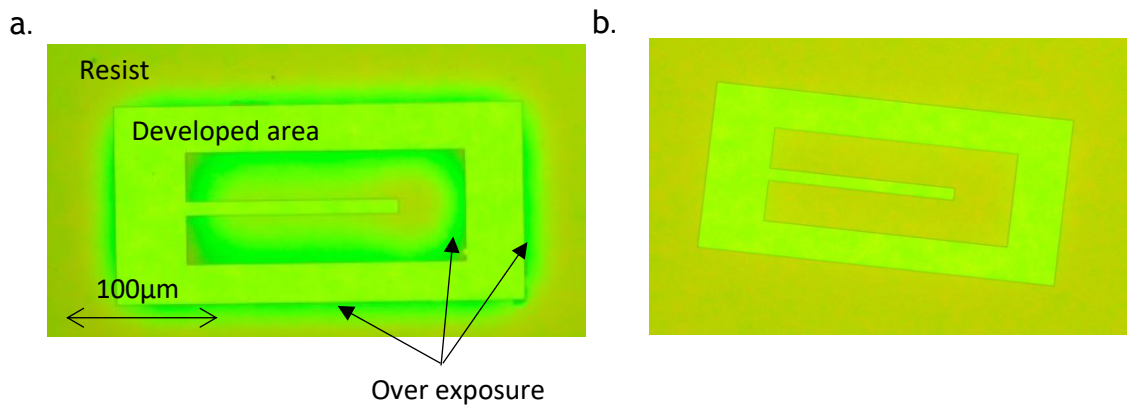


Figure 4.1.3 a & b Patterns written by EBL showing overexposure due to charge accumulation (a) and correct exposure achieved with 10 nm Al charge dissipation layer deposited on the surface of the sample post-resist deposition.

4.2 Thin Film Deposition & Lift Off

Routinely, the lithography step will be followed by a uniform thin film deposition onto the substrate which covers the exposed areas of the substrate and the remaining resist. Subsequently, the substrate can then be submerged in a solvent such as acetone to remove the remaining resist which also removes any of the thin film deposited onto it, leaving only the desired pattern overlaid by the thin film. This is a method known as lift off. To ensure a good resist profile for lift off, it is recommended that a bi-layer of resist is used so that the bottom layer undercuts the top layer. This can be achieved by using different compositions of resist. By doing this, it is also ensured that the resist removing solvent will be able to access the resist beneath the metal thin film. Typically, the lithography/lift off process will be repeated several times throughout the device fabrication process, with different overlapping layers of conducting and insulating materials deposited between each lithography step. Thus, devices of elaborate design in terms of layer count and electrical connections can be created horizontally, vertically, or a combination of both across the surface of a substrate.

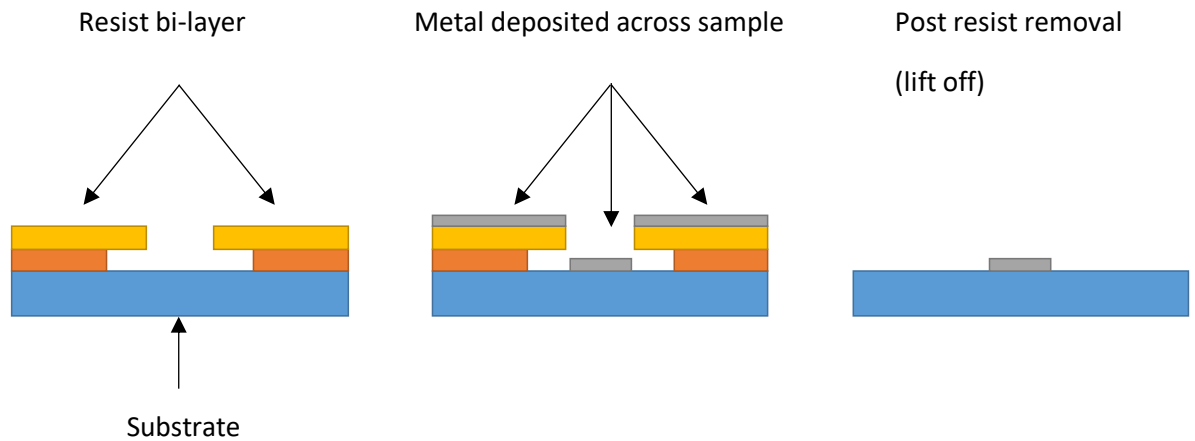


Figure 4.2.1 Diagram showing different stages of the lift off process. Metal is deposited over a bi-layer of resist. The bi-layer promotes a clean metal profile and solvent access during the final lift off stage.

There are several methods of thin film deposition commonly used including thermal evaporation, electron beam evaporation and atomic layer deposition. The main deposition technique used throughout this study is electron beam evaporation.

The evaporation tool typically has two chambers - a load lock and a main chamber, separated by a series of shutters. The substrate is loaded into the load lock where it is inverted and held above the main chamber. Inside the main chamber there are several crucibles each holding a target of metal to be potentially evaporated. Much like the EBL tool, an electron beam evaporator tool utilises a beam of electrons. The electron beam is magnetically focused onto the target metal to be evaporated. The main chamber of the system contains a quartz crystal oscillator which is used to monitor the evaporation rate of the metal. Once the evaporation rate reaches a desired threshold, the shutters open and the evaporated metal travels up through the main chamber onto the substrate. Evaporation typically occurs at a pressure of around 10^{-7} Torr which allows the evaporated metal to travel uninhibited through the chamber onto the surface of the sample.

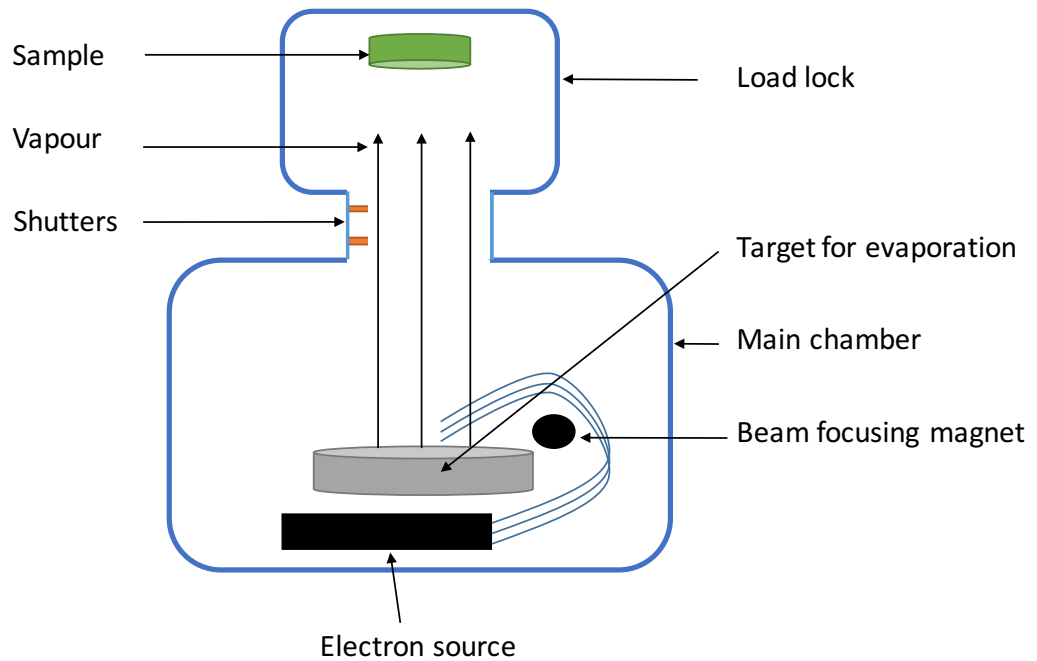


Figure 4.2.2 Diagram of electron beam evaporation tool showing critical components. The sample is held in an inverted position over the evaporated metal. A crystal oscillator (not shown) is used to measure the flow rate of the evaporated metal.

The evaporation tools used in this study were Plassys MEB 400S & 500S Electron Beam Evaporators. In addition to forming etch masks, the Plassys tools were also used to deposit electrical contacts on active devices and for transmission line measurements (TLM) (see Chapter 5).

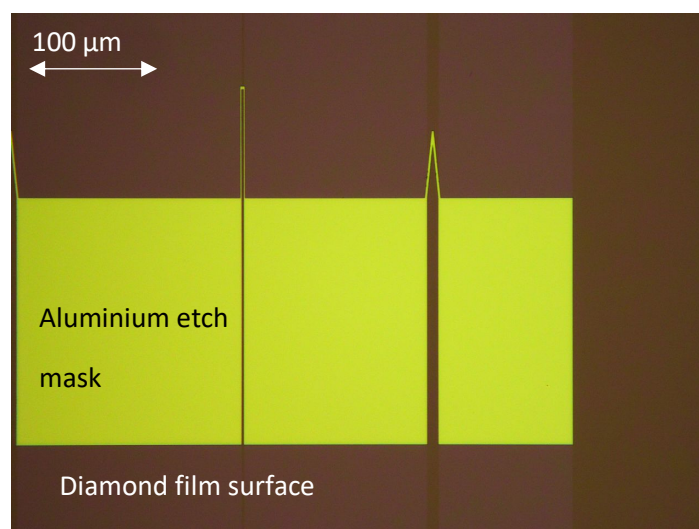


Figure 4.2.3 Optical image of an aluminum etch mask deposited by electron beam evaporation onto a diamond substrate.

4.3 Etching Processes

Perhaps one of the most challenging aspects to MEMS device fabrication is material etching. Many devices rely on the formation of nanoscale freestanding features that must be formed with absolute accuracy. In addition to operational issues, a device's mechanical behavior is much easier to predict and model if mechanical features can be accurately formed. The following sub-chapters provide details of the etching processes developed and employed by the author in order to fabricate the diamond MEMS devices presented in this work.

4.3.1 Diamond Plasma Etching

In order to create diamond MEMS devices, it is important that we have the ability to perform highly anisotropic 90° etches in the material. The most commonly known method for achieving this is by plasma etching. The plasma etching process involves placing the substrate to be etched in an appropriate gas plasma generated in an electric field. The plasma contains different types of gas species interacting with one another, experiencing different processes known as excitation, dissociation and ionization. The species interact with each other but also react with the substrate, becoming absorbed onto the surface and chemically reacting with it. The etch products are desorbed from the surface and removed from the chamber via the gas flow exhaust as demonstrated in **Figure 4.3.1**. The type of plasma etching that takes place depends on the excitation techniques used [4.4].

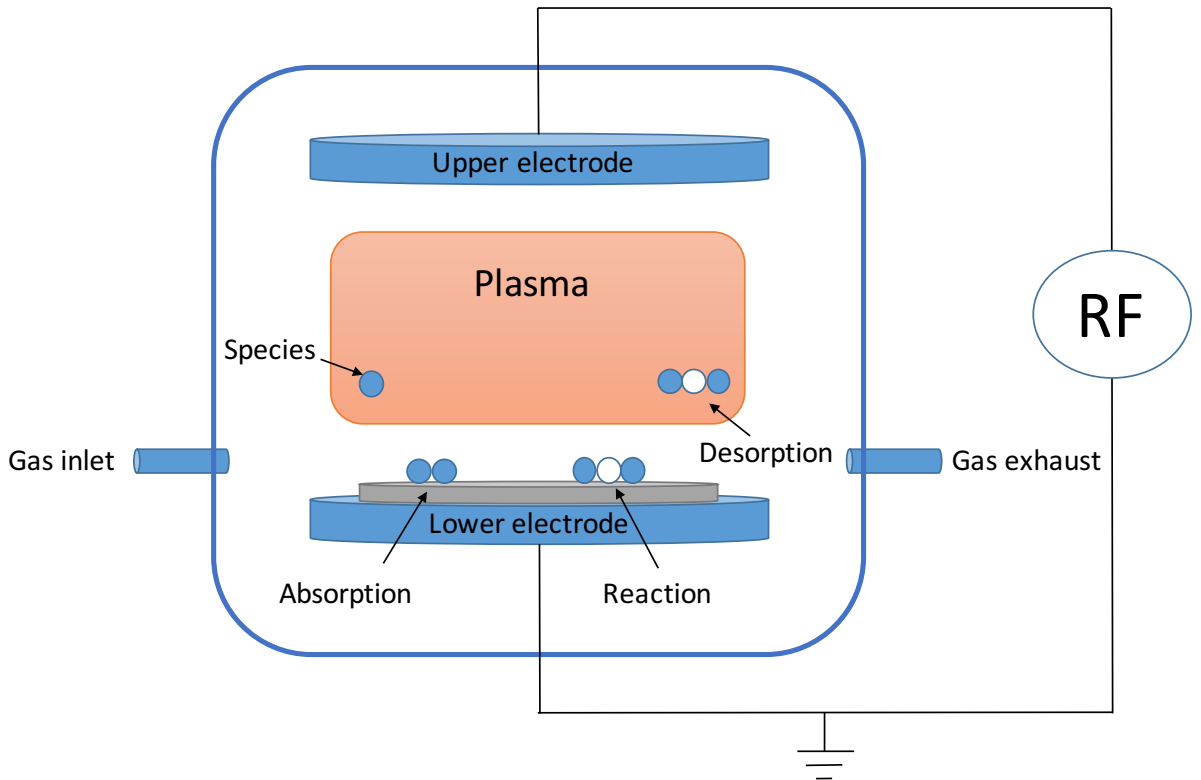


Figure 4.3.1. Non-specific radio frequency (RF) plasma etching process overview diagram showing absorption, reaction and desorption.

As diamond is chemically inert, there are not many processes that can be used to etch the material. One of the few known plasmas that will etch diamond is oxygen. Oxygen plasma species react with the diamond surface to produce the volatile etch products CO and CO₂. To achieve 90° anisotropy, a method known as reactive ion etching (RIE) is employed, which is an ion assisted plasma etching process. The addition of ion bombardment increases anisotropy by promoting the desorption of the volatile etch products. The plasma is formed in a vacuum chamber under high pressure between two electrodes. One electrode is coupled to an RF frequency (anode) and one electrode (cathode) is grounded. During the plasma forming process, the cathode generates a negative DC bias. As a result, positively charged ions are accelerated towards the cathode bombarding the substrate [4.4].

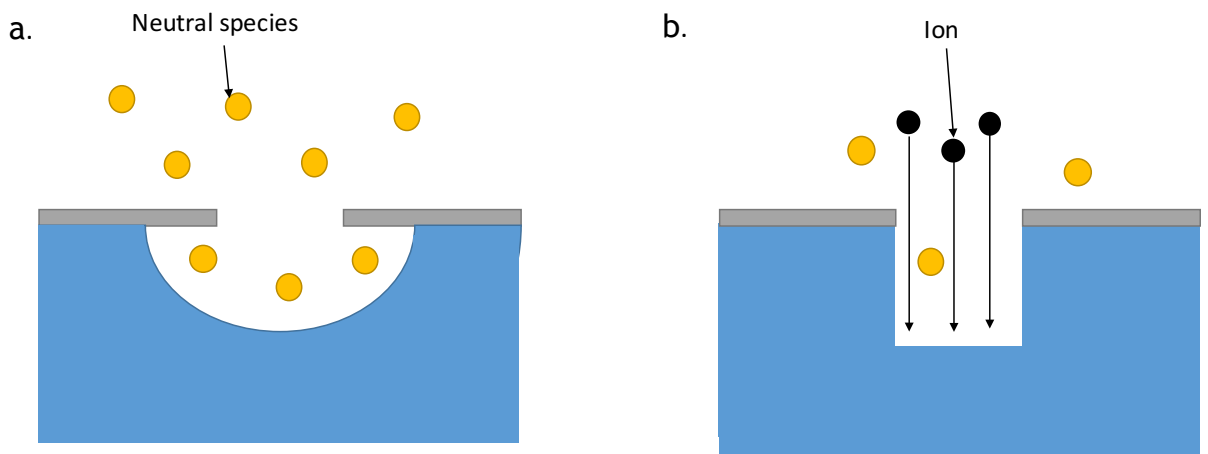


Figure 4.3.2 a & b Diagram showing isotropic chemical plasma etching (a) and anisotropic ion assisted plasma etching (b).

Figure 4.3.3 below shows an example of the anisotropy that can be achieved with RIE etching. The image shows a diamond cantilever tip (still attached to the silicon substrate), etched in an Argon/Oxygen plasma.

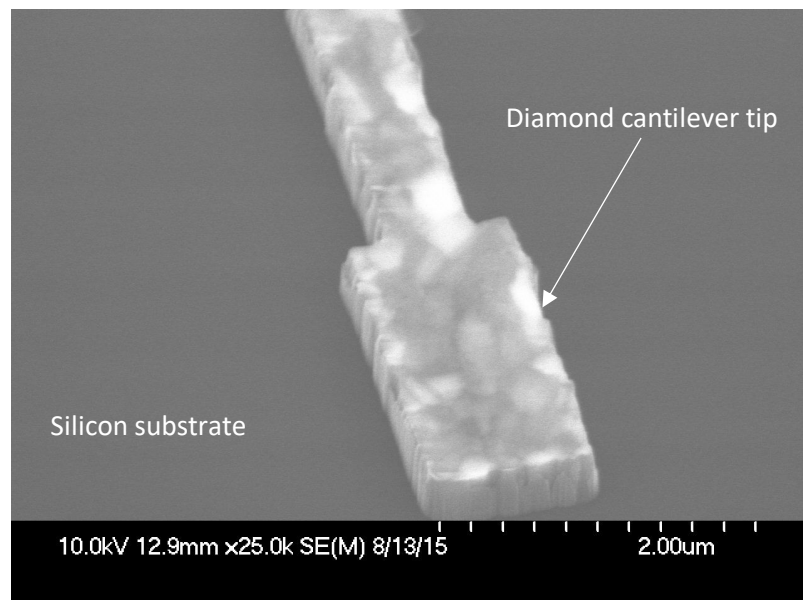


Figure 4.3.3 SEM image of a diamond cantilever tip on silicon substrate as an example of RIE etch anisotropy.

4.3.2 Silicon Plasma Etching

The most ubiquitous material in semiconductor and MEMS device manufacturing is silicon. A major advantage with this is that there is an abundance of processing techniques already developed that can be utilized by engineers. In thin film MEMS processing, it is common to have silicon as a base substrate, onto which the thin film is deposited or grown. The MEMS mechanical features are etched into the thin film then subsequent silicon etching is performed to release the free-standing mechanical parts from the substrate. The diamond thin films used for this study are all grown on silicon <100>, and as such some common silicon etching methods can be used to form the basis for the release part of the device fabrication process.

SF₆ is a common gas used in silicon plasma processing. One of the etching mechanisms for silicon in an SF₆ plasma is known to be [4.5]:



An exclusively SF₆ plasma etching process was used to release devices early in this project, and whilst devices were successfully released from the silicon substrate, the etch was found to be extremely isotropic, leaving a large device undercut. In order to increase anisotropy, and reduce undercut, a passivating polymer can be added to the process. This has a similar effect as the RIE process but involves an entirely different mechanism. When a polymer is added to the plasma it is deposited on the sidewalls of the etched silicon pit which helps control the lateral etch rate, thus reducing the undercut, as shown in **Figure 4.3.4**. In this instance C₄F₈ plasma polymer was used to good effect [4.6]. This is known as a mixed process, and can be used to achieve vertical side walls at etch depths less than 40 μm. Other etch processes such as the Bosch process exist for deeper etches [4.7], however the mixed process method provided sufficient result for the devices described herein.

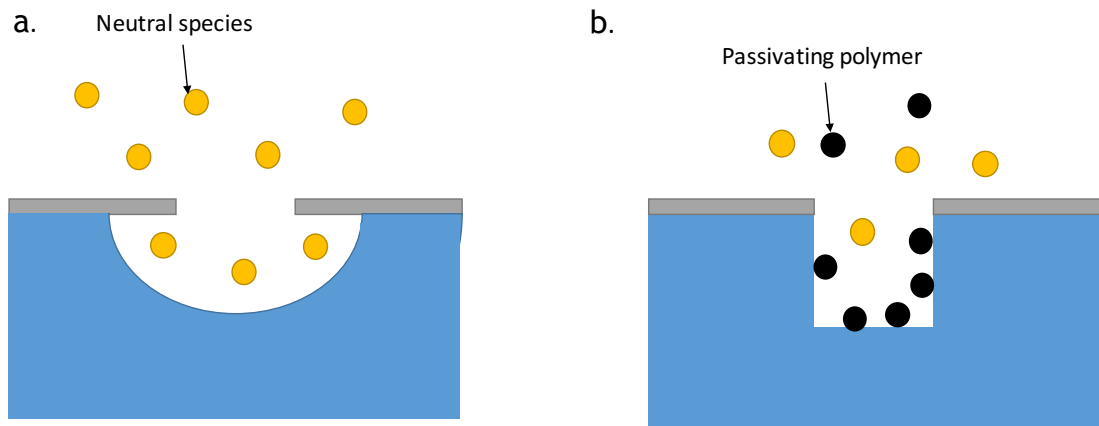


Figure 4.3.4 Diagram showing isotropic etch (a) and anisotropic etch aided by polymer sidewall passivation (b).

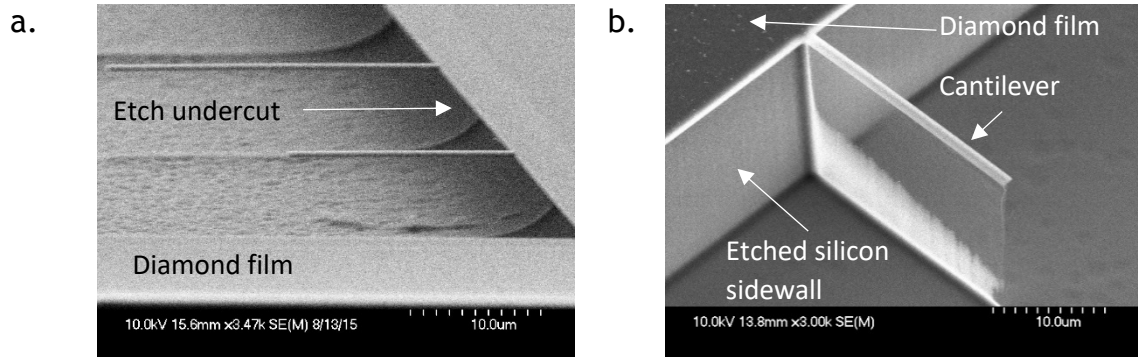


Figure 4.3.5 a & b SEM images showing the contrast between an isotropic SF_6 plasma silicon etch result (a) and SF_6 C_4F_8 mixed process etch result (b).

4.3.3 Silicon Wet Etching

In addition to plasma etching, silicon can also be etched using wet etching methods. Wet etching methods are typically less anisotropic than plasma processes, however they are less expensive and easier to implement.

A commonly used etchant in silicon MEMS processing is potassium hydroxide (KOH). The major benefit of using KOH is that it selectively etches silicon depending on its crystal orientation [4.8]. By controlling the size of the window in the etch mask, specific depths can be reached, and the etch will self-terminate when the crystal planes converge at the bottom of the etch pit. **Figure 4.3.6** shows a diagram describing the shape of a KOH etch pit in silicon $\langle 100 \rangle$. The $\langle 100 \rangle$ plane etches at a faster rate than the $\langle 111 \rangle$ plane resulting in an inverted pyramid shaped pit.

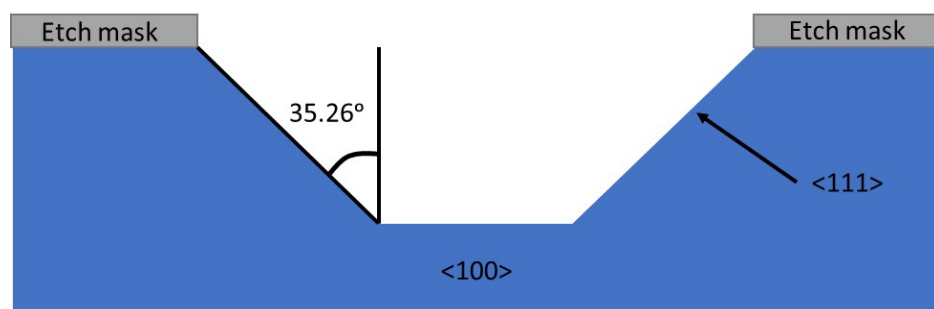


Figure 4.3.6 Diagram showing selective crystal plane etching of silicon by KOH.

KOH comes in pellet form and therefore a water solution must be created to perform an etch. The etch rate of KOH depends on the concentration and temperature of the solution. To maintain a constant concentration and temperature, an acid reflux etching kit as shown in **Figure 4.3.7** can be used.

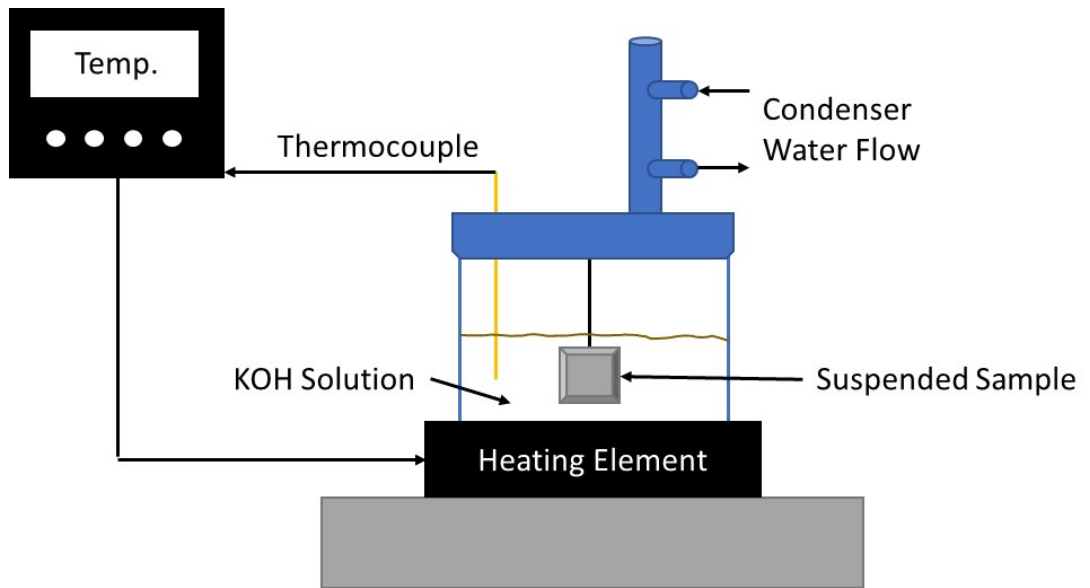


Figure 4.3.7 Typical processing equipment setup for acid reflux etching.

A heating element, thermocouple and temperature feedback control unit are used to maintain a constant temperature, and a water condenser attachment is used to maintain a constant solution concentration.

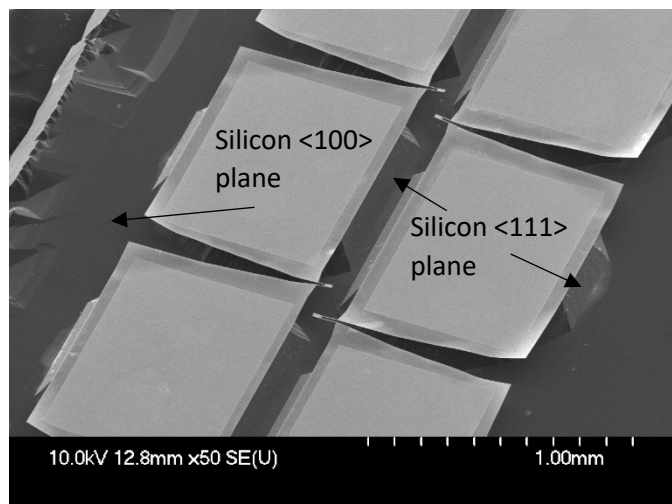


Figure 4.3.8 SEM image of diamond cantilever array released from silicon substrate by KOH wet etch showing silicon crystal planes.

One of the drawbacks of wet etching is that free standing structures are prone to becoming stuck onto the substrate if the etch depth is not sufficient. This happens at the drying stage of the process, where the surface tension of the fluid (either the etching solution, or water at a later rinsing stage) captures the free-standing element of the device, as demonstrated in **Figure 4.3.9**.

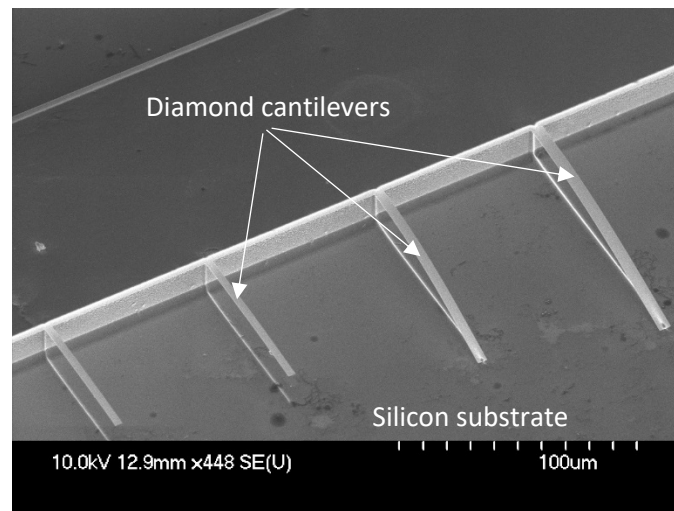


Figure 4.3.9 SEM image of diamond cantilever array partially released from silicon substrate by KOH wet etch. Note that the longer cantilevers have become stuck to the substrate surface.

4.4 Wire Bonding

The final stage of device fabrication is packaging. On a testing level, it is possible to probe different electrical elements of a device to achieve characterization. However, bond pads supplied on a device are generally fragile, and will not withstand repeated probing before becoming mechanically compromised. To overcome this, a suitably sized carrier package can be used to host the device substrate. The carrier will comprise of larger, more robust electrical contacts that the device's bond pads can be electrically attached to via microscopic wires. This process is known as wire bonding.

Two types of bond exist, wedge bonds and ball bonds. A bonding device will use a combination of vertical force, ultrasonic energy and heat to perform a bond between the wire and the contact pads. A wedge bond is performed by simply pressing the wire into the contact pad and ultrasonic energy is transferred to create a weld. The ball bonding process is different in that the tip of the bonding wire is formed into a ball before the weld is performed [4.9]. The advantage of ball bonding is that the wire protrudes vertically from the weld, so it does not matter in which direction the next bond is to be performed.

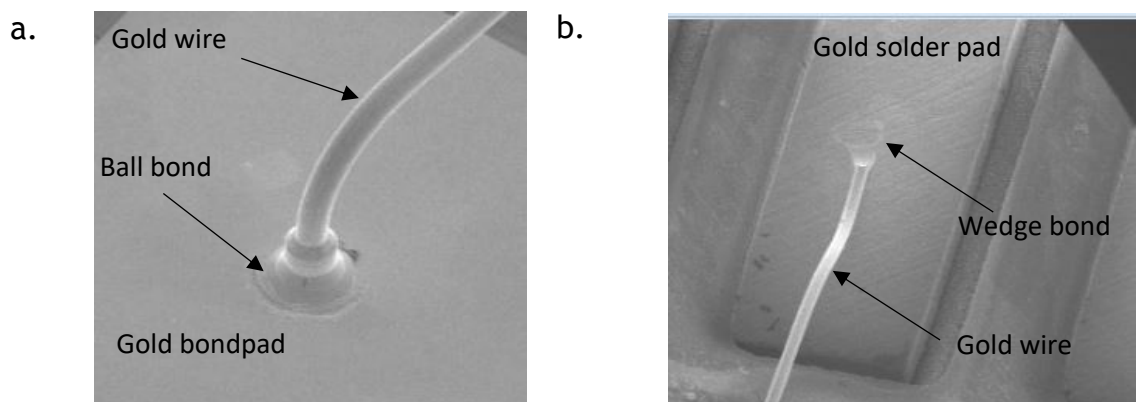


Figure 4.4.1 a & b SEM images showing ball bond (a) and wedge bond (b).

4.5 Chapter Summary

This chapter provides an overview of fabrication processes and equipment used to fabricate diamond MEMS devices. As stated previously, most of these processes originate from the semiconductor industry, however, all the processes investigated required adjusting by the author to achieve specific end results. In particular, plasma processing is notorious for inconsistent results, and required extensive process development to ensure a stable and reproducible device release process. The particular details of tools and process parameters used for fabricating specific devices is supplied in the relevant results chapters.

References

- [4.1] Okazaki, S “Resolution limits of optical lithography” *Journal of Vacuum Science & Technology B: Microelectronics and Nanometer Structures Processing, Measurement, and Phenomena* 9, 2829 (1998)
- [4.2] A. I. M. Greer and D. A. J. Moran, “Charge dissipation layer optimisation for nano-scale electron-beam lithography pattern definition on diamond,” *Diamond and Related Materials*, vol. 29, pp. 13-17 (2012)
- [4.3] Haus, J.W. “Fundamental and Applications of Nanophotonics” *Woodhead Publishing* Pages 149-184 (2016)
- [4.4] Franssila S., Sainiemi L. “Encyclopedia of Microfluidics and Nanofluidics” *Springer*, Boston, MA (2013)
- [4.5] R. Knizikevicius, R., Kopustinskasb, V.” Anisotropic etching of silicon in SF6 plasma” *Vacuum* 77 (2004) 1-4
- [4.6] Ouyang, Z., Ruzic D. N., Kiehlbauch, M.,Schrinsky A., Torek,K. “Etching mechanism of the single-step through-silicon-via dry etch using SF6/C4F8 chemistry” *Journal of Vacuum Science & Technology A* 32, 041306 (2014)
- [4.7] Lips, B., Puers, R. “Three step deep reactive ion etch for high density trench etching” *Journal of Physics: Conference Series* 757 (2016)
- [4.8] Sato, K., Shikida, M. “Characterization of orientation-dependent etching properties of single-crystal silicon: effects of KOH concentration” *Sensors and Actuators A: Physical*, Volume 64, Issue 1, Pages 87-93, 1998
- [4.9] Uno, T., Oyamada, T. “High-performance Bonding Wires for Semiconductor Packaging” *NIPPON STEEL & SUMITOMO METAL TECHNICAL REPORT* No. 117 December 2017

Chapter 5: Characterisation Equipment & Methods

The micro and nano-fabrication industry relies on sophisticated and verified methods for measuring different aspects of devices and materials in order to characterise them. As devices become smaller and more sensitive there is a requirement for characterisation tools with very high resolution in order to capture sub-femtometre displacements and sub-femtonewton forces. This chapter details the equipment used and methods employed throughout this body of work to characterise the diamond materials and MEMS devices fabricated.

5.1 Laser Doppler Vibrometry

Perhaps one of the most important tools for characterising MEMS devices is a displacement sensor. By measuring the displacement of fabricated devices, we can find a wealth of information pertaining to its operation in terms of resonance and stiffness. The tool made available for characterising the displacement of the devices in this work is the laser Doppler vibrometer (LDV). The LDV is an interferometer system that deploys a laser onto a moving surface and uses a network of beam splitters and mirrors in order to modulate a reference beam to calculate the displacement at the point of reflection.

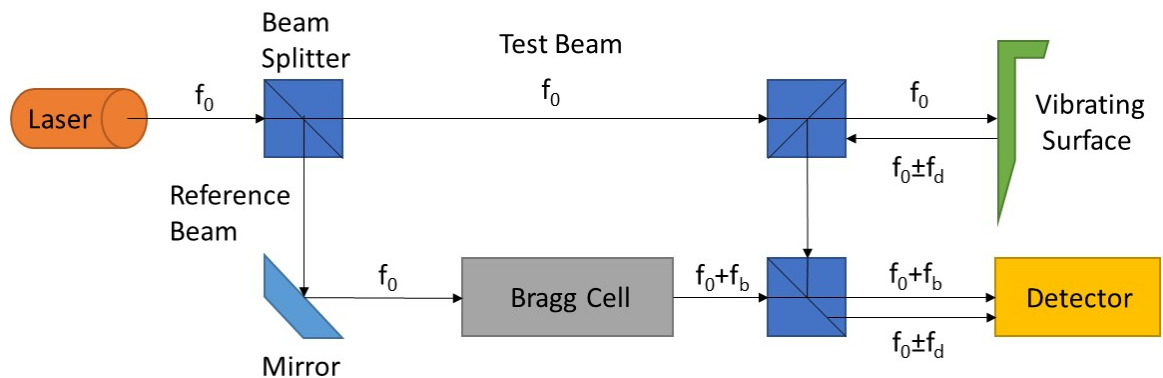


Figure 5.1.1 Schematic diagram of LDV system showing laser signal path and manipulation.

The sequence begins with a laser beam f_0 accelerated towards an initial beam splitter. The beam splitter splits the beam into a reference beam and a test beam. The test beam is focussed onto a moving surface and the wavelength of the reflected wave is modulated by the velocity of the moving surface ($f_0 \pm f_d$). The scattered modulated test beam is captured by the LDV and guided back towards a photodetector. Meanwhile, the reference beam is shifted up in frequency by means of a Bragg cell and guided towards the same photodetector. The backscattered light from the vibrating surface and the reference beam are superimposed onto the photodetector generating a phase modulated carrier signal at the photodetector output. The information pertaining to the displacement of the vibrating surface is contained in the resulting phase shift of the carrier [5.1].

The LDV system then down-converts the phase modulated carrier into the baseband.

To demodulate the signal, the carrier is converted into two quadrature signals, I (in-phase) and Q (quadrature). The two quadrature signals carry the same information as the carrier signal but are easier to manipulate computationally as they lie in the base band. In theoretical terms, the quadrature signals are sinusoidal, 90° out of phase with each other and have equivalent amplitudes [5.2].

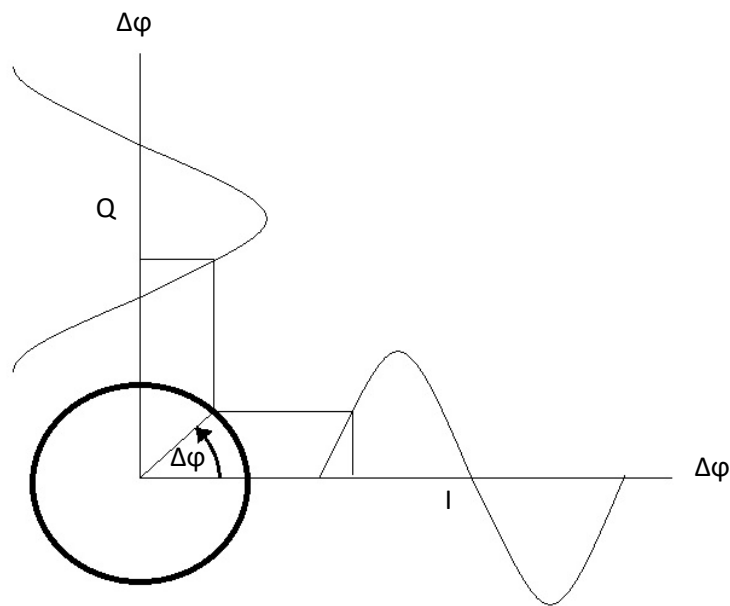


Figure 5.1.2 Diagram of quadrature signals Q & I. The phase difference between the signals is used to calculate displacement.

Figure 5.1.2 shows a graphical diagram of quadrature signals Q & I. The angle of rotation of the pointer is equal to the interferometric phase difference between the signals. The direction of rotation of the pointer corresponds to the direction of movement of the vibrating surface. The phase difference $\Delta\phi$ is calculated by the following relationships [5.2]:

$$I(\Delta\varphi) = A\sin\Delta\varphi \quad (5.5.1)$$

$$Q(\Delta\varphi) = A\cos\Delta\varphi \quad (5.5.2)$$

By dividing Equation 5.5.2 by Equation 5.5.1 we find the following relationship:

$$\frac{I(\Delta\varphi)}{Q(\Delta\varphi)} = \frac{\sin\Delta\varphi}{\cos\Delta\varphi} = \tan\Delta\varphi \quad (5.5.3)$$

And applying the inverse tan function we arrive at:

$$\Delta\varphi = \tan^{-1} \frac{Q(\Delta\varphi)}{I(\Delta\varphi)} \quad (5.5.4)$$

The phase difference $\Delta\varphi$ is proportional to the displacement of the vibrating surface Δx by the relationship:

$$\Delta\varphi = \frac{4\pi}{\lambda} \Delta x \quad (5.5.6)$$

The LDV system used to capture vibration data in this body of work is the Polytec UHF-210. With software oversampling methods the UHF-120 can be calibrated to measure vibrations up to 2.4 GHz. The UHF-120 is incredibly sensitive and able to capture sub-picometer displacements. This, however, makes the measurements highly susceptible to mechanical noise coupling, and unwanted interference is commonplace. Possible interference sources can be air conditioning systems, PC fans located near the scan head and human traffic within the lab during measurements. Therefore, extensive measures must be taken to ensure the scan head is securely clamped, and measurements be captured when the probability of lab interference is lowest. The majority of MEMS-specific manufacturers utilise specially designed low-noise laboratories for sensitive calibration and characterisation purposes.

5.2 Surface Profiling

An important aspect of device and material characterisation is surface profiling. Mechanical surface profiling generally makes use of a cantilever with an extremely hard (typically diamond) sharp tip or stylus a few nm wide which probes the surface of the sample. By using electronic feedback and detection methods, the displacement of the tip or needle as it moves across the sample surface can be used to build an image of the sample's topography. One of the most common forms and a technique used widely in this work is atomic force microscopy (AFM).

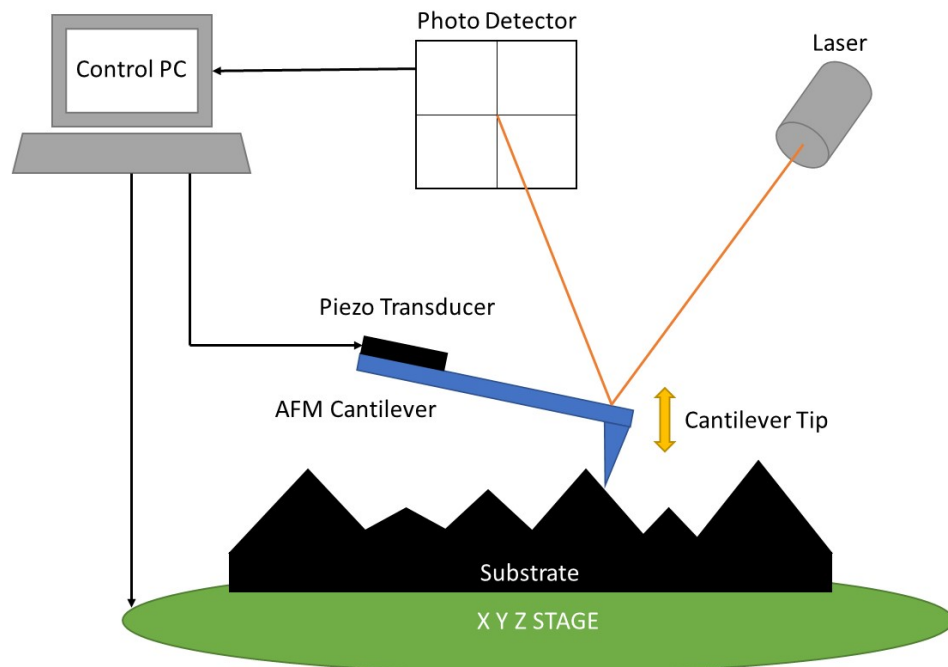


Figure 5.2.1 Graphical representation of AFM system. The photodetector captures the laser reflected from the cantilever tip as it probes the sample surface.

The AFM method uses a silicon cantilever with an elongated pointed tip to profile the surface of samples. An AFM system uses the laser bounce method to determine cantilever displacement. A laser is focussed onto the free end of the cantilever beam where it is reflected onto a photodetector. As the cantilever moves, the laser beam is scattered onto the photodetector quadrants. The AFM system then takes the photodetector voltage change and determines the cantilever's displacement. There are two common modes of operation for an AFM tool, static mode and dynamic, or tapping mode. In static mode, the cantilever tip is accelerated towards the sample surface and the deflection of the cantilever in combination with its stiffness constant (usually supplied by the manufacturer) can be used to determine mechanical properties of the sample. In tapping mode, the cantilever is driven into a vibrating motion by a piezoelectric transducer. As the tip moves across the sample, the amplitude and frequency of the resonant motion modulates depending on sample surface conditions. The AFM uses the change in motion of the tip to build the image of the sample surface. This method can be very useful in determining sample surface roughness and is used in this work to characterise sample roughness after etching. However, the resolution of the AFM scan is limited by the geometry of the cantilever tip. The cantilever tip is conical, so if the sample, or feature, to be characterised has smaller attributes than the width or angle of the tip then an inaccurate image will be resolved [5.3].

In instances where surface roughness is not of concern and only the height difference between two adjacent parts of a sample is required, a less sophisticated form or surface profiling is satisfactory. In these instances, a 2D contact profilometer can be used. Similar to the AFM, the profilometer uses a stylus to make contact with the sample surface, and then moves a pre-specified distance in one direction. The stylus provides feedback on its position, typically through a piezoresistive mechanism, which the system then translates into Z deflection distance. This method is less accurate than AFM, however it has been used in this work to provide a fast and less complex method of characterising etch rate and sample height (see **Chapter 6**) [5.3].

5.3 Transmission Line Measurements

Transmission line measurement or transfer length measurement (TLM) is a method used in semiconductor device characterisation to determine information pertaining to metal contact and semiconductor material properties [5.4]. By performing TLM analysis it is possible to find the contact resistance between any given contact and semiconductor interface, the sheet resistance of the semiconductor and the theoretical transfer length of the contact. The method utilises a series of geometrically identical contacts on a semiconductor surface (commonly defined using metallisation and lithography techniques) spaced increasingly further apart from one another. Typically, the contacts are linearly spaced as can be seen in the example below in **Figure 5.3.1**, where the gap increase by the primary gap width every instance.

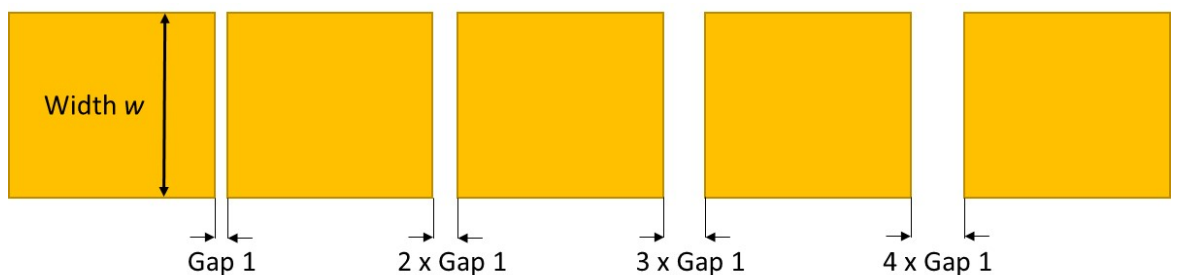


Figure 5.3.1 Graphical representation of TLM structures showing gap size and width.

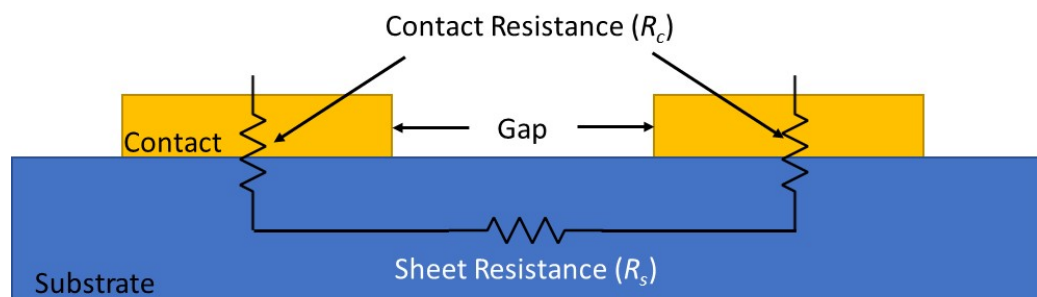


Figure 5.3.2 Schematic model of TLM equivalent circuit showing sheet and contact resistance.

As can be seen from **Figure 5.3.2** above, each pair of TLM contacts can be modelled as a network of three resistances in series: the resistances between each contact and the substrate, and the sheet resistance of the semiconductor. By applying a voltage across each pair of contacts in turn and measuring the resistance between each pair, we can build up a plot of resistance vs gap size that can be used to determine the contact and sheet resistance of the network.

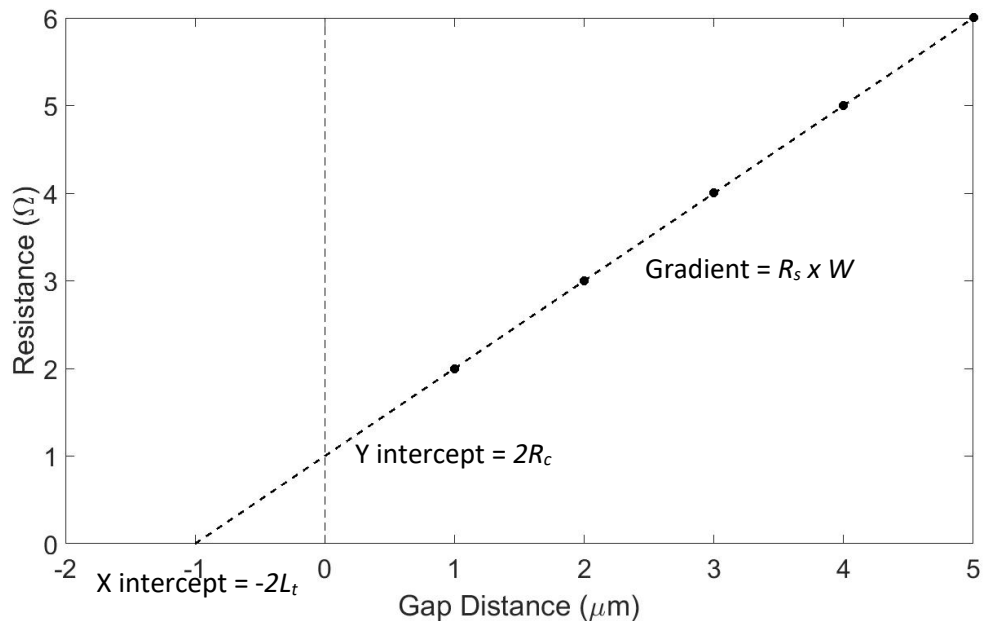


Figure 5.3.3 Idealised TLM plot showing linear fit to TLM gap resistances.

Figure 5.3.3 shows an idealised plot of TLM resistance vs gap data for five different gap distances ranging from 1-5 μm . Realistically the measured resistances would not all lie exactly on a straight linear fit, and average values over a range of measured TLM structures would be used. From the gradient of the slope we find the sheet resistance of the semiconductor material divided by the width of the TLM. To normalise this figure into useable data we multiply by the TLM width shown in **Figure 5.3.1** which reveals the sheet resistance of the material in Ω/\square . We can then multiply this figure by the thickness of the sample material to find its resistivity. The Y intercept of the linearly extrapolated fit to the resistance data gives the combined contact resistance for both contacts, $2R_c$. If we extrapolate further to find the X intercept this give us the theoretical combined transfer length of the contacts, $2L_t$. The transfer length refers to the

area of the contact where the charge transfer from the contact to the semiconductor takes place. That is, the charge transfer is not distributed evenly across the contact owing to current crowding at the edges in the direction of flow. This method of determining transfer length remains valid only if the sheet resistance of the semiconductor material is assumed to remain constant beneath the contact. In some instances, where contact annealing has taken place, the sheet resistance cannot be assumed to be the same under the contacts as it is between the contacts. If the transfer length is to be used, the contribution of the contacts can be expressed as contact resistivity $\rho_c \Omega/cm^2$ using the effective area of the contact. If the transfer length is deemed inconclusive by an unknown sheet resistance below the contact then the contact resistance can be normalised by the contact width and expressed in terms of Ω/mm .

TLM structures designed and used in the work are $150 \mu m^2$ and the gaps between contacts designed as 1, 2, 3, 4 and $5 \mu m$. However, owing to the nature of the lithography and lift off methods used to fabricate the contacts, optical or SEM inspection must be used to determine that actual width of the gaps as shown in **Figure 5.3.4.**, as this value can vary.

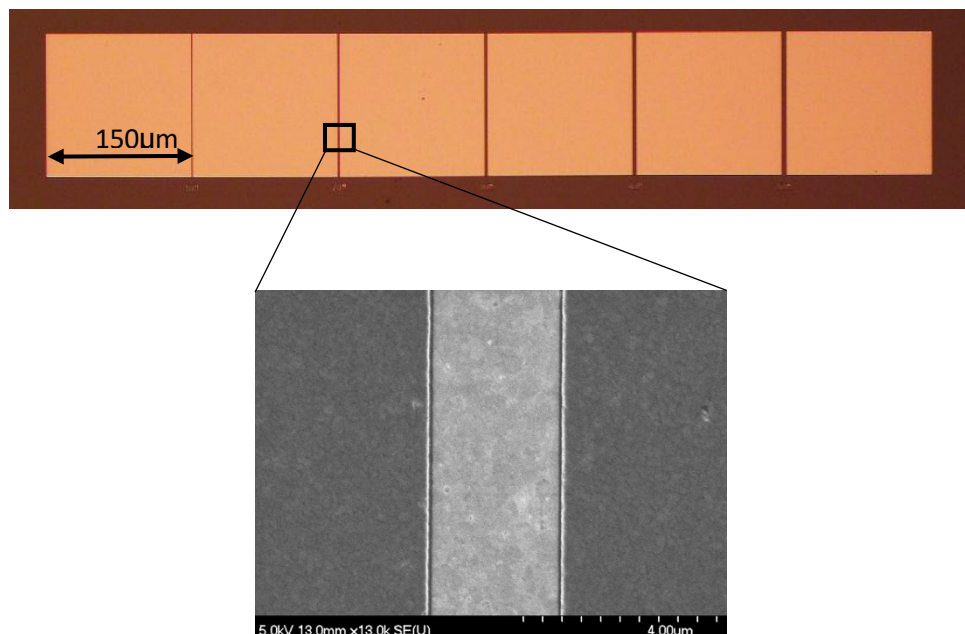


Figure 5.3.4 Optical & SEM inspection of TLM structure to determine gap width. Actual measured distance of $2 \mu m$ gap is $1.7 \mu m$.

5.4 Scanning Electron Microscopy

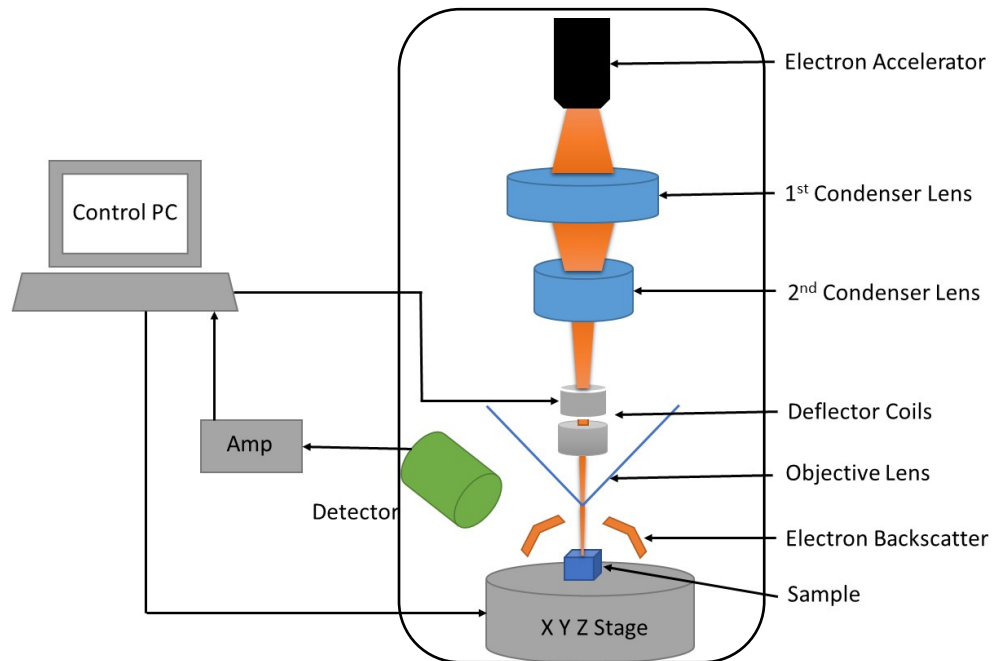
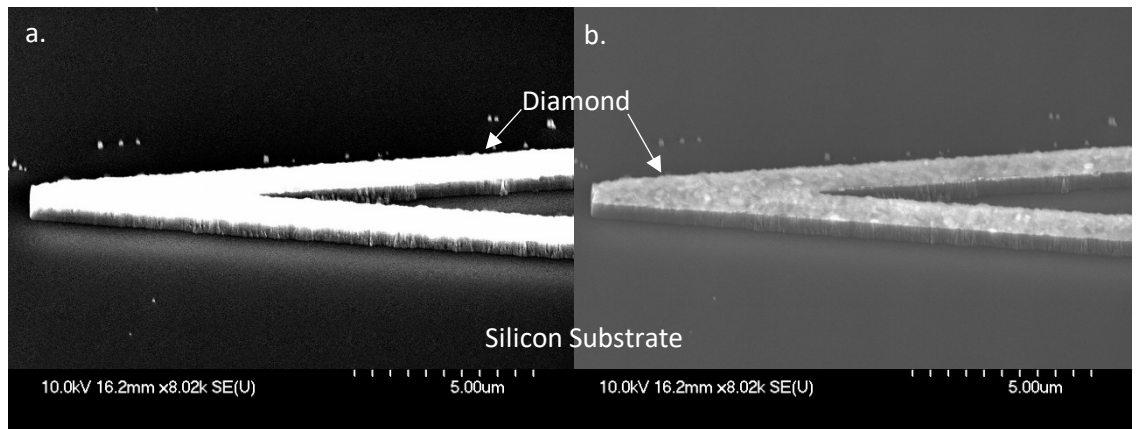


Figure 5.4.1 Graphical representation of SEM system.

Owing to the limits of optical detection, conventional optical microscope systems provide insufficient magnification to visualise most MEMS and NEMS devices at a useful level. In this body of work, to achieve visualisation of micro and nano-scale devices, a scanning electron microscope (SEM) system is deployed [5.5]. The SEM system is a type of electron microscope that scans a sample with a focused beam of electrons to generate images of it. Optical imaging resolution is limited by the wavelength of the illuminating light, whereas SEM imaging can theoretically resolve sub nm features depending on the system. The system (**Figure 5.4.1**) consists of an electron source from which an electron beam is accelerated through a series of condenser lenses used to focus the electron beam. Once the beam has been focused, magnetic deflector coils are used to manipulate the direction of the beam through a final objective lens via PC control. The electron beam is incident on the sample, causing the electrons to be scattered into the chamber. A portion of the beam will penetrate the sample, dependent on the sample material properties, topography and beam energy. These interactions create different signals, which are then captured by one or more detectors in the chamber and amplified *en route* to a PC control unit where the image is formed.

The different signals can include backscattered electrons, secondary electrons and X-Ray.



Figures 5.4.2 a & b SEM images of etched PCD cantilever tip on silicon substrate showing the irregular contrasting effects of sample charging (a) and typical image contrasting (b).

An issue that can arise when capturing SEM images is the phenomena of charging. Insulating samples are subject to a build-up of electrons and their subsequent uncontrolled discharge. This can produce artefacts in the captured image such as warping and irregular contrasting which can be seen in **Figure 5.4.2 a**, where the grain detail on the surface of the diamond film has become undetectable over time. Two methods employed that can help alleviate the symptoms of charging are: reducing the energy of the electron beam by decreasing the beam current or beam voltage, or a common practice used is to coat the sample in a conductive layer which provides the electrons with a path such that they do not become embedded in the insulating sample.

The SEM images displayed in this body of work were captured using a Hitachi SEM4700. Optimal settings for capturing intrinsic diamond sample images are: backscatter signal from a 10 kV, 5 μ A beam, and optimal settings for capturing boron doped PCD sample images are: backscatter signal from a 5 kV, 5 μ A beam.

5.5 Chapter Summary

Within this chapter is a description of state-of-the-art tools used in this work to characterise fabrication processes and diamond MEMS devices reported. This list, although not exhaustive, is a good representation of systems and techniques currently employed in the MEMS industry at time of writing. The drive to make devices smaller, faster, more sensitive inevitably leads to increasing demands from characterisation equipment and consequently these tools will be adapted and replaced as necessary.

References

- [5.1] S.J.Rothberga, M.S.Allen, P.Castellini, D.Di Maiod, J.J.J.Dirck, D.J.Ewins B.J.Halkona, P.Muyshondte, N.Paonec, T.Ryang, H.Steger, E.P.Tomasinic, S.Vanlanduiti, J.F.Vignola, “An international review of laser Doppler vibrometry: Making light work of vibration measurement” *Optics and Lasers in Engineering* Volume 99, December 2017, Pages 11-22
- [5.2] *Polytec Scanning Vibrometer Theory Manual V. 9.1*, Waldbronn DE
- [5.3] R. K. Leach, “Good Practice Guide No. 37: The Measurement of Surface Texture using Stylus Instruments”, *National Physical Laboratory Publications* (UK), (2016)
- [5.4] G. K. Reeves, H. B. Harrison, “Obtaining the specific contact resistance from transmission line model measurements”, *IEEE Electron Device Letters*, 3, (1982)
- [5.5] L. Reimer “Scanning Electron Microscopy” Springer (1998)

Chapter 6: Fabrication Results

The next chapter focuses on the author's efforts to fabricate diamond MEMS utilising the processes and methods described in the previous two chapters. As will be explained further, the fabrication and characterisation of two distinct devices is discussed: a passive micro-cantilever micro-rheometer made from intrinsic PCD (6.1), and a micro-cantilever based piezoresistive sensor made from boron-doped PCD (6.2 - 6.3). Material characterisation, fabrication methods & process development are discussed and contextualised.

6.1 Fabrication Results: Intrinsic PCD Micro-cantilever

As has been expressed throughout this work, passive micro-rheology is an attractive method for evaluating the mechanical properties of fluids in a fast, effective and low cost way using a minimal sample size. Owing to their simplicity and availability, active MEMS micro-cantilevers have been applied in this field to some success using established models, but reported methods lack in terms of high frequency analysis and are limited to measurements at the device's excitation frequency. Therefore, an investigation into a MEMS micro-cantilever device for passive micro-rheology by applying optical tweezers modelling methods whilst exploiting the material properties of diamond is explored.

The first step to realising such devices was to investigate fabrication methods with the aim of fabricating arrays of free standing micro-cantilevers from polycrystalline diamond (PCD).

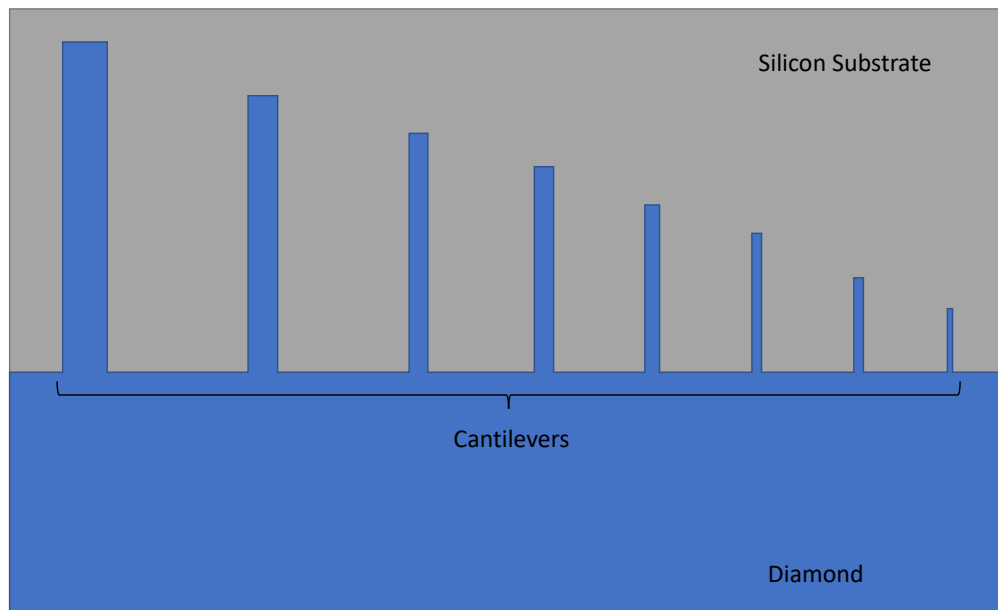


Figure 6.1.1 Graphical representation of initial micro-cantilever array design. Not drawn to scale. Each cantilever varies in length and width to the next, ranging from 1 μm to 4 μm in width, and 10 μm to 100 μm in length. The height of the cantilever is constant and corresponds to the thickness of the diamond layer.

Two-inch PCD-on-silicon samples grown by microwave plasma chemical vapour deposition (MPCVD) and chemically-mechanically polished (CMP) were supplied by collaborator Dr Oliver Williams at Cardiff University. Further details of deposition

and CMP conditions can be found in previous work: [6.1] [6.2]. The two-inch wafers are cleaved into 10 mm x 10 mm samples for ease of handling. The initial step to realising PCD devices was to investigate PCD plasma etching. SEM imaging of the cleaved edges showed the thickness of the sample to be around 500 nm, as shown in **Figure 6.1.2**. An oxygen/argon gas mixture in a reactive ion etching system is commonly used to achieve vertical sidewall etching in diamond and thus forms the basis for the investigated process [6.3], [6.4]. The PCD samples were patterned with micro-cantilever arrays using electron beam lithography. Aluminium was then metallised onto the PCD as an etch mask for the diamond etching process. Aluminium was chosen as it is reported to have a high selectivity versus diamond in the etching process [6.4]. The cantilever features were etched into the diamond using an oxygen/argon plasma in an O.I. System 100 reactive ion etching (RIE) tool. Starting parameters were taken from processes developed previously within the research group.

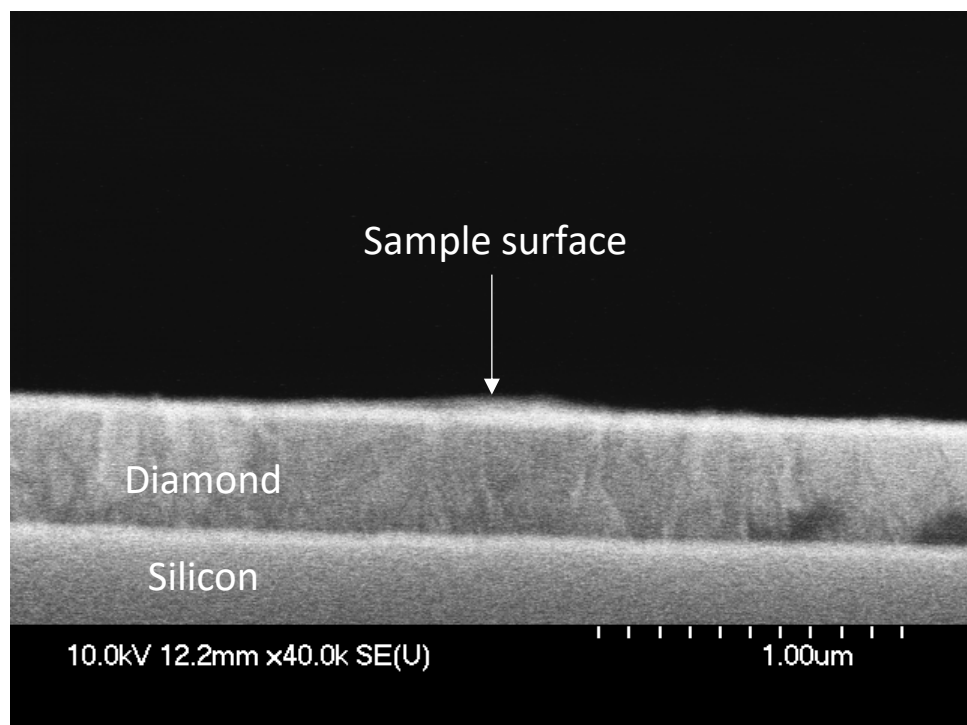


Figure 6.1.2 SEM image of the cleaved edge of diamond sample.

Gases	Flow rate & ratio (sccm)	Temp. (°C)	Power (Watts)	Pressure (mTorr)	Etch Rate (nm/min)
O ₂ /Ar	40/10	22	200	20	22±2

Table 6.1.1 Process parameters for diamond etching in RIE tool. The etch rate error corresponds to the surface roughness of the material.

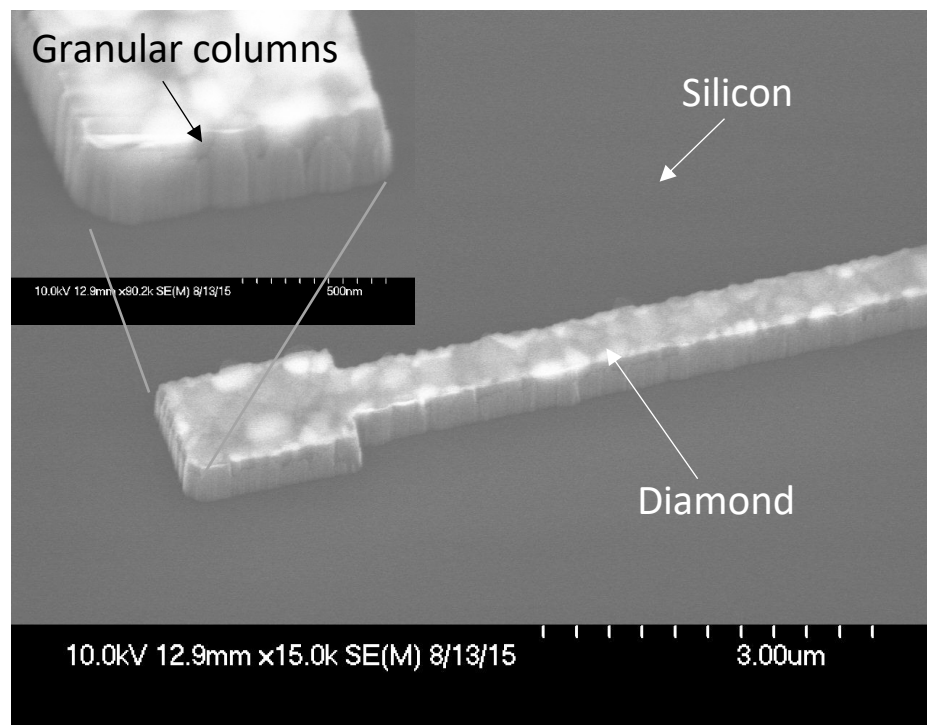


Figure 6.1.3 SEM image of diamond-on-silicon cantilever structure post RIE diamond etching. Close up of cantilever tip showing diamond granular columns (inset) (rotated 90° counter-clockwise from main image).

The results of the PCD RIE process can be seen in **Figure 6.1.3**. The process parameters shown in **Table 6.1.1** yields highly anisotropic diamond structures. By measuring the height of the structures before and after etch mask removal we found the selectivity of diamond to aluminium to be ~100/1. O₂/Ar is a common gas combination for etching diamond, and work reported elsewhere study various etch rates for these gasses between 10 - 60 nm/min [6.5]. The relatively low etch rate reported herein could be attributed to the plasma power or gas flow rate, with increased power or flow increasing the etch rate [6.6]. Oxygen may be used alone and is more commonly used for surface etching as it leaves a smoother

surface, however, this reduces the etch rate. Additional mechanical bombardment from the larger argon ions simultaneously increases the etch rate but leaves the etched areas rougher [6.7].

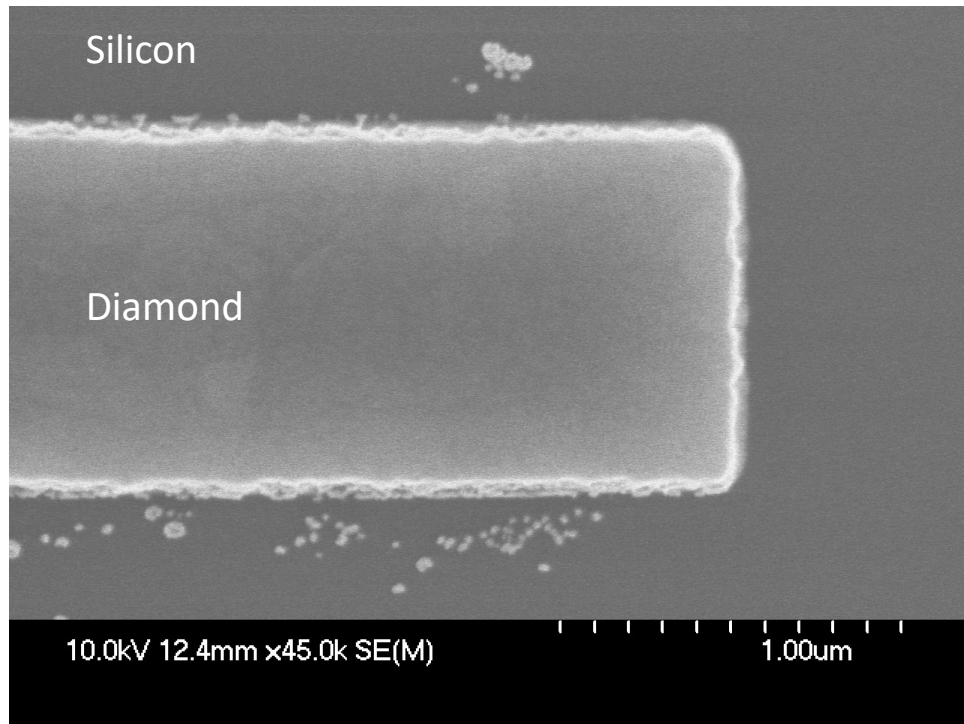


Figure 6.1.4 SEM image from directly above cantilever post RIE etching in oxygen/argon plasma showing sidewall roughness (pre mask removal).

Figure 6.1.4 shows the sidewall roughness of the etched diamond features. Roughness is estimated from SEM imaging to be around ± 20 nm. Sidewall wall roughness could be attributed to two things: either the aluminium etch mask becomes rougher during the etch process and this roughness translates onto the diamond features, or the grain boundaries in the diamond are being selectively etched. The granular columns are visible in the SEM of the etched diamond features and can be seen in **Figure 6.1.3**.

By far the most challenging aspect of producing free standing cantilever type structures is the release step of the process where the cantilever structure is released from its host substrate. One of the benefits of fabricating diamond devices is that diamond is highly chemically inert: one of the few and most common ways to etch diamond is by oxygen plasma, therefore it can be subjected to many silicon etching processes without the need for any other etch mask than the diamond itself. For ease of use, a top-side dry etching method was employed to release the diamond cantilevers from the silicon substrate. The first method described uses a sulphur hexafluoride (SF₆) plasma exclusively to isotropically etch any silicon not masked by the diamond cantilever structures. This yields a ratio of around 3:1 vertical to horizontal etch rate. This severely limits the etch depth that can be achieved without creating a significant undercut at the base of the cantilevers. A large undercut increases the effective length of the cantilever, lowering the resonant frequency and Q factor of the device such that their operation deviates significantly from classical cantilever beam theory. The process parameters shown in **Table 6.1.2** below yield an etch rate of 9 μm/min. This is higher than similar processes reported elsewhere that yield around 5 μm/min [6.8]. It has been reported that a chamber pressure of 1-6 mTorr can lead to anisotropic silicon etching, however, this reduces the etch rate to around 0.1-0.5 μm/min which is only suitable for shallow etching [6.9].

Gases	Flow rate (sccm)	Temp. (°C)	Power (W)	Substrate power (W)	Pressure (mTorr)	Vertical Etch Rate (μm/min)
SF ₆	300	20	1800	20	46	9±2

Table 6.1.2 Process parameters for silicon etching in ICP tool.

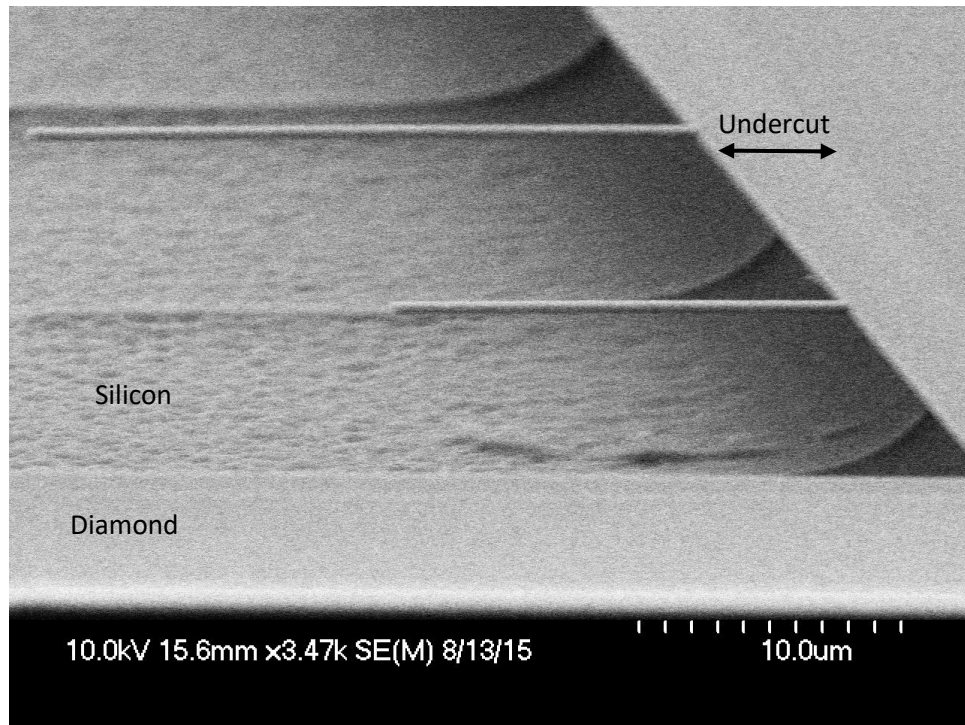


Figure 6.1.5 SEM image of cantilever array released from silicon substrate by isotropic top-side ICP etching.

In an attempt to minimise the undercut of the devices and maximise the etch depth, the release process was moved to a mixed-process whereby a passivating polymer, octafluorocyclobutane (C_4F_8), is introduced during the etching process to control the isotropy of the process and hence the undercut rate.

Gases	Flow rate (sccm)	Temp. ($^{\circ}C$)	Power (W)	Substrate power (W)	Pressure (mTorr)	Vertical Etch Rate ($\mu m/min$)
SF_6/C_4F_8	40/50	20	600	12	10	1 ± 0.2

Table 6.1.3 Process parameters for silicon mixed process etch in ICP tool.

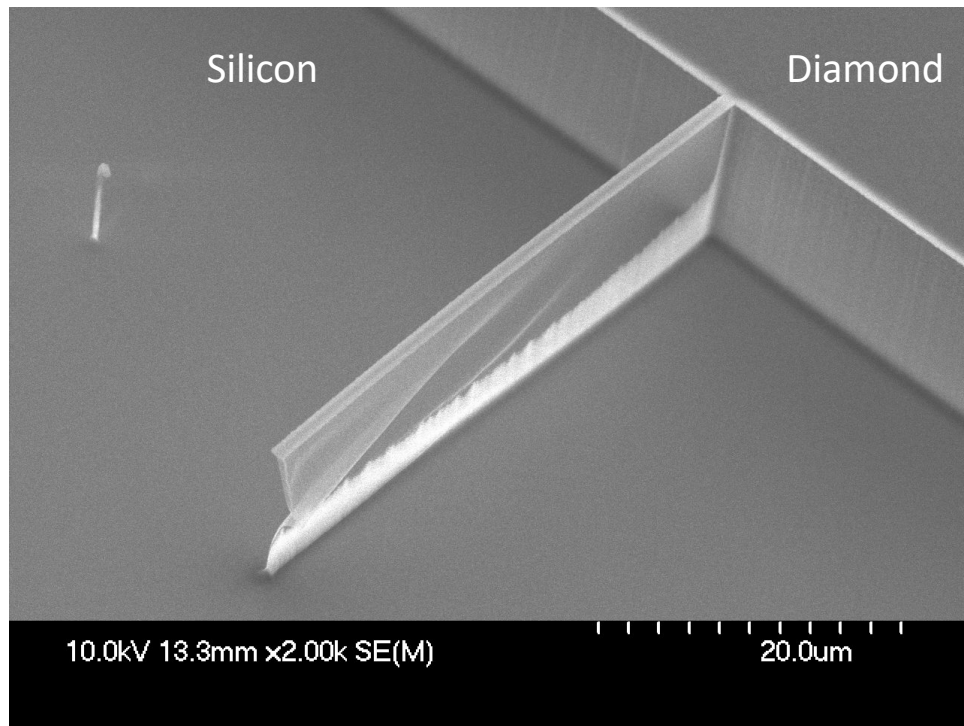


Figure 6.1.6 SEM image of a 1 μm x 40 μm x 0.48 μm cantilever beam post mixed process silicon etch.

Figure 6.1.6 shows an SEM image of a 1 μm x 40 μm x 0.48 μm cantilever beam post mixed process silicon etch. **Table 6.1.3** displays the process parameters used to achieve the results shown in **Figure 6.1.6**. The etch rate of 1 $\mu\text{m}/\text{min}$ is in accordance with similar processes reported elsewhere and the etch has achieved 90° anisotropy [6.10]. Although the undercut at the base of the cantilever is minimal, the etch process has failed to completely remove the silicon from beneath the cantilever. Further attempts to remove the remaining silicon involved a further dry etch stage again using SF_6 exclusively. This removed some of the silicon but further increased the undercut at the base of the cantilever as can be seen in **Figure 6.1.7** below. Increasing the SF_6 flow or decreasing the C_4F_8 flow during the etch process only served to further increase the undercut.

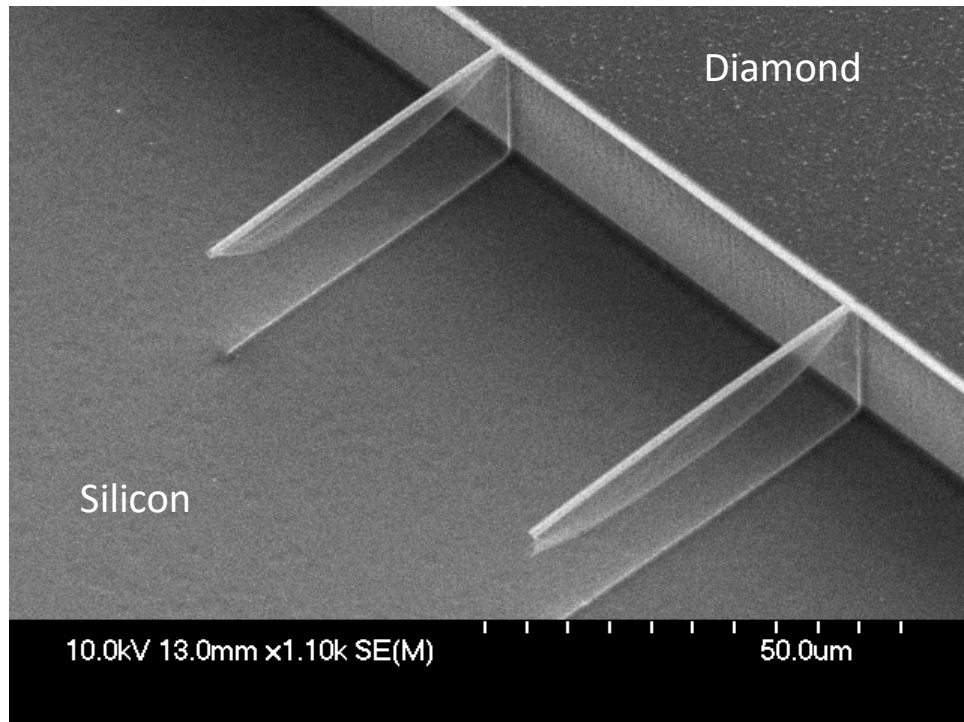


Figure 6.1.7 SEM image of a $1\ \mu\text{m} \times 40\ \mu\text{m} \times 0.48\ \mu\text{m}$ cantilever beam post mixed process silicon etch and further SF_6 etch to remove silicon from under the cantilever.

In an attempt to remove the excess silicon from under the cantilever post mixed process silicon etch, wet etching alternatives were investigated. Potassium hydroxide (KOH) is a silicon wet etchant used for MEMS processing that selectively etches silicon depending on its crystal orientation, and has been used for AFM cantilever fabrication [6.11]. During a purely KOH release process, an acid reflux etching kit would be used to maintain a constant temperature and KOH concentration. A full KOH release process would be unsuitable for releasing structures with such relatively small feature sizes as it is an aggressive etchant and can leave a large undercut. However, by using a small batch of etchant in a beaker at a relatively low temperature and short etch duration, KOH was expected to be suitable for removing the excess silicon from under the partially released cantilevers.

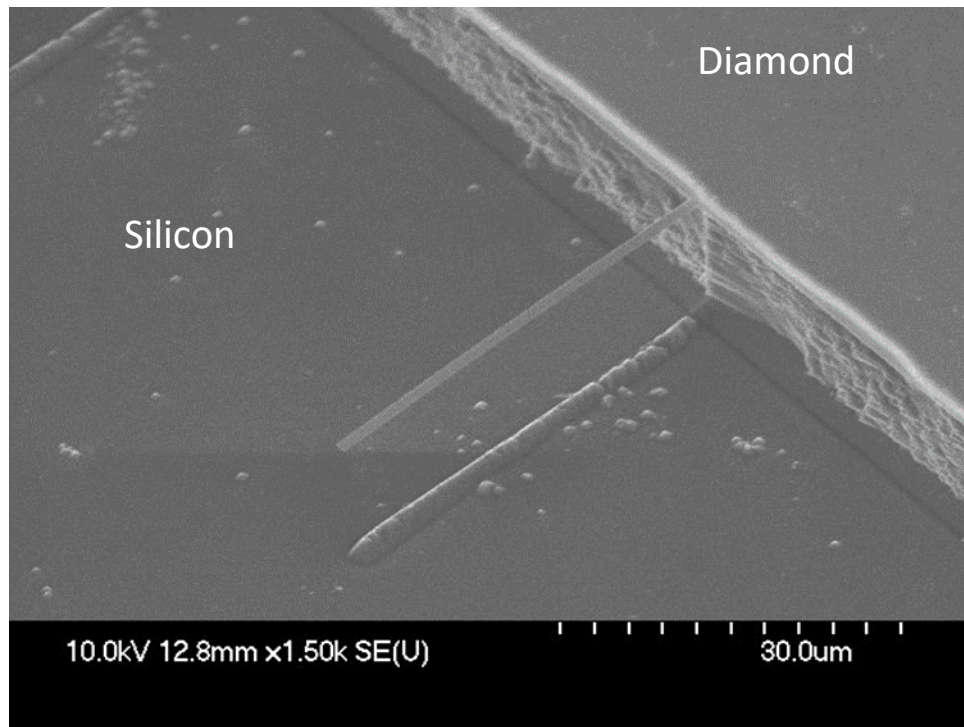


Figure 6.1.8 SEM image of a $1\ \mu\text{m} \times 40\ \mu\text{m} \times 0.48\ \mu\text{m}$ cantilever beam post mixed process silicon etch and further KOH wet etch to remove silicon from under the cantilever.

Figure 6.1.8 shows an SEM image of a $1\ \mu\text{m} \times 40\ \mu\text{m} \times 0.48\ \mu\text{m}$ cantilever beam post mixed process silicon etch and further KOH wet etch to remove silicon from under the cantilever. KOH needs a raised temperature to etch silicon at a sufficient rate, however, KOH reacts exothermically when mixed into water to form a solution. The heat generated at room temperature from creating a 30 % KOH solution was sufficient enough to remove all the excess silicon from the partially released cantilevers with no significant undercut within 5 minutes.

6.2 Fabrication Results: Piezoresistive Micro-Cantilevers from Boron Doped PCD - Material Characterisation

Piezo-resistive micro-cantilevers are common devices that have been applied in many areas of technology including but not limited to AFM, chemical and biological detection [6.12]. Owing to the large piezoresistive effect in doped silicon and well-established manufacturing processes, the majority of piezoresistive devices are silicon based. Over the past decade or so, advancements in chemical vapour deposition technology have promoted polycrystalline diamond as an attractive alternative to silicon-based devices. With regards to its excellent mechanical properties, polycrystalline diamond exceeds silicon in many aspects in terms of biocompatibility and robustness [6.13]. The electrical properties of boron-doped polycrystalline diamond have been shown to be less temperature dependant than other semiconductors in addition to its relatively high piezoresistive effect [6.14]. Recently, there has been an increase in demand for low cost, low power medical diagnostic devices for use at point of care (POC) [6.15]. MEMS devices have the potential to provide a solution to this demand, and polycrystalline diamond exhibits excellent mechanical properties and biocompatibility for such devices. In the following sub-chapters the fabrication of boron-doped polycrystalline diamond piezoresistive cantilever sensors is described.

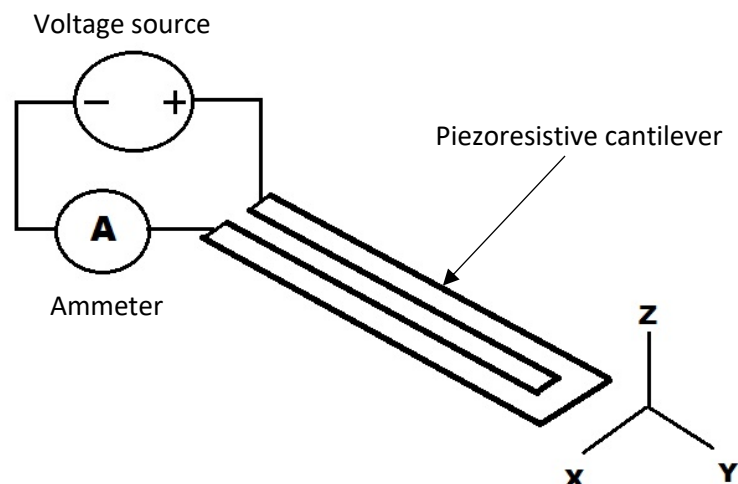


Figure 6.2.1 Basic schematic of proposed piezoresistive cantilever device. When the cantilever is deflected in the Z direction it's resistance will change. If the voltage across the cantilever is kept constant the change in resistance can be determined by measuring the change in current through the ammeter and applying Ohm's law.

The initial step towards realising piezoresistive polycrystalline diamond cantilever sensors (e.g. **Figure 6.2.1**) is to investigate the electrical properties of diamond samples supplied by collaborator Dr Oliver Williams at Cardiff University [6.1]. The boron-doped diamond samples were supplied as thin films grown by microwave plasma chemical vapour deposition on two-inch silicon substrates. After the growth process, the diamond films are polished using a proprietary chemical mechanical process, resulting in a typical roughness of 3 nm Ra. After polishing the thin diamond films are around 400 nm thick (verified by surface profiling), however this is not uniform across the entirety of the wafer. Boron doping is achieved by introducing trimethylboron gas into the CVD chamber during the growth process. Further information on the growth process can be found here [6.16].

To establish the sheet resistance of the diamond films and find a suitable ohmic contact, transmission line measurement (TLM) analysis was conducted. In order to achieve this, metal contacts, defined using electron beam lithography, were evaporated onto the surface of the diamond films by electron beam evaporation. A metal stack comprising of a layer of titanium under a layer of gold was chosen for the contacts: the titanium layer promotes adhesion to the diamond surface as well as having low resistivity, and gold also has low resistivity and is resistant to oxidation [6.17]. From the TLM analysis we can find the resistance contribution of the contacts in addition to the sheet resistance and hence resistivity of the diamond film.

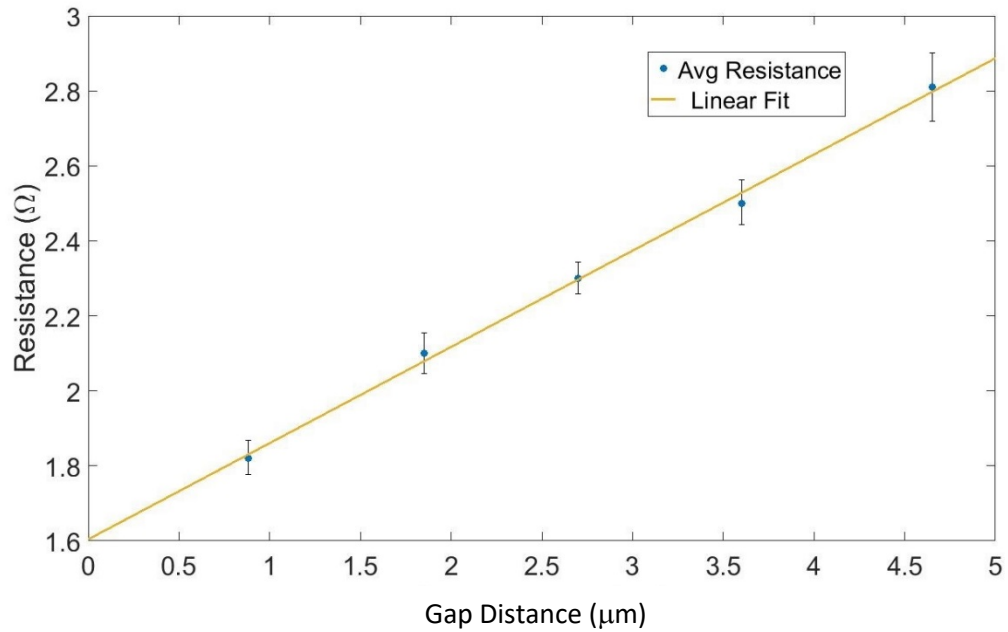


Figure 6.2.1 Plot of resistance vs gap distance for Ti/Au contact TLM measurements. The y-intercept of the linear fit corresponds to twice the contact resistance ($2R_c$). Error bars show data range.

Figure 6.2.1 shows the results from TLM measurements of Ti/Au contacts on boron doped PCD. The surface area of the contacts is $150 \mu\text{m}^2$ and comprises of a 40 nm titanium layer at the diamond interface capped with a 300 nm gold layer. A 0.5 V - -0.5 V sweep was applied between contacts for each gap size. Five separate TLM structures were measured and the resistance for each gap size averaged to plot this data. The gap distances were $0.88 \mu\text{m}$, $1.85 \mu\text{m}$, $2.7 \mu\text{m}$, $3.6 \mu\text{m}$ and $4.7 \mu\text{m}$, verified by SEM imaging. From the y-intercept we find the combined contact resistance, $2R_c$ is 1.63Ω . The contacts exhibit linear ohmic behaviour and as a result the decision was made not to anneal the contacts. As there has been no annealing process, the sheet resistance of the material under the contacts is assumed to be consistent with the sheet resistance between them. Following this assumption, we can use the transfer length derived from the TLM measurement to find the effective contact resistivity, which from this data we find to be $3.75 \times 10^{-6} \Omega \cdot \text{cm}^2$. The gradient of the linear fit to the TLM measurements is equal to the sheet resistance of the sample multiplied by the width of the TLM. Dividing by the TLM width we find the sheet resistance of the material to be $39 \Omega/\square$. For a sample thickness of 400 nm this corresponds to a bulk resistivity of $1.44 \times 10^{-3} \Omega \cdot \text{cm}$ which, according to the plot shown in **Figure 6.2.2** [6.18], finds the resistivity of the diamond sample in the metallic range.

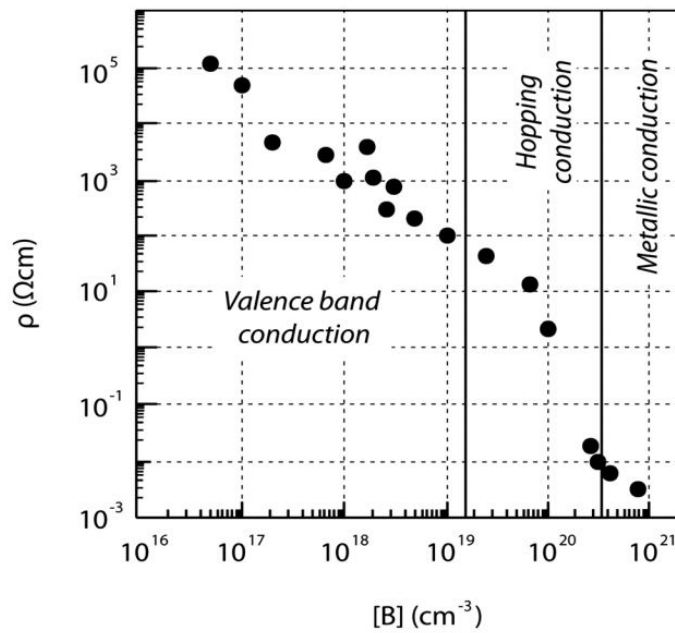


Figure 6.2.2 Resistivity vs Boron doping concentration in polycrystalline diamond (see also Figure 2.5.2) [6.18].

If we are to fabricate cantilevers from the material and observe the piezoresistive effect when deflecting the cantilevers, we must first ensure that the material maintains a constant resistance for a given constant voltage. If the resistivity of the material changes over time for an applied voltage, then it would not be possible to separate resistance changes due to the piezoresistive effect from these fluctuations. Consequently, the next step is to investigate the time dependent stability of the electrical properties of the diamond film. One of the causes for fluctuations in resistivity for a constant voltage could be self-heating of the device as heat is generated from current flow in the material.

To investigate the time dependent resistivity of the material, wires were formed from the diamond films and the resistance of the wires monitored over set time intervals for an applied voltage. To create wires from the doped diamond films, electron beam lithography was used to create wire-shaped etch masks on the surface of the film. Aluminium was used as an etch mask as it is known to have good selectivity versus diamond during the selected RIE etch process [6.19]. The patterned diamond is etched in an RIE plasma etching tool with an Ar/O₂ plasma. This is the same etching process detailed in the previous chapter, however, it is noted that for the same parameters (and same RIE tool) the boron doped diamond etch rate is half that of the intrinsic samples. The decreased etch rate in boron doped samples has also been reported elsewhere, and could be attributed to an increased etching resistance to O₂ plasma on the diamond lattice's <111> plane owing to boron concentration there [6.20].

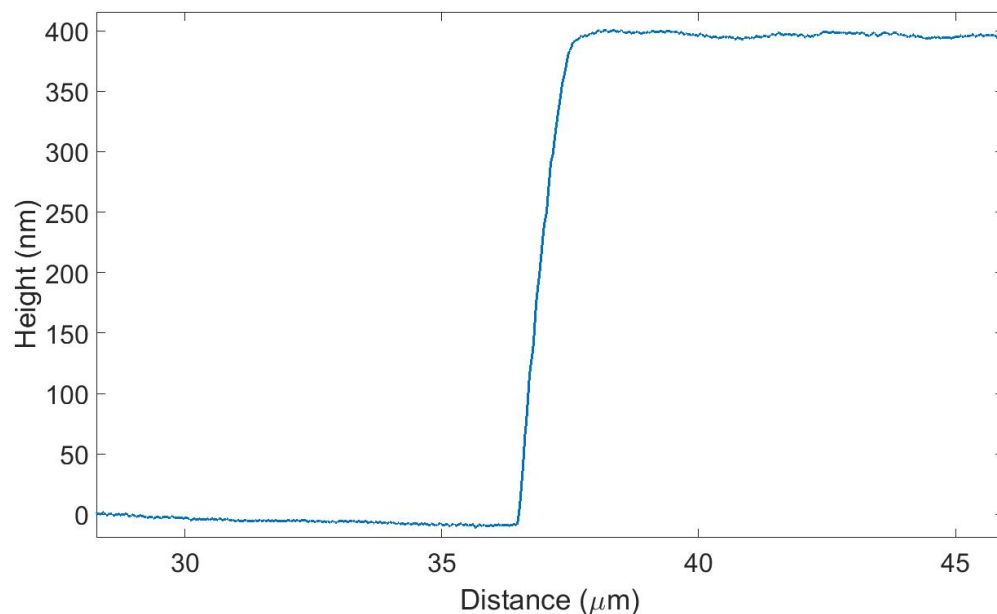


Figure 6.2.3 Diamond film thickness as measured by surface profiling. To the left of the graph is the silicon substrate surface and the plateau on the right is the diamond film showing a height of 400 nm.

After etching is complete, the aluminium mask is removed by soaking the sample in MF-CD26 developer and optically inspected for residue. At this stage in the process, surface profiling can be used to determine the thickness of the diamond film. A Dektak XT stylus profiler was used and the thickness of the diamond film was found to be approximately 400 nm, as shown in **Figure 6.2.3**. A further electron beam lithography step is used to define the metal contacts for performing electrical measurements on the wires. The same Ti/Au contacts used for the TLM measurements are used in this instance and are metallised onto the surface of the diamond using electron beam evaporation.

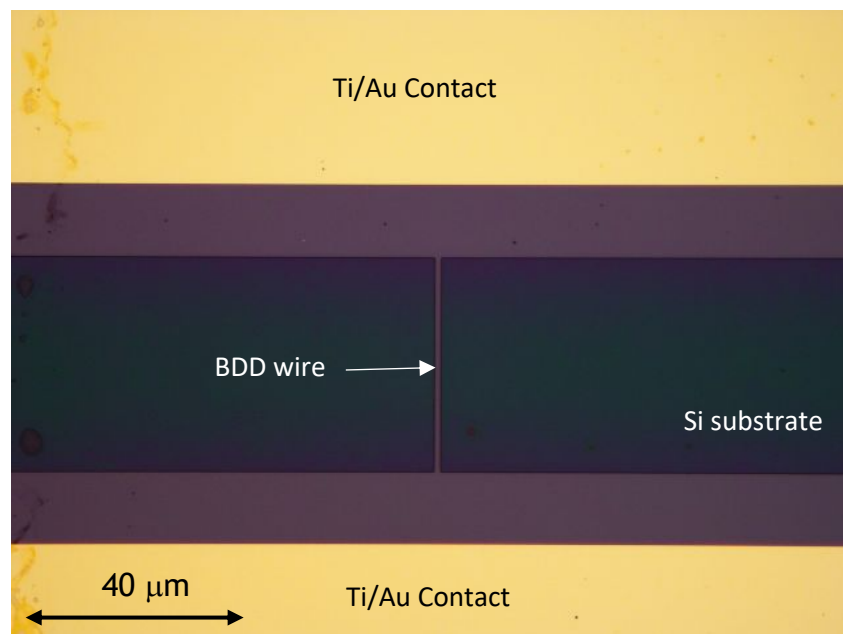


Figure 6.2.4 Optical image of complete microwire structure including Ti/Au contacts. The wire shown is 1 μm wide, 40 μm long and 0.4 μm thick.

An Agilent B1500 semiconductor parameter analyser is used to perform electrical measurements on the diamond wires. A voltage is applied between two wires in turn, and the current sampled at 20 ms intervals for 60 seconds. The current remains constant across the 60 second interval within the investigated voltage range. Similar results were consistent across all wire dimensions ranging from 40 μm .

6.3 Boron-doped PCD Cantilever Fabrication

We now turn to look at potential designs for current carrying cantilever beams. Essentially, these cantilevers are suspended piezoresistors. It was noted at this point that, owing to the inclusion of metal contacts in these devices, fabrication processes established earlier in this work for releasing free standing cantilever type structures would be incompatible with these devices. Silicon processing is highly sensitive to metal contamination, so with the addition of metal contacts on these devices and shared laboratory equipment plasma silicon processing is ruled out. As an alternative to plasma processing to release cantilever type structures, wet etch release techniques are investigated. Previously reported cantilever release process development in this work utilise a potassium hydroxide (KOH) 'dip' to remove minimal amounts of excess silicon from beneath partially released cantilever structures. KOH selectively etches silicon dependent on the crystal orientation of the material. The PCD samples received from our collaborator are grown on silicon $\langle 100 \rangle$. Therefore, it should be possible to achieve a full cantilever release by exclusively wet etching the samples in a KOH solution. This release method, however, introduces a new problem. The metal contacts used to investigate the electrical properties of the samples detailed earlier in this chapter utilised a Ti/Au stack. KOH not only etches silicon but also etches Ti (and Au to a lesser extent), so an alternative ohmic metallisation must be investigated that will withstand the KOH release process. Nichrome (NiCr) is a popular alloy used for contact adhesion layers owing to its high bonding strength [6.21]. NiCr has a much higher resistivity than Ti, so further TLM analysis was performed to investigate the contact resistance and suitability for this material to be used for contacts on the boron doped PCD.

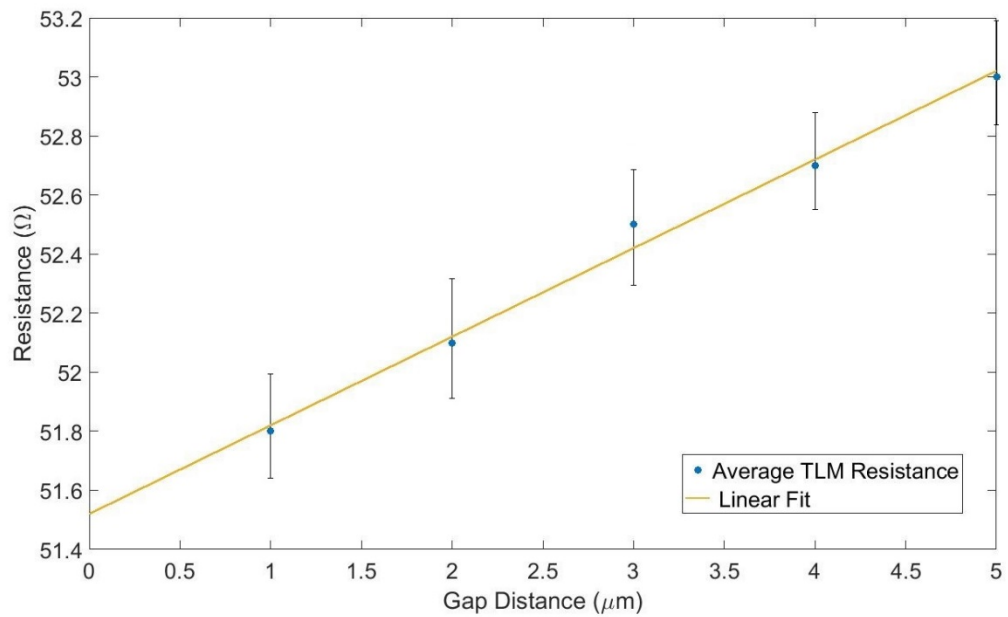


Figure 6.3.1 Plot of resistance vs gap distance for NiCr/Au contact TLM measurements. The y-intercept of the linear fit corresponds to twice the contact resistance ($2R_c$). Error bars show data range.

The contacts for these measurements are deposited by electron beam evaporation and consist of a 10 nm layer of NiCr at the diamond interface capped by 300 nm of Au. In comparison to the Ti/Au TLM data shown earlier, the NiCr/Au contacts showed a higher variation in resistance data. This could be attributed to poor contact adhesion between the NiCr layer and diamond surface in comparison to the Ti/Au stack. However, the TLM data was consistent enough to verify the NiCr/Au contacts as a suitable alternative to the Ti/Au stack. From the NiCr/Au TLM data we find the contact resistivity to be $1.2 \times 10^{-3} \Omega \cdot \text{cm}^2$, more than 2 orders of magnitude higher than the Ti/Au contacts.

Having established that NiCr/Au is a suitable contact metal stack, a design for an array of suspended micro-cantilevers was composed. The design consists of several U-shaped cantilevers of varying length and thickness as demonstrated in **Figure 6.3.2**.

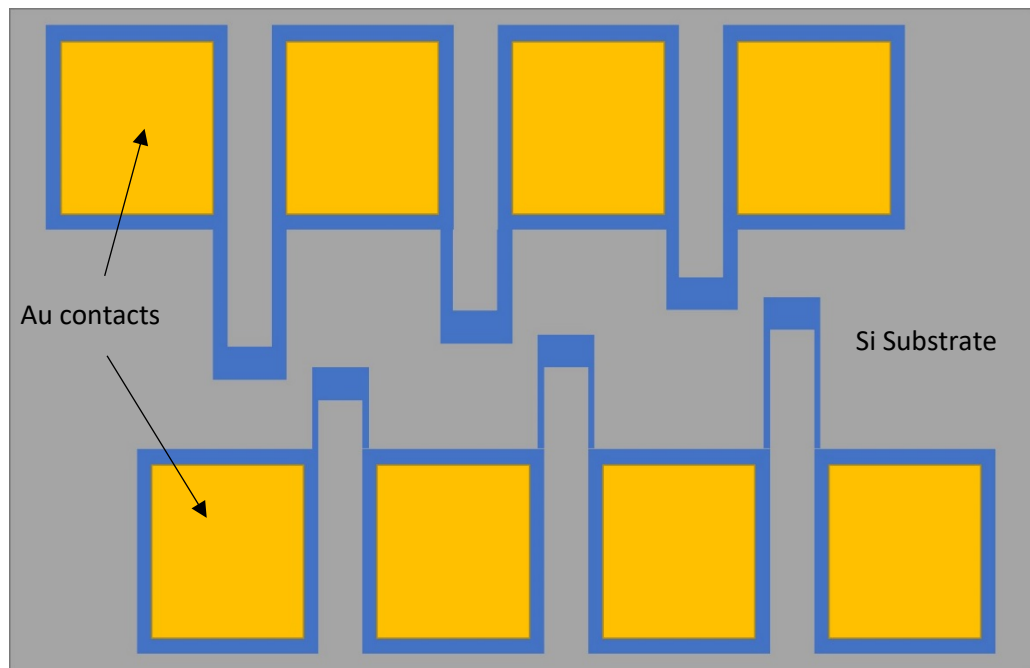


Figure 6.3.2 Graphical design plan for piezoresistive cantilever array with beam length ranging from 60 μm to 110 μm . Dimensions not drawn to scale.

By following the same process as described previously for fabricating wires from the diamond, the cantilever patterns are etched into the diamond thin film. Following the diamond etch process, a further electron beam lithography step is used to define the contacts onto the diamond film surface. NiCr/Au contacts are metallised onto the diamond surface using electron beam evaporation with respective thickness of 10 nm/400 nm. Once the contacts are metallised the sample is ready for the cantilever release process. The samples were submerged in a 30% KOH solution in an acid reflux etching kit for 10 minutes at 100 degrees. The expected etch rate as taken from literature for this process is around 10 $\mu\text{m}/\text{minute}$ [6.11]. After the 10 minute KOH etch the samples are inspected with an SEM tool.

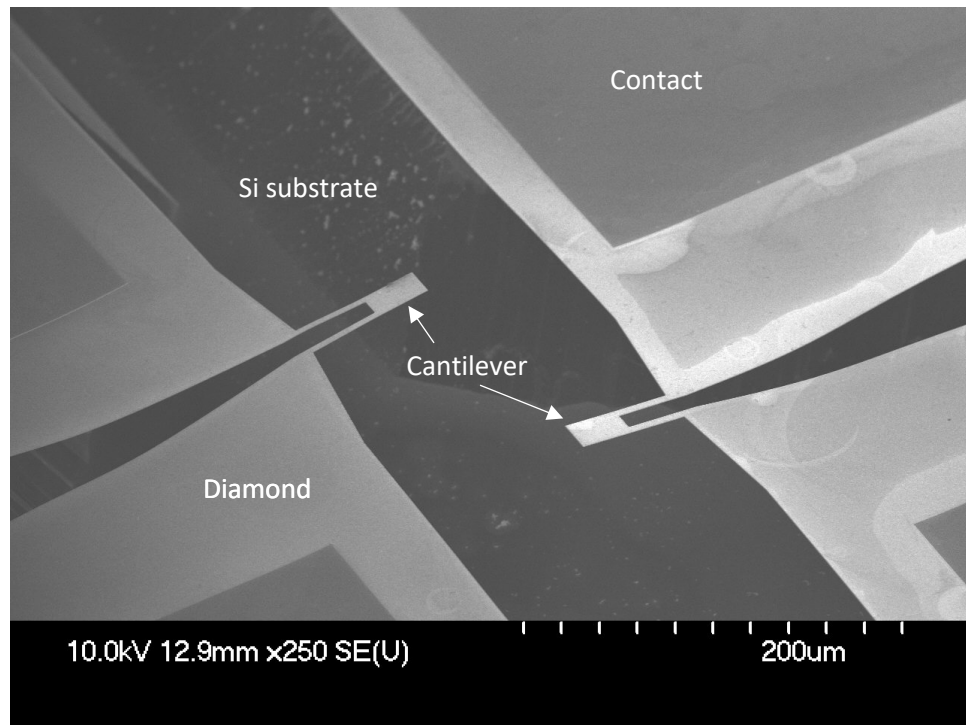


Figure 6.3.3 SEM image of BDD cantilever beams post KOH release etch.

As can be seen from the SEM images in **Figures 6.3.3**, the cantilevers are successfully released from the silicon substrate, however the KOH process has left the devices with a large undercut that extends below the area where the contacts are positioned. An investigation into the impact of this undercut on device performance is provided later in this chapter. At this stage it becomes apparent that the diamond films are experiencing significant residual stress. Due to this mechanical stress, the cantilevers with smaller more fragile features shear apart at stress points as displayed in **Figure 6.3.5**. This significantly reduces the device yield from this sample. However, the cantilevers with wider legs survive the release process. This residual stress is a well-documented phenomenon and has been attributed to different factors including varying thermal expansion coefficients of the diamond material and the silicon substrate during cool-down after the growth process, as well as non-diamond carbon content within the diamond crystal [6.22].

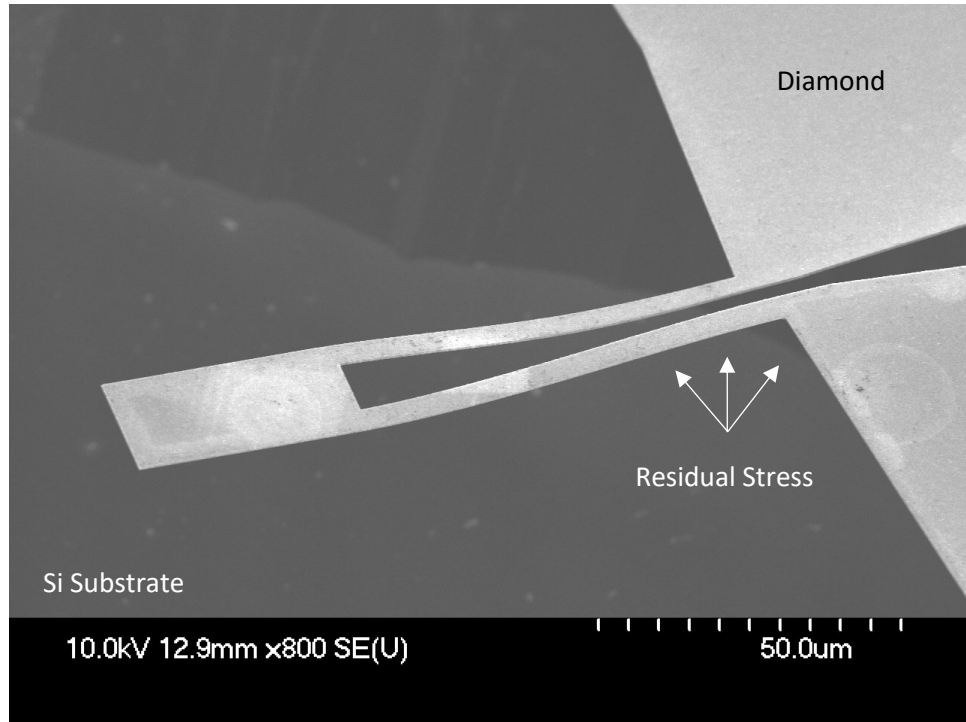


Figure 6.3.4 SEM image of BDD cantilever showing bending as a result of residual stress in the diamond film.

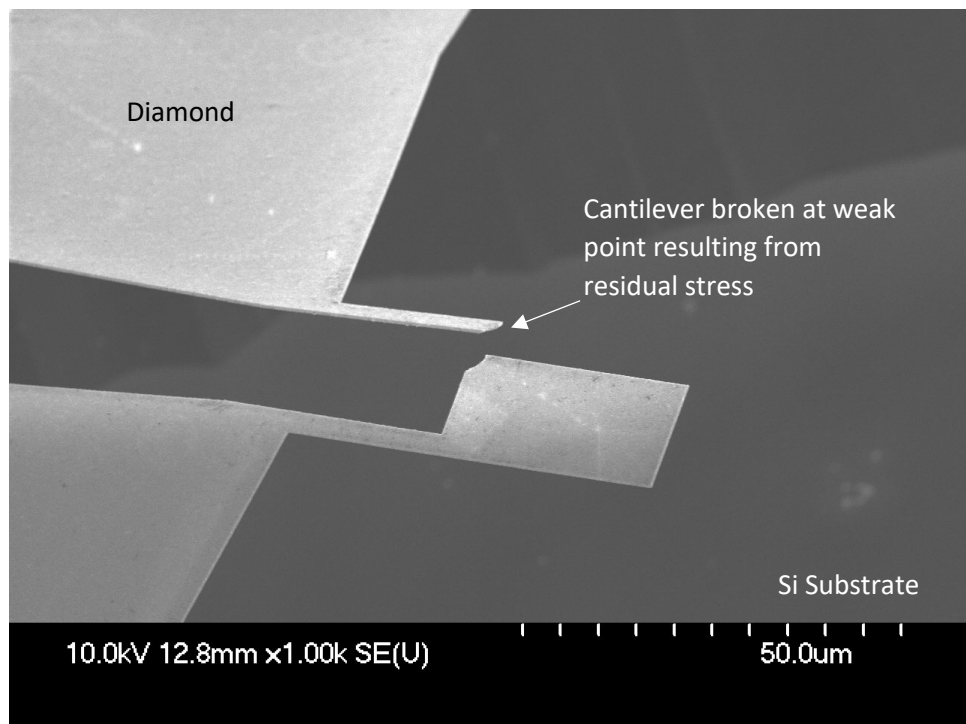


Figure 6.3.5 SEM image of BDD cantilever destroyed by residual stress in the diamond film.

The final step towards completing the cantilever devices is to consider packaging for characterisation. The thin metal contacts on the devices are fragile and will not withstand repeated probing without becoming mechanically compromised. The solution to this is to secure the sample to a suitable carrier featuring more substantial contacts and wire bonding the contacts on the devices to the contacts on the carrier. The ADAfruit SMT breakout printed circuit board (PCB) was found to be a suitable carrier for the sample. The breakout board features a 10x10 mm footprint surrounded by 32 Au solder pads 1mm in pitch and 500 μm thick. This coincides with 10x10 mm footprint of the sample and the Au contacts on the devices. Common metals used in wire bonding are Cu, Au and Al. The combination of Au solder pads and contacts allows increased bond adhesion with Au wire.

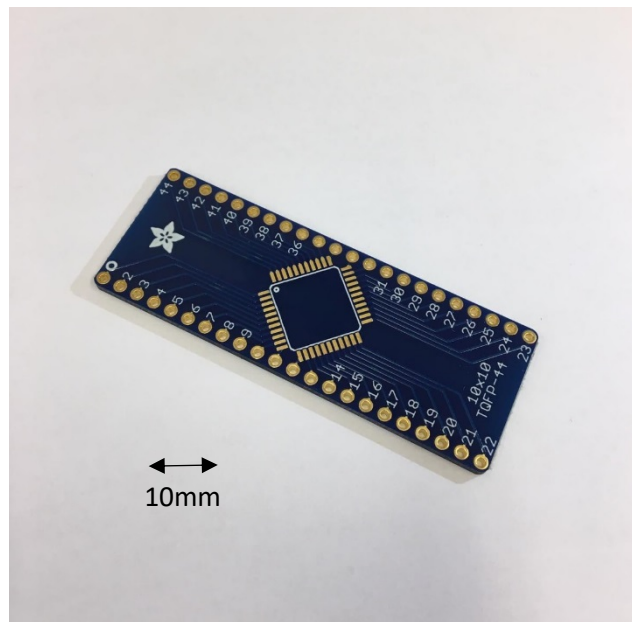
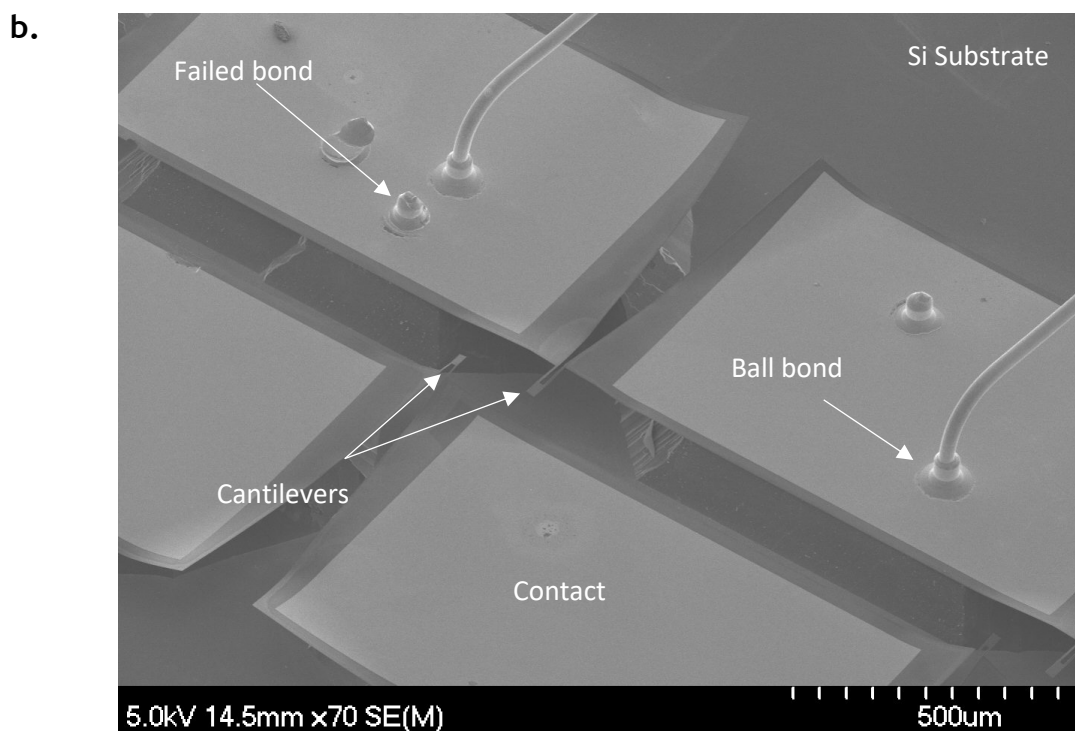
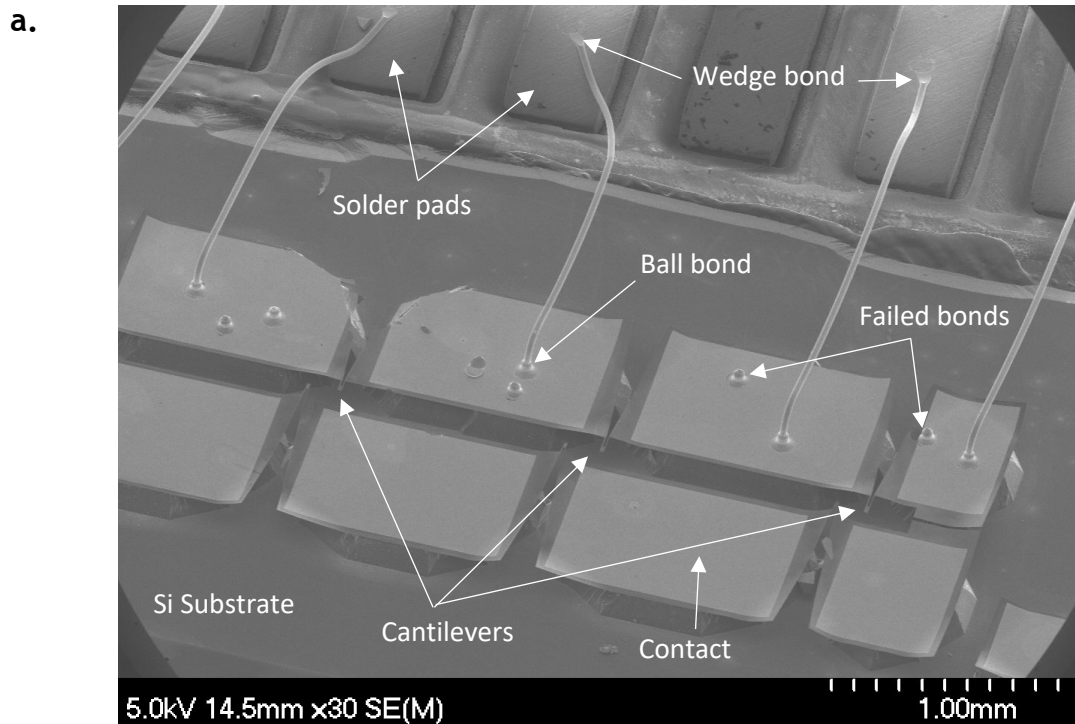


Figure 6.3.6 TQFP-44 IC breakout board (ADAfruit).

The sample is glued to the centre of the breakout board on the 10x10 mm IC footprint. To wire bond the contacts to the solder pads on the breakout board, a K&S IBond5000 ball bonder was utilised. The ball bonder uses 20 μm diameter Au wire and performs two types of bond: the initial bond is a ball bond and the secondary bond is a wedge (or ‘tail’) bond. The ball bond has increased adhesion in comparison to the wedge bond, so this was performed on the thin contact and the wedge bond performed on the thicker solder pad. Starting from a factory pre-set for Au bonding, the following parameters were found to make sufficient bonds to the contacts and solder pads:

	Ultrasonic Power	Time	Force
Ball Bond	4	4	4
Wedge Bond	4	4	4

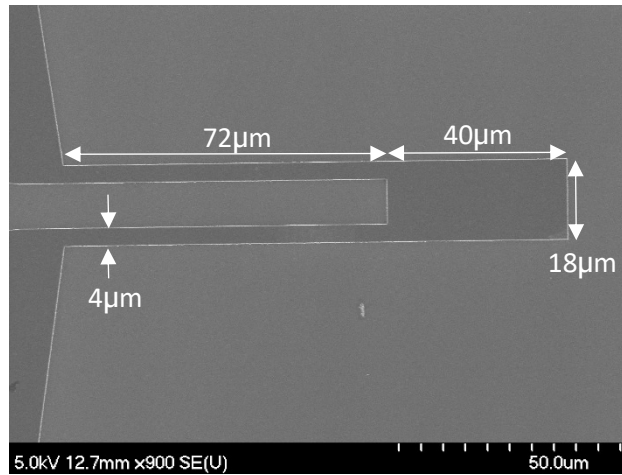
Table 6.3.1 Table of normalised bonder parameters. Actual parameter ranges from the manufacturer are: *Power* = 1.3-2.5 Watts, *Time* = 10 - 1000 ms and *Force* = 10 - 250 g.



Figures 6.3.7 a & b SEM images of BDD cantilever beams after wire bonding.

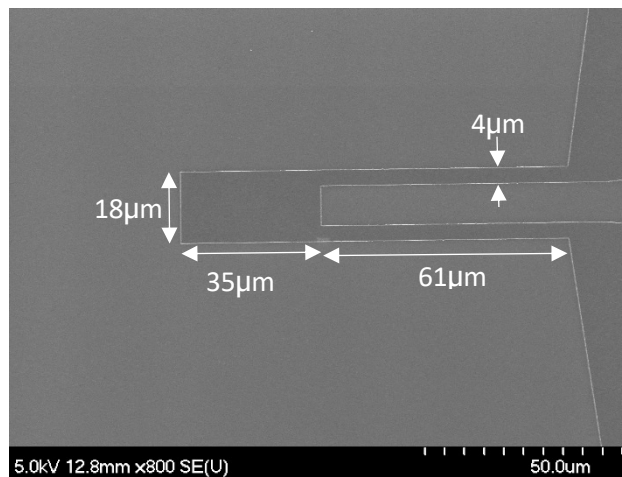
The SEM images in **Figures 6.3.7 a & b** show the devices after successful bonding. The described process yields three useable devices, cantilever A, B and C, shown in **Figures 6.3.8 a b & c**

a.



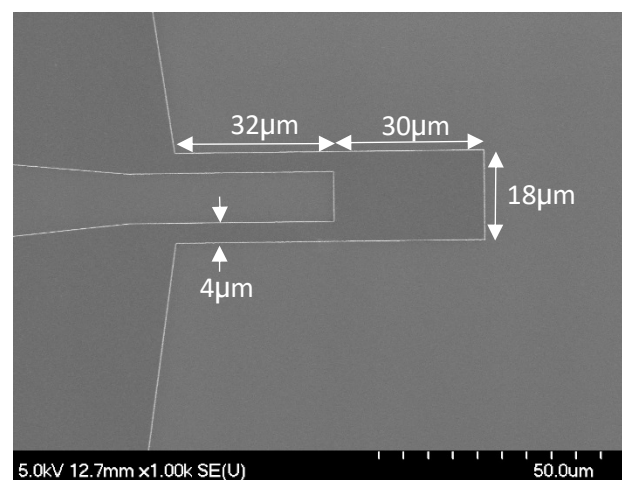
Cantilever A

b.



Cantilever B

c.



Cantilever C

Figure 6.3.8 a, b & c SEM image showing cantilevers A, B & C pre-release etch and their dimensions.

6.4 Chapter Summary

The fabrication of MEMS devices from intrinsic and boron-doped PCD has been presented. Wet and dry etch processes have been developed in order to overcome the difficulties presented with fabricating free standing micro-structures, such as etch anisotropy, structure release and process compatibility. Two fully realised sets of devices are presented: an intrinsic PCD microcantilever array for passive measurements, and a boron-doped piezoresistive micro-cantilever array for force sensing, wire bonded into a test package. The following chapters detail the characterisation of these devices.

References

- [6.1] EL Thomas, GW Nelson, S Mandal, JS Foord and OA Williams “ Chemical Mechanical Polishing of Thin Film Diamond” *Carbon*, Vol 68, pp 473, 2018.
- [6.2] OA Williams, M Nesladek, M Daenen, S Michaleson, A Hoffman, E Osawa, K Haenen and RB Jackman, “*Growth, electronic properties and applications of nano-diamond,*” *Diamond and Related Materials* Vol 17 pp. 1080, 2008.
- [6.3] J. Lu, Z. Cao, D. M. Aslam, N. Sep, and J. P. Sullivan, “Diamond Micro and Nano Resonators Using Laser , Capacitive or Piezoresistive Detection,” *2008 3rd IEEE International Conference on Nano/Micro Engineered and Molecular Systems*, pp. 873-876, 2008.
- [6.4] Y. Ando, Y. Nishibayashi, K. Kobashi, T. Hirao, and K. Oura, “Smooth and high-rate reactive ion etching of diamond,” *Diamond and Related Materials*, vol. 11, pp. 824-827, 2002.
- [6.5] O. Dorsch, M. Werner, E. Obermeier, R.E. Harper “Etching of Polycrystalline Diamond and Amorphous Carbon Films by RIE” *Diamond and Related Materials* Vol 1(2-4) pp. 277-28, 1992.
- [6.6] P. Leech, G. K. Reeves, A. Holland, “Reactive ion etching of CVD diamond in CF₄/O₂, O₂ and O₂/Ar plasmas” *MRS Online Proceedings Archive* 622:T6361-T6366, 2000.

- [6.7] S.Iliasa, G.Senéa, P.Möllera, V.Stamboulia, J.Pascallona, D.Bouchiera, A.Gicquelb, A.Tardieub, E.Angerb, M.F.Ravetc, “Planarization of diamond thin film surfaces by ion beam etching at grazing incidence angle,” *Diamond and Related Materials*, Volume 5, Issues 6-8, Pages 835-839, 1996.
- [6.8] E. Gogolides , C. Boukouras, G. Kokkoris, O. Brani, A. Tserepi, V. Constantoudis, “Si etching in high-density SF₆ plasmas for microfabrication: surface roughness formation,” *Microelectronic Engineering*, Vol 73-74, pp. 312-318, 2004
- [6.9] R. KnzikeviWiusa, V. Kopustinskas, “Anisotropic Silicon Etching in SF₆ Plasma,” *Vacuum*, Vol 77, pp 1-4 2004
- [6.10] Robert L. Bates, P.L. Stephan Thamban, Matthew J. Goeckner and Lawrence J. Overzet, “Silicon Etch Using SF₆/C₄F₈/Ar Gas Mixtures,” *Journal of Vacuum Science & Technology A*, Vol 32, No 4, 2014.
- [6.11] J. K. Park, J. W. Park, “Fabrication of diamond tip cantilever and its application to tribo-nanolithography,” *2005 International Symposium on Computational Intelligence in Robotics and Automation*, June 2005.
- [6.12] J. Bausells, “Piezoresistive cantilevers for nanomechanical sensing,” *Microelectron. Eng.*, vol. 145, pp. 9-20, 2015.
- [6.13] M. Possas-abreu, F. Ghassemi, L. Rousseau, E. Scorsone, E. Descours, and G. Lissorgues, “Development of Diamond and Silicon MEMS Sensor Arrays with Integrated Readout for Vapor Detection,” pp. 1-15, 2017.
- [6.14] Y. Tang, D. M. Aslam, J. Wang, and K. D. Wise, “Study of polycrystalline diamond piezoresistive position sensors for application in cochlear implant probe,” vol. 15, pp. 199-202, 2006.
- [6.15] S. L. Karsten, M. C. Tarhan, L. C. Kudo, and D. Collard, “Talanta Point-of-care (POC) devices by means of advanced MEMS,” *Talanta*, vol. 145, pp. 55-59, 2015.
- [6.16] G. M. Klemencic, S. Mandal, J. M. Werrell, S. R. Giblin, and O. A. Williams, “Superconductivity in planarised nanocrystalline diamond films,” *Sci. Technol. Adv. Mater.*, vol. 18, no. 1, pp. 239-244, 2017.

- [6.17] E. Films, H. Shiomi, Y. Nishibayashi, N. Fujimori, H. Mukuda, T. Tsuchida, D. Diamond, E. Films, H. Shiomi, Y. Nishibayashi, N. Fujimori, and A. Schottky, "Related content Electrical Characteristics of Metal Contacts to Boron-Doped Diamond Epitaxial Film," 1989.
- [6.18] J. V. Macpherson, "A practical guide to using boron doped diamond in electrochemical research," *Phys. Chem. Chem. Phys.*, vol. 17, no. 5, pp. 2935-2949, 2015.
- [6.19] D. S. Hwang, T. Saito, and N. Fujimori, "New etching process for device fabrication using diamond," *Diamond and Related Materials*, vol. 13, pp. 2207-2210, 2004.
- [6.20] D. Lia, L. Gou, J. Xu, K Gao, X Kang, "Investigations on etching resistance of undoped and boron doped polycrystalline diamond films by oxygen plasma etching," *Vacuum*, Vol 128 pp 80-84, 2016.
- [6.21] E. D. Luckowski, J. M. Delucca, J. R. Williams, S. E. Mohny, M. J. Bozack, T. Isaacs-Smith, and J. Crofton, "Improved ohmic contact to n-type 4H and 6H-SiC using nichrome," *Journal of Electronic Materials*, vol. 27, no. 4, pp. 330-334, 1998.
- [6.22] C. T. Kuo, C. R. Lin, and H. M. Lien, "Origins of the residual stress in cvd diamond films," *Thin Solid Films*, vol. 290-291, no. 1, pp. 254-259, 1996.

Chapter 7: Device Characterisation Results I

The forthcoming chapter details the characterisation of intrinsic PCD micro-cantilevers, the fabrication of which is presented in **Sub-Chapter 6.1**. The thermal fluctuations of the devices are characterised in air and water. Methods to maximise cantilever displacement and hence increase signal to noise ratio are discussed. A data analysis method is presented to extract a fluid's viscoelastic properties from the power spectrum of the thermal fluctuations of submerged cantilevers.

7.1 Cantilever Thermal Response

Having succeeded in fabricating free standing PCD micro-cantilevers, the next step was to attempt to characterise the thermal response of the devices at room temperature. As per the method described by Tassieri *et al* for optical tweezers, the intention was to plot the mean squared displacement (MSD) (or position autocorrelation function (PAF)) of the thermal fluctuations at the free end of the cantilever beams [7.1]. From the variance of the time-displacement series the stiffness of the cantilever can be calibrated using the equipartition theorem described in **Chapter 2**, and the MSD (or PAF) can be normalised by the variance and used for further data analysis. As described in **Chapter 2**, the cantilever and its surroundings are to be considered as a homogenous mechanical system having both elastic and viscous properties, with the cantilever being the dominant elastic contribution and the surrounding fluid the dominant viscous contribution working in parallel. By calibrating cantilevers of varying size in a fluid of known viscosity we can extract the cantilever drag coefficient (for specific cantilever dimensions) and hence calibrate the system for further measurements.

A Polytec UHF laser doppler vibrometer (LDV) system was used to measure the thermal fluctuations of the fabricated cantilevers as described in **Chapter 5**. The sample was placed under the focusing lens of the LDV and the laser spot focussed on to the tip of each cantilever. The LDV software records data as a time series of displacements or as the frequency spectrum of the cantilever's motion.

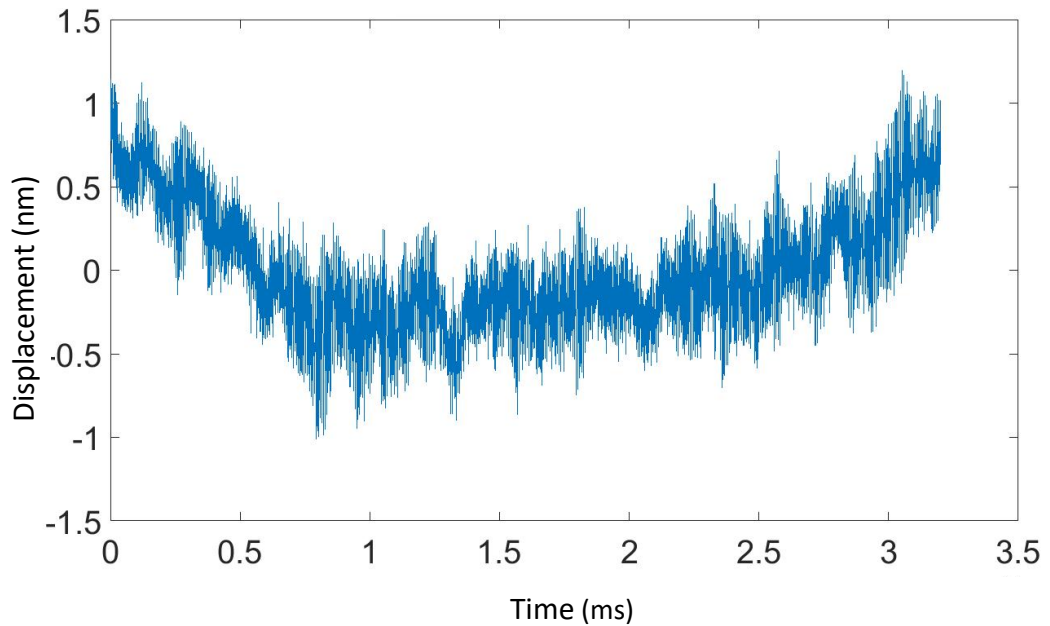
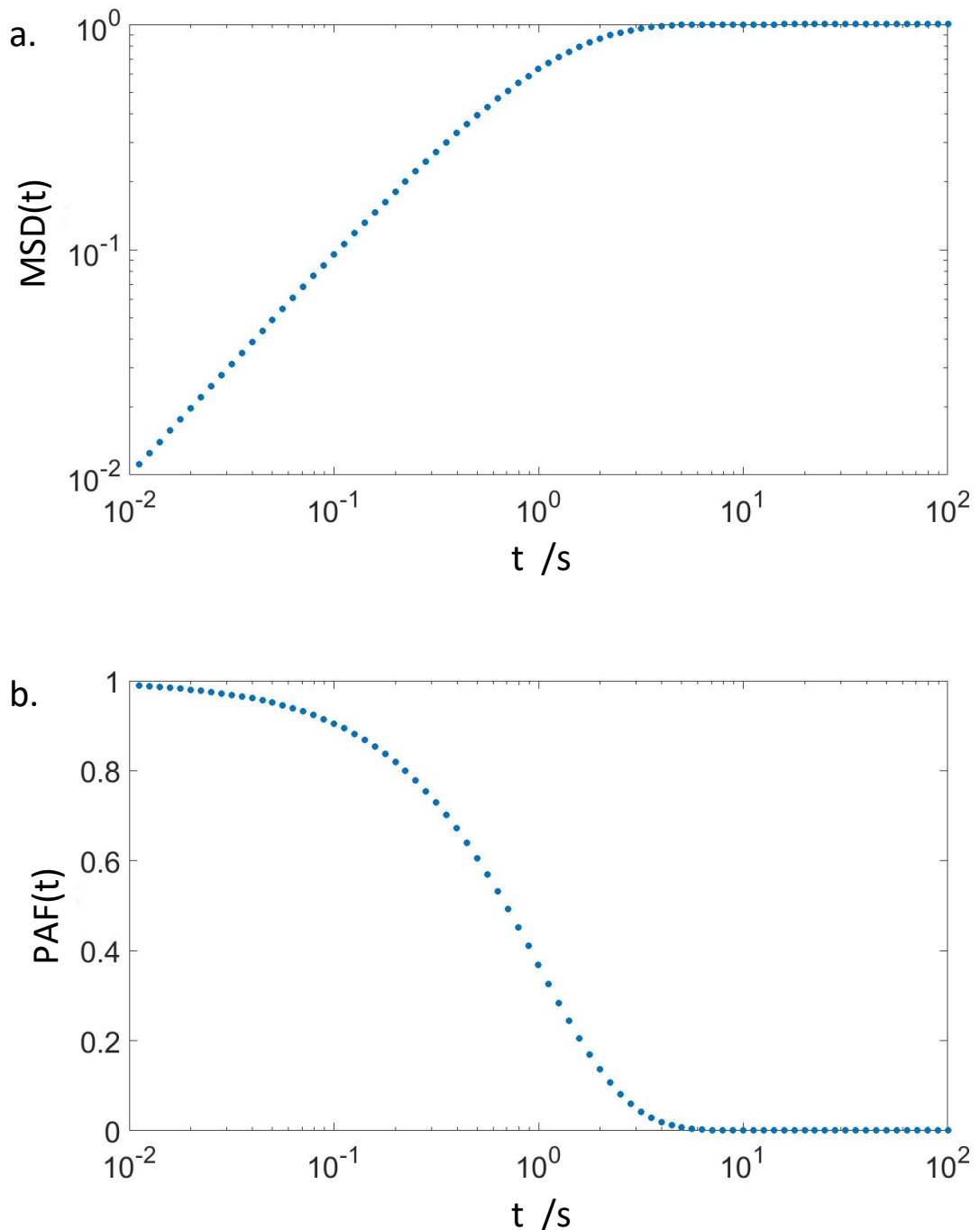


Figure 7.1.1 The thermal fluctuation of a $4\ \mu\text{m} \times 80\ \mu\text{m} \times 0.48\ \mu\text{m}$ cantilever beam sampled at 2.5 GHz.

Figure 7.1.1 shows the time vs displacement plot of the thermal fluctuations of the free end of a $4\ \mu\text{m} \times 80\ \mu\text{m} \times 0.48\ \mu\text{m}$ cantilever beam in air at room temperature and sampled at 2.5 GHz. Humidity in the lab, which could affect the cantilever dynamics, was not evaluated but assumed to be constant for all measurements. To acquire enough data to form the MSD plot the data must be sampled for a sufficiently long period of time such that the plot reaches a plateau as demonstrated by synthetic test data (generated in Excel) in **Figure 7.1.2** a below. The data in **Figure 7.1.1** is raw, as taken directly from the LDV system. The stiffness of the cantilevers can be estimated from the device's geometry and material properties, and from the estimated stiffness we can use the equipartition theorem described in **Chapter 2** to find an estimated displacement. The expected displacement for the cantilevers shown is in the pico-meter range, however the plot shown in **Figure 7.1.1** shows an overall trend extending into the nanometre range, which could be attributed to low frequency drift or interference. Typically, the data is not centred around zero on the x-axis, so initially we must first calculate the mean of the data values and subtract it from the original data so

that the mean of the signal is zero. This ensures a correct interpretation of the variance value. The data can appear distorted at low frequency if the device has physically drifted during the measurement. This can be alleviated by de-trending using a least-squares fit, however, care must be taken as too much filtering can distort the data further.



Figures 7.1.2 a & b MATLAB plots of the MSD (a) and PAF (b) of synthesised test data for a single decaying exponential function $y = e^{-\alpha t}$. The normalised MSD (NMSD) and PAF (NPAF) have the relationship $NMSD + NPAF = 1$

The time series data captured by the LDV is analysed by means of a MATLAB code. The auto-correlation of the time series data returns the PAF of the cantilever tip. As it can be seen from **Figure 7.1.3** the NPAF plotted from the time series data captured bears only a slight resemblance to the generated ideal data in **Figures 7.1.2 a & b** above. This data has been normalised by the variance of the time series in **Figure 7.1.1**.

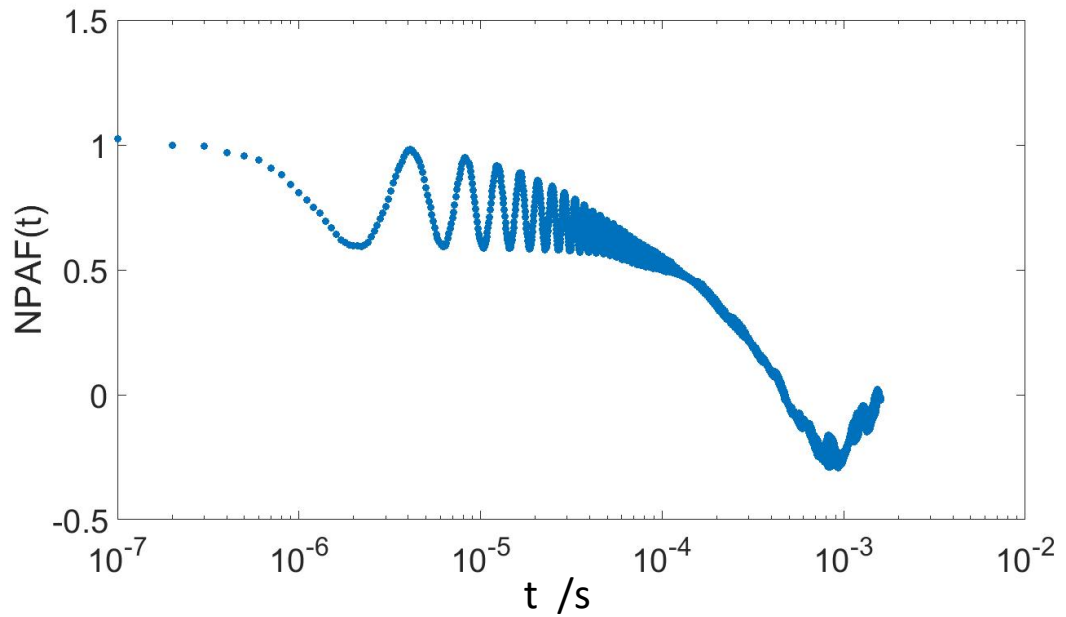


Figure 7.1.3 NPAF plot time series data captured from the thermal fluctuations of a 3 μm x 80 μm x 0.48 μm cantilever beam. Data normalised by the variance of the original time series data.

Three things can be noted from **Figure 7.1.3**: Firstly, there is a clear oscillation with a time period of approximately 4.1 μs . This corresponds to the resonant frequency (~ 250 kHz) of the cantilever as can be seen in **Figure 7.1.4**. This resonant frequency can be verified analytically by using **Equation 2.2.18** from **Chapter 2**:

$$\omega_1 = \beta_1^2 \sqrt{\frac{EI}{mL^4}}$$

Where $\beta_1 = 1.88$ for the first natural frequency, mass, $m = \text{density}, \rho \times \text{cross sectional area}, A$, and I is Equation 2.1.2 for the moment of inertia. Therefore, for a cantilever of width, length and thickness $3 \mu\text{m} \times 70 \mu\text{m} \times 0.48 \mu\text{m}$, we have:

$$\begin{aligned}\omega_1 &= 1.88^2 \sqrt{\frac{E(WH^3/12)}{\rho(WH)L^4}} = 1.88^2 \sqrt{\frac{EH^2}{12\rho L^4}} \\ &= 3.5344 \sqrt{\frac{900 \times 10^9 * (0.48 \times 10^{-6})^2}{12 * 3510 * (70 \times 10^{-6})^4}} = 1.6 \times 10^6 \text{ rad/s} \\ &\approx 250 \text{ kHz}\end{aligned}$$

Secondly, the plot does not accurately scale from 1 to 0 when normalised, and lastly, the plot does not settle around a single value (or plateau) at long time scales as expected.

It is believed that oscillations at the resonant frequency of the cantilever are present in the PAF because the system is underdamped. The elastic energy of the cantilever owing to the high acoustic velocity of the material is dominating the mechanics of the system.

The nature of the poor normalisation and absence of a plateau at long lag times can be attributed to more than one source of error. If the measurement is too short the measured variance could be inaccurate as the signal does not statistically contain enough data to represent how the cantilever behaves. The longer the signal, the more accurate the variance will be, with the value eventually reaching a plateau. The final value is related to the stiffness of the cantilever and does not change in different fluids. However, the length of time that the system takes to reach the final value is dependent on the fluid. The more viscous the fluid, the longer the cantilever fluctuations take to reach maximum variance. Owing to software limitations the LDV system has a maximum measurement length of 3.2ms which may not be sufficiently long enough. Another source of error could be fluctuations of the entire mechanical system owing to environmental influences within the lab such as technical noise mechanically coupling from equipment

elsewhere in the building such as air conditioning systems and movement from human traffic within the lab itself. These environmental factors translate as low frequency fluctuations imposed onto the cantilever's thermal fluctuations. This kind of low frequency low amplitude technical noise has been reported elsewhere [7.2]. Low frequency interference could also be related to the phenomena of $1/f$ noise, the nature of which has been debated for numerous systems and is reported elsewhere as a limiting factor in low frequency and magnitude measurement systems [7.3]. The term low frequency can be misleading: low frequency is relative to the sample rate and device resonant frequency, and so for the purpose of these analyses can be defined as interference occurring at less than around 20 kHz. We can look at the Fourier transform of the signal to acquire more information about it.

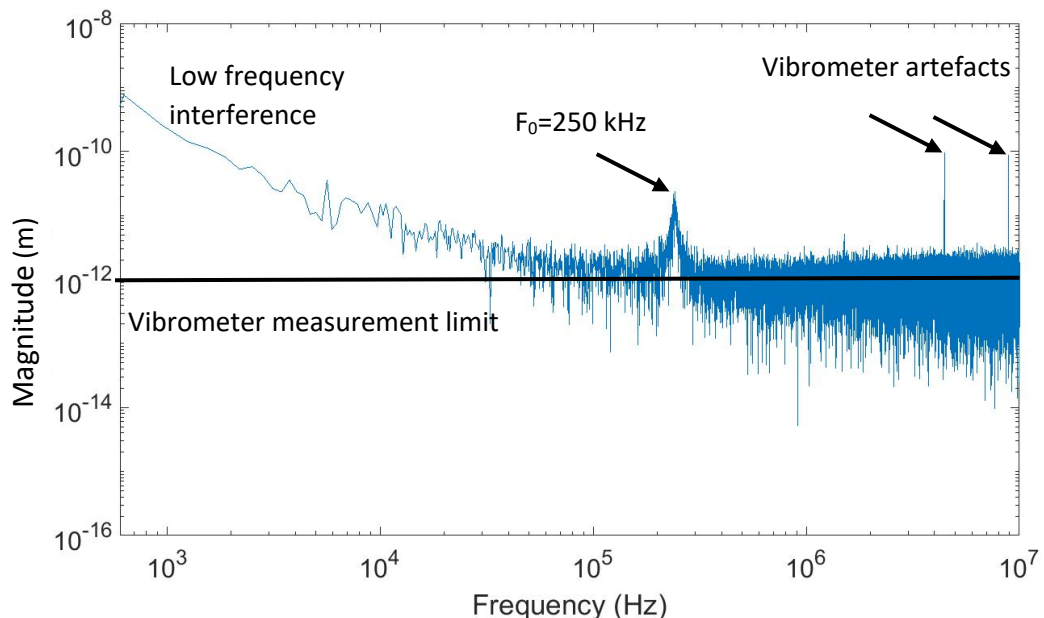


Figure 7.1.4 Frequency response plot (dual log) of a $4 \mu\text{m} \times 70 \mu\text{m} \times 0.48 \mu\text{m}$ cantilever beam's thermal fluctuations in air plotted in MATLAB.

Figure 7.1.4 shows the power spectrum of the thermal fluctuations in air of a $4 \mu\text{m} \times 70 \mu\text{m} \times 0.48 \mu\text{m}$ cantilever beam. MATLAB is used to take the Fourier transform of the original time series data. The relationship between the frequency resolution and the time series is f_s/N , where f_s is the sampling frequency and N is the number of samples. The fundamental resonant peak can be seen at 250 kHz, which is verified by arithmetic calculations based on cantilever geometry and mechanical properties. The resonant peak is set firmly within the noise floor of the measurement systems capabilities. The resulting low signal to noise ratio

(SNR) destroys any useable data outside the limits of the resonant peak where the displacement characteristics of the cantilever are more influenced by the compound system's viscous dampening component. Also present in the power spectrum are artefacts introduced by the measurement system. These artefacts could be attributed to laser speckle, a phenomena resulting from scattered laser light reflections interfering constructively and destructively with one another [7.4][7.5]. These artefacts are present in all of the measurements taken on this system above 4 MHz which severely limits the ability to perform high frequency measurements. Attempts were made to work around the artefacts by manually removing the affected data bins and either interpolating or zero-padding between data points. However, it was found that subsequent data analysis steps described later were sensitive to these methods and an adequate work around could not be found by the author. Lower sample rates also affect the displayed average noise level (DANL) of the measurement. The maximum achievable frequency resolution of the measurement increases with sample rate. At lower frequency resolution we see higher DANL, decreasing the SNR ratio of the measurement. The magnitude of the low frequency interference also extends above the maximum displacement of the cantilever beam at resonance. This again destroys any useable portion of data from cantilever displacement at these frequencies.

The simple free end cantilever beam structure was kept constant throughout the devices, however, it was decided that only one geometrical factor should vary per iteration of device. In the original designs both width and length increased with each device. Calibration of the devices in a known fluid would have been complicated by the variation of more than one geometrical factor (width and length). By changing only the length of devices, calibration would become dependent on only one geometrical factor. Henceforth, only cantilever structures varying only in length were characterised.

In order to try to minimise noise in the LDV measurements, data averaging was investigated. As the driving mechanism is derived from the thermal motion of the fluid's particles surrounding the cantilever, the fluctuations of the cantilever are stochastic in nature. The thermal fluctuations drive the cantilever to resonance but there are also random movements owing to the stochastic nature of the excitation which results in a noisy signal. Averaging the signal in the time domain would remove the random fluctuations and leave only the resonant features of

the signal, thus giving a false representation. This is because at long time scales a random signal will average to zero. In order to retain the information pertaining to the random motion of the cantilever but reduce unwanted noise, the decision was made to capture data from the devices in the frequency domain and average the magnitudes of the fluctuations. Then, from the averaged magnitude spectrum the power spectral density (PSD) can be calculated. In accordance with the Wiener-Khinchin theorem, the autocorrelation of the signal can be found by taking the inverse Fourier transform of the PSD [7.6].

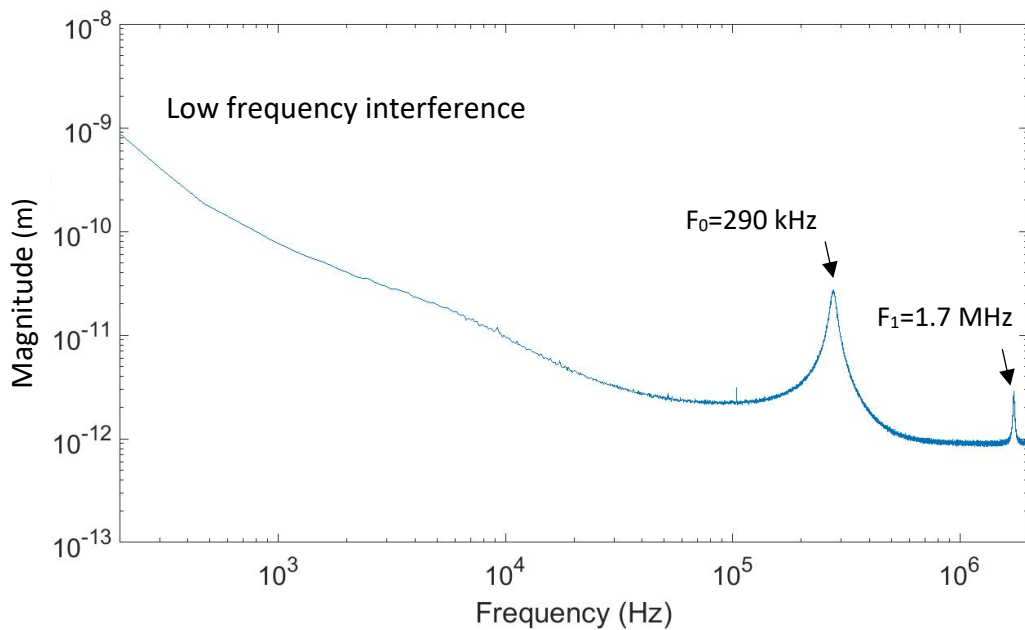


Figure 7.1.5 Plot of the frequency response of the thermal fluctuations of a $1 \mu\text{m} \times 65 \mu\text{m} \times 0.48 \mu\text{m}$ cantilever beam averaged 500 times.

From the averaged frequency spectrum plot in **Figure 7.1.5** we can see that although we have an improved signal to noise ratio as expected, low frequency interference still has the dominant magnitude in the signal. We can also see higher modes of vibration present in the frequency spectrum. This implies that although we have a greater signal to noise ratio, the system has become more underdamped.

Due to the time scales involved when capturing many frequency spectrum snapshots for averaging, the issue of drift also became apparent. The LDV laser spot is $1 \mu\text{m}$ in diameter, as is the width of the cantilever beams. In many cases, after 50 measurements or so, the cantilever had drifted away from the laser spot

destroying the measurement. When clamped more securely to the LDV stage, an increase in low frequency interference was apparent. In some cases, if the cantilever did not drift entirely away from the laser focal point by the end of the measurements, an increase in the noise floor of the measurement was observed.

7.2 Cantilever Thermal Response in Water

It is evident from the well-defined resonant peaks observed from the data captured from the devices that the cantilever's dynamic behaviour is underdamped. In order to induce dampening on the cantilevers such that they behave in an over-damped manner, the decision was made to attempt characterisation in water, and observe the dampening effects in an environment with a higher viscosity than air. This was done in order to have the thermal fluctuations of the free end of the cantilever resemble the over-damped response of a trapped particle system, such as the case in optical tweezers. The ideal frequency response of an optical trap is shown in **Figure 7.2.1** below [7.7].

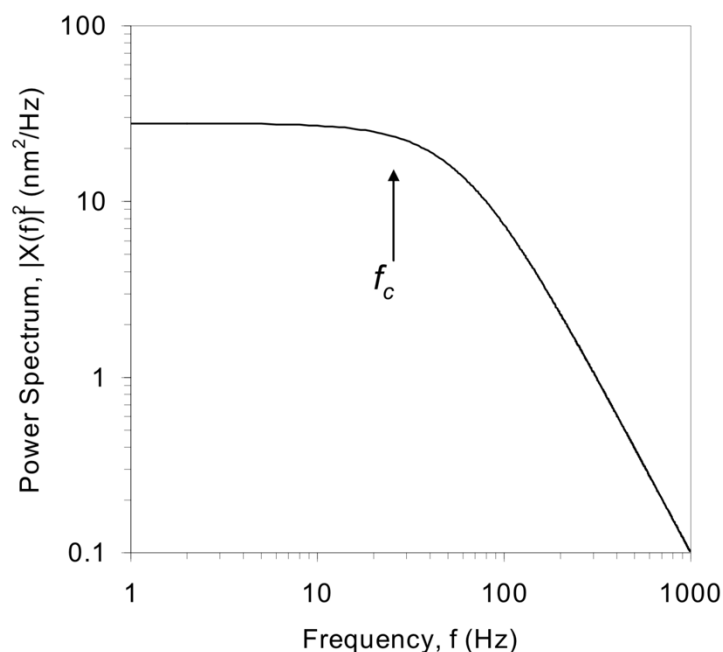


Figure 7.2.1 Ideal power spectrum of an optical trap showing overdamped frequency response. f_c is the characteristic frequency of the system [7.7].

A small holder was laser cut from plastic to hold the sample featuring the devices. The sample is placed in the centre of the holder and secured with superglue. The holder is then filled with de-ionised water and a cover slip placed over the surface to trap in the water around the sample, creating a chamber.

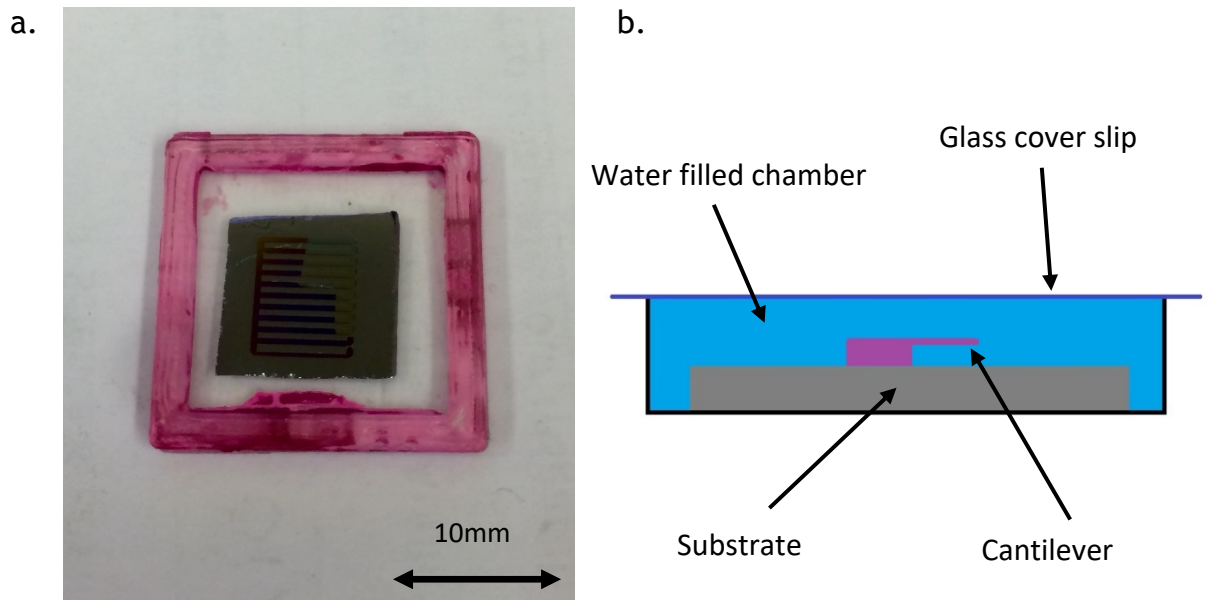


Figure 7.2.2 a & b Photograph of sample housed inside laser cut water chamber (a) and diagram showing cross section view of chamber set-up (b) (not to scale).

The sample holder is then placed on the LDV stage as described previously with the laser spot focussed through the glass cover slip onto the tip of the free end of the cantilever. Owing to increased scattering of the laser light in water and through the glass slide the magnitude of the reflected signal to the LDV detector is reduced. However, it was still possible to measure the thermal fluctuations of the cantilever beams submerged in water.

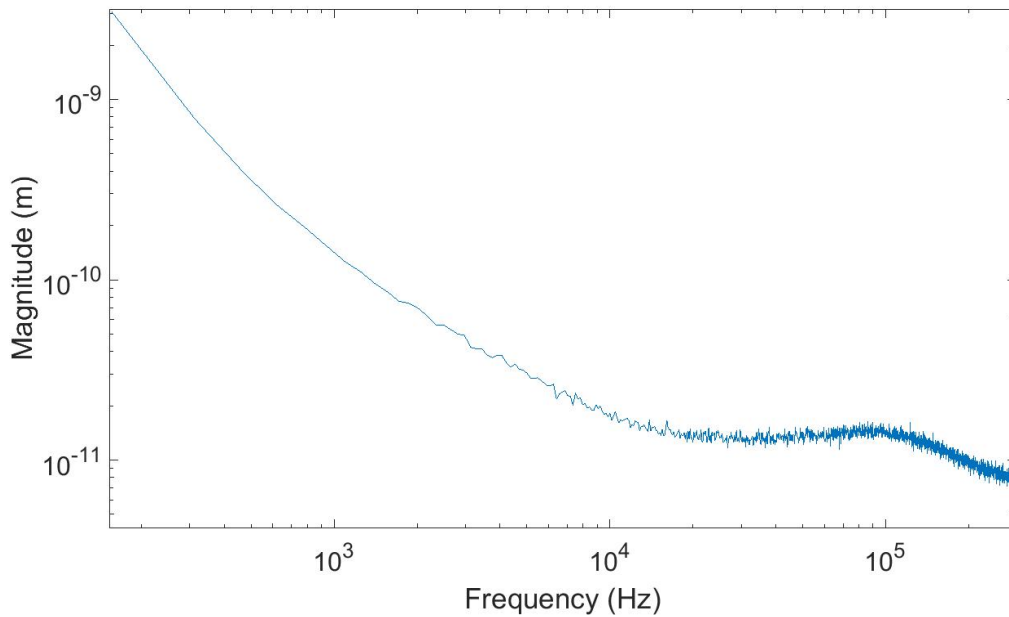


Figure 7.2.3 Plot of the frequency response of the thermal fluctuations of a $1 \mu\text{m} \times 40 \mu\text{m} \times 0.48 \mu\text{m}$ cantilever submerged in water averaged 100 times.

Figure 7.2.3 shows the frequency response of the thermal fluctuations of a $1 \mu\text{m} \times 40 \mu\text{m} \times 0.48 \mu\text{m}$ submerged in water averaged 100 times. The widening of the resonant peak (and hence reduced Q factor) shows significant dampening when compared to the cantilever response in air. **Figure 7.2.3** reveals that noise or interference at the low frequency still dominates the measurement. Normalising the NPAF in **Figure 7.2.4** was attempted using the RMS value acquired by the LDV software from the PSD of the cantilever submerged in water, but because the resonant peak lies within the low frequency interference range of the measurement it is not possible to attain an accurate measurement.

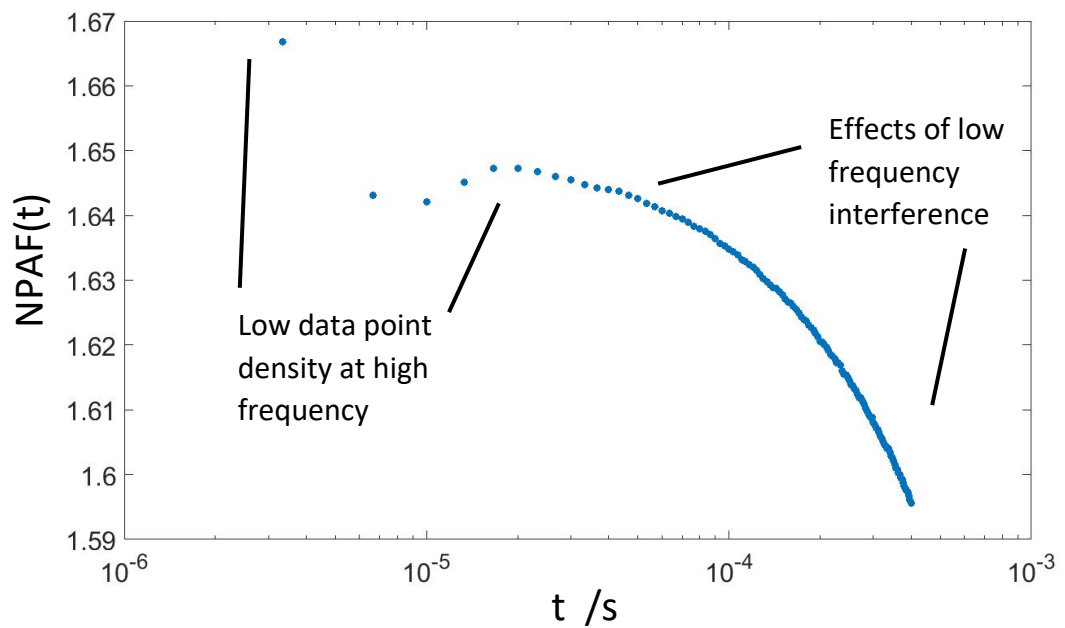


Figure 7.2.4 Normalised autocorrelation plot of the thermal fluctuations of a $1 \mu\text{m} \times 40 \mu\text{m} \times 0.48 \mu\text{m}$ cantilever submerged in water.

The plot shown in **Figure 7.2.4** is the normalised autocorrelation plot of the thermal fluctuations of a $1 \mu\text{m} \times 40 \mu\text{m} \times 0.48 \mu\text{m}$ cantilever submerged in water sampled at 300 kHz. This was chosen because it is the frequency at which the noise floor of the measurement starts to dominate the high frequency information. As a result of sampling at such a low frequency we find that the density of data points at short lag times in the NPAF is greatly reduced. It can also be seen at long lag times how the low frequency interference distorts the data and normalisation factor.

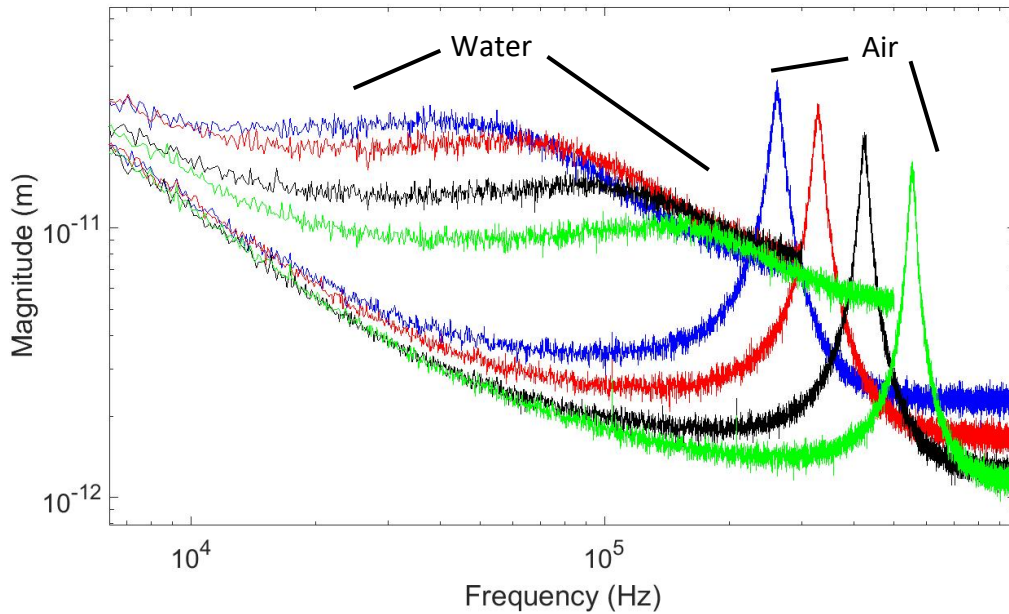


Figure 7.2.5 Plot of the thermal fluctuations in air & water of four cantilever beams. Width and thickness are uniformly $1\ \mu\text{m}$ & $0.48\ \mu\text{m}$, and lengths are $35\ \mu\text{m}$ (green), $40\ \mu\text{m}$ (black), $45\ \mu\text{m}$ (red) and $50\ \mu\text{m}$ (blue).

Figure 7.2.5 shows a summary of the frequency response of cantilevers from the initial fabricated device array measured both in air and water. This shows a reduction in oscillation amplitude for each cantilever when submerged in water, ranging from a $7\ \text{pm} \pm 0.3$ reduction for the $35\ \mu\text{m}$ cantilever to an $8\ \text{pm} \pm 0.3$ reduction for the $50\ \mu\text{m}$ cantilever. This reduced amplitude could be the result of the fluid being compressed by the high frequency oscillations and subsequently loading the surface of the cantilever, as described by Butt *et al* [7.8].

7.3 Reducing Cantilever Stiffness

It became clear at this point that the low signal to noise ratio of the measurements was considerably distorting the captured data. In order to further maximise the cantilever displacement to increase the SNR we would have to reduce the stiffness constant of the devices.

$$k = \frac{3EI}{L^3} \quad (2.1.1)$$

Equation 2.1.1 is the equation for the stiffness of a cantilever beam where E is the material's Young's modulus, L , the cantilever length and I the second moment of inertia for a rectangular cross section defined as

$$I = \frac{WH^3}{12} \quad (2.1.2)$$

Where W is the width of the cantilever and H is the height, or thickness. We can see from the above equations that the cantilever stiffness is dominated by 3 controllable factors: the stiffness is proportional to the width and thickness cubed and is inversely proportionally to length cubed. As the devices are at the lower limit of width in terms of the LDV laser spot diameter of 1 μm , the devices can be reduced in stiffness by having reduced height or increased length.

In order to minimise cantilever stiffness and therefore maximise displacement and SNR, two further strategies were employed. The first strategy was to try thinning the cantilevers further in order to reduce their stiffness. The initial cantilever arrays fabricated were around 480 nm thick, limited by the initial thickness of the diamond-on-silicon samples provided by our collaborator. The intent was to etch the entire surface of the diamond sample to reduce it in thickness before fabricating devices. The diamond etch process described earlier and used to define the cantilever structures was used for this purpose. Initial etching tests revealed that the surface of the diamond did not become significantly rougher over the first 100 nm or so. **Figure 7.3.1** shows an AFM scan of the surface of the sample at the etch wall after a two minute etch. The lower plateau is the etched region. Average values showed the roughness of the un-etched area to be 3 nm Ra and the roughness of the etched area 3.6 nm Ra.

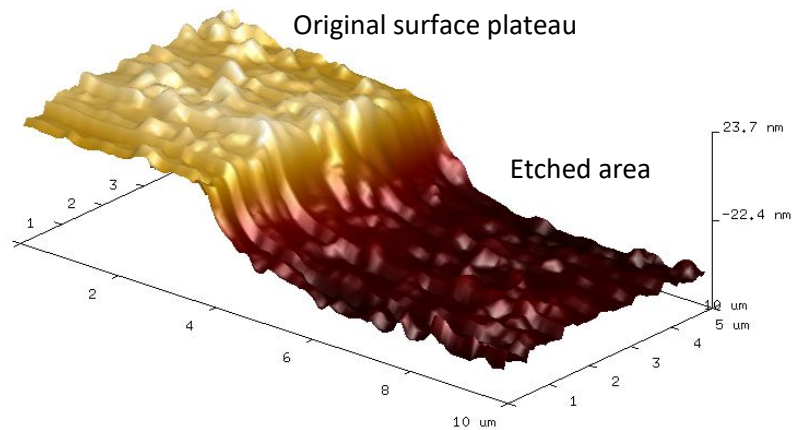


Figure 7.3.1 AFM scan of the diamond surface at etch wall. The lower plateau is the etched area.

However, the more diamond that was etched the rougher the surface became. After etching 150 nm the surface had become so rough that the AFM scan head would not engage. This roughness was possibly due to the etch rate varying with regards to grain boundaries and other structural defects in the diamond. Despite the roughening of the surface, it was still possible to pattern and etch the thinned diamond into cantilevers ready for release. **Figure 7.3.2** shows an optical image of the thinned substrate after patterning.

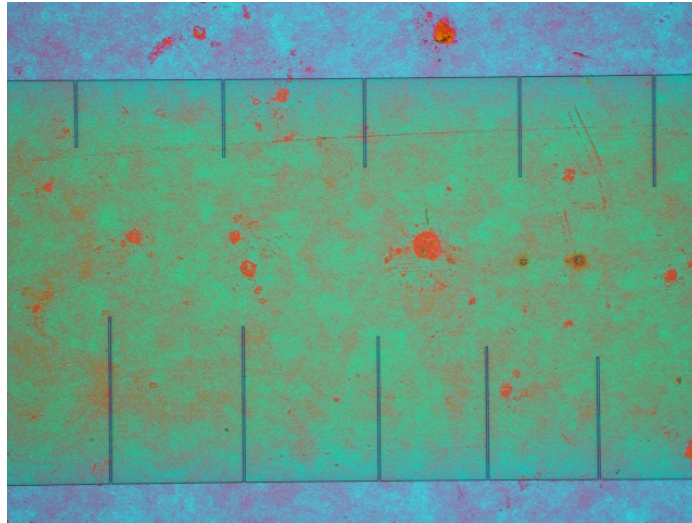


Figure 7.3.2 Optical inspection of cantilever patterning on thinned diamond substrate at 60 x magnification. Cantilever width 1 μm .

Upon inspecting the sample after the ICP silicon etching stage of the release process, it was found that the diamond had been completely removed from the silicon substrate during the process. It is thought that during the diamond thinning process the material had become mechanically compromised and the bonding between the diamond and silicon substrate unsecure. This could be attributed to the diamond and silicon substrate experiencing different thermal expansion during the thinning process.

Owing to the complex and time-consuming nature of dry etch process, development of a second approach for reducing cantilever stiffness was investigated. The second strategy employed was to fabricate cantilevers with increasing length in order to reduce stiffness. The limiting factors in producing long, high width/length aspect ratio cantilevers are twofold: with increasing length and reduced stiffness the cantilevers become increasingly fragile and may not survive the fabrication or characterisation process, and with increasing length there is a risk that the cantilevers will not fully release from the silicon substrate and become stuck to the silicon surface during the wet etch stage of the release process.

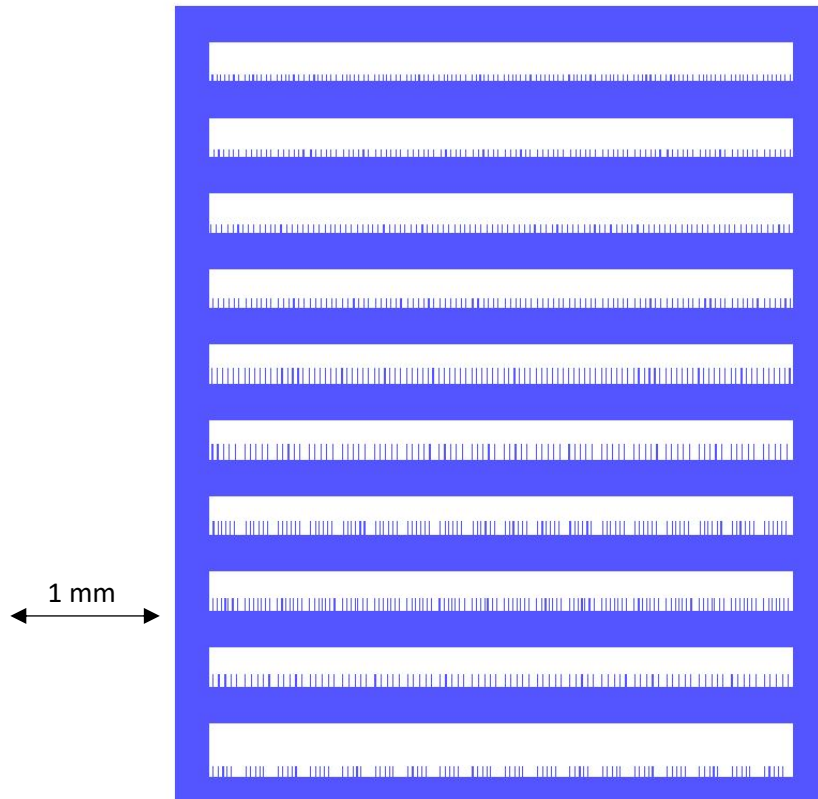


Figure 7.3.3 L-edit screen capture of cantilever arrays of varying length from 60 μm to 150 μm , showing increased number of devices in this design iteration.

Figure 7.3.3 shows the CAD design for the etch mask that forms cantilever arrays ranging in length from 60 μm to 150 μm . Significantly more cantilevers appear here in comparison to previous designs as low device yield was anticipated for longer devices. The fabrication process as described for previous devices was used with the exception of a longer final wet etch step to increase the clearance between the silicon substrate surface and the cantilevers.

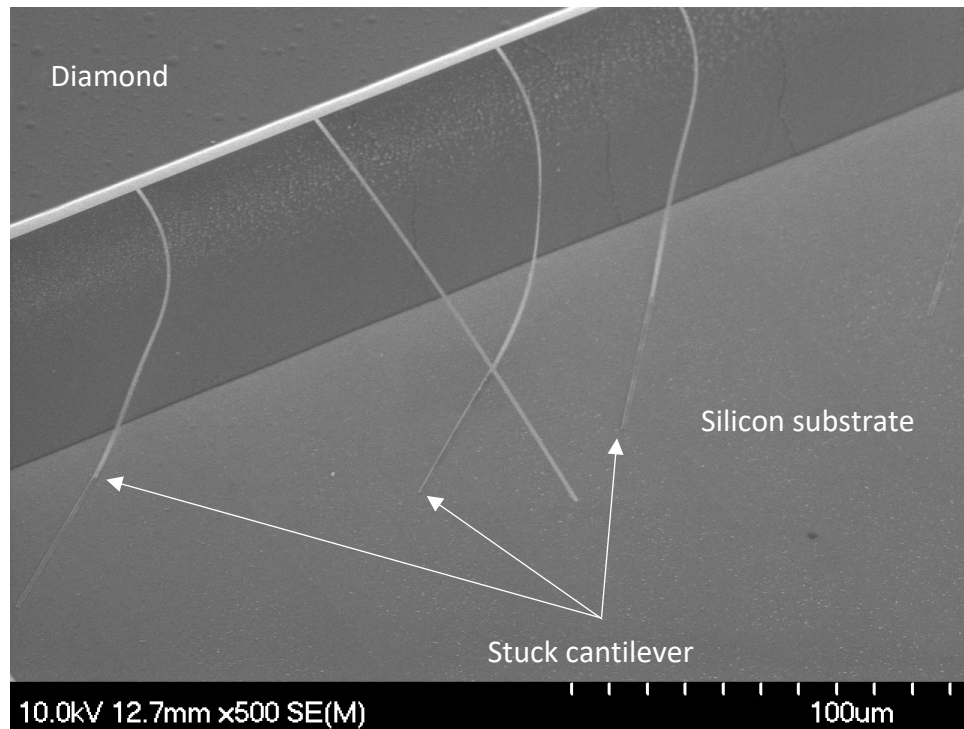


Figure 7.3.4 SEM image of a $1\ \mu\text{m} \times 110\ \mu\text{m} \times 0.4\ \mu\text{m}$ cantilever beam. Also visible are cantilevers stuck to the silicon substrate during the release process.

Despite a low yield ($< 10\%$ at longer cantilever lengths), cantilever devices up to $150\ \mu\text{m}$ in length were fabricated successfully. The majority of yield issues were due to cantilevers becoming stuck to the silicon surface during the wet etch release stage. Further silicon etching to increase the clearance of the cantilevers from the silicon surface would significantly increase the undercut at the base of the cantilevers. It is understood that these are the highest width/length aspect-ratio polycrystalline diamond cantilevers yet reported. Linzon *et al* reported a silicon device with dimensions $L = 500\ \mu\text{m}$, $W = 16\ \mu\text{m}$ and $H = 5\ \mu\text{m}$ [7.9]. Their designs were used to obtain large amplitude flexural vibrations using electrostatic forces to be used as mass sensors. Therefore, these devices could be of importance in applications relating to large amplitude vibrations. It was discovered after the initial diamond etch stage of the process for these devices that the PCD thin films are not uniformly thick across the entire wafer area. The diamond is thinner towards the wafer edges as a result of the CMP process. The thickness of the sample used to fabricate the longer cantilevers is $400\ \text{nm}$, $80\ \text{nm}$ thinner than the initial devices.

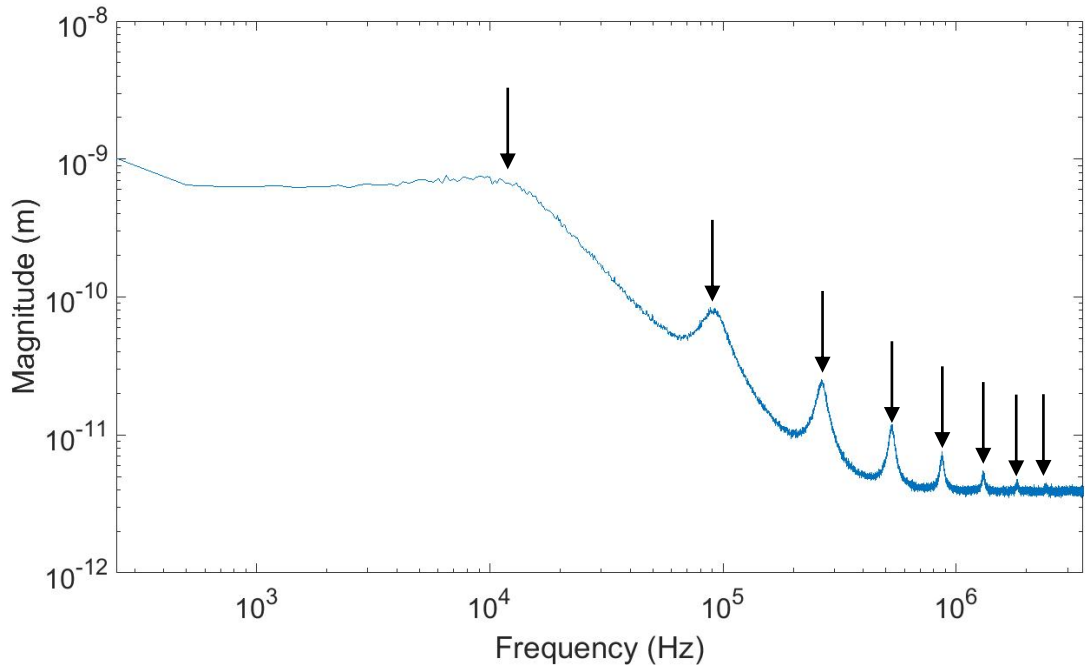


Figure 7.3.5 The frequency response of the thermal fluctuations of a $1\ \mu\text{m} \times 150\ \mu\text{m} \times 0.4\ \mu\text{m}$ cantilever in air averaged 250 times. Arrows indicate the 8 modes of vibration.

Figure 7.3.5 shows the frequency response of the thermal fluctuations of a $1\ \mu\text{m} \times 150\ \mu\text{m} \times 0.4\ \mu\text{m}$ cantilever in air averaged 250 times. The plot shows a slightly underdamped peak at around 40 kHz, and 7 higher modes of vibration, indicated by the black arrows. The first resonant peak, or knee, has displacement roughly equal to the magnitude of low frequency interference and the majority of the signal up to around 1 MHz is above the DANL of the measurement. The displacement is around 900 pm, more than an order of magnitude greater than the previously fabricated shorter cantilevers.

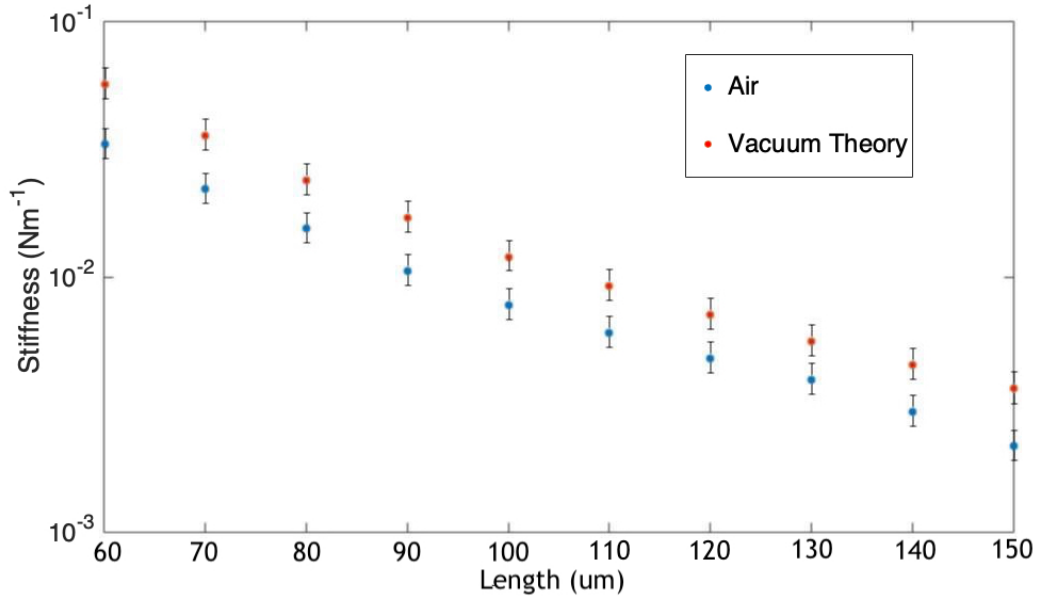


Figure 7.3.6 Plot of cantilever length v stiffness comparing measurements and theoretical values. Error bars show 90 % confidence interval corresponding to possible variation in the diamond material's Young' modulus and/or density. The fabricated cantilevers show a substantially uniform reduction in stiffness for each length measured.

Figure 7.3.6 compares the theoretical values in vacuum and measured values for cantilever stiffness in air as a function of cantilever length. The stiffness of fabricated cantilevers was calculated from the measured resonant frequency, geometry and mechanical properties of the devices. Slight variations in the trend of measured data can be attributed to undercut at the base of the cantilever changing its effective length. The measured values reveal a substantially uniform reduced stiffness owing to their reduced resonant frequency as a result of dampening in air.

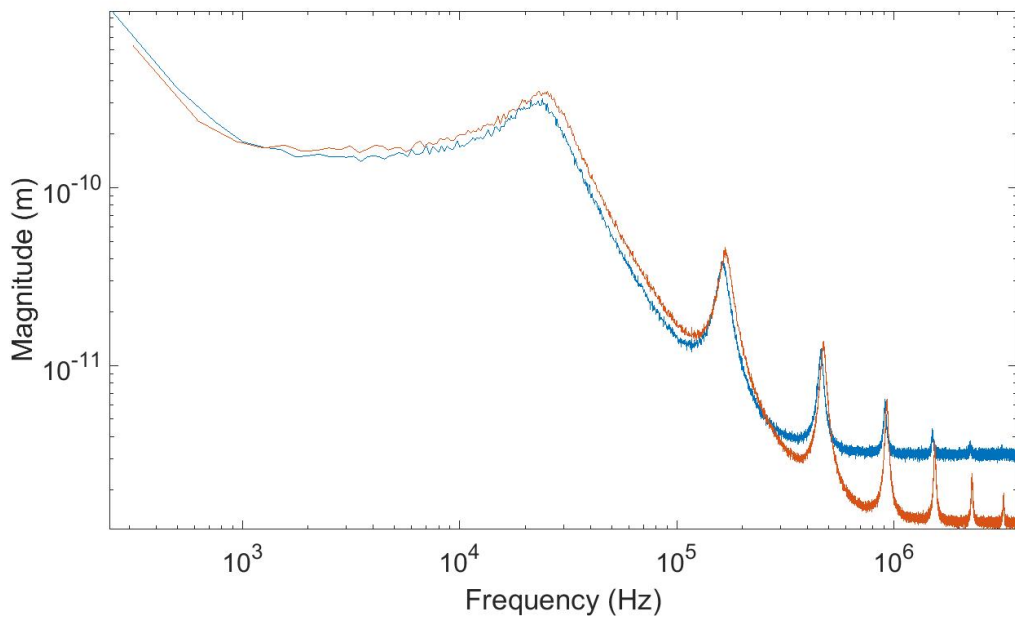


Figure 7.3.7 The frequency response of the thermal fluctuations of two $1\ \mu\text{m} \times 130\ \mu\text{m} \times 0.4\ \mu\text{m}$ cantilever in air averaged 250 times sampled at 10 MHz (red) and 7 MHz (blue). Difference in noise floor levels at high frequency are attributed to the different sample rates.

Figure 7.3.7 shows the frequency response of the thermal fluctuations of two $1\ \mu\text{m} \times 130\ \mu\text{m} \times 0.4\ \mu\text{m}$ cantilever in air averaged 250 times. This plot is an example of how the DANL changes with sampling frequency. The red plot has been sampled at 10 MHz and the blue plot sampled at 7 MHz. We can also see from this plot that even with a 1:130 aspect ratio cantilever the maximum cantilever displacement still does not exceed the magnitude of low frequency noise. Slight variations in frequency and magnitude at the resonant peaks can be attributed to measurement drift or variation in etching undercut at the cantilever base which increases the effective length of the cantilever.

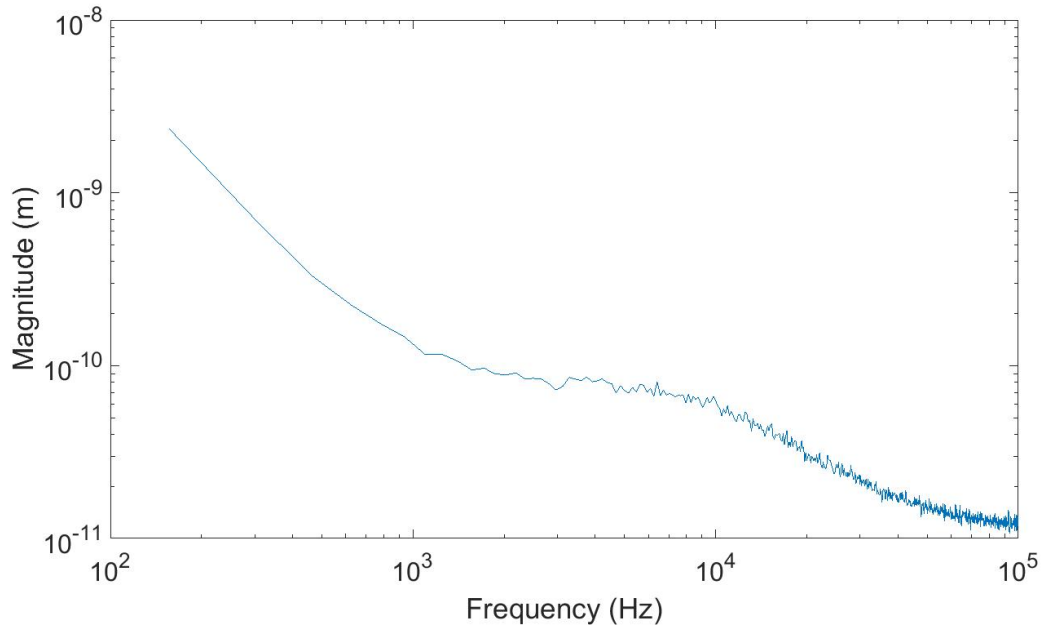


Figure 7.3.8 The frequency response of the thermal fluctuations of a 1 μm x 60 μm x 0.4 μm cantilever in water averaged 250 times.

Figure 7.3.8 shows the measured frequency response of a 1 μm x 60 μm x 0.4 μm cantilever submerged in water up to 100 kHz. As can be seen from the plot, the longer cantilever has increased displacement in water and the response of the cantilever is overdamped. Low frequency noise still dominates the measurement. Owing to limitations in the LDV software a maximum of 640 data points were available for this plot. This gives a frequency resolution of 156.25 Hz. This translates into a low density of high frequency data points in the corresponding NPAF of the data as can be seen in **Figure 7.3.10** below. Here we see an improvement in the amount of data points at high frequency when compared to the NPAF plot in **Figure 7.2.3** however there is still insufficient data resolution at short time lengths. Interference still dominates at low frequency and warps normalisation factors.

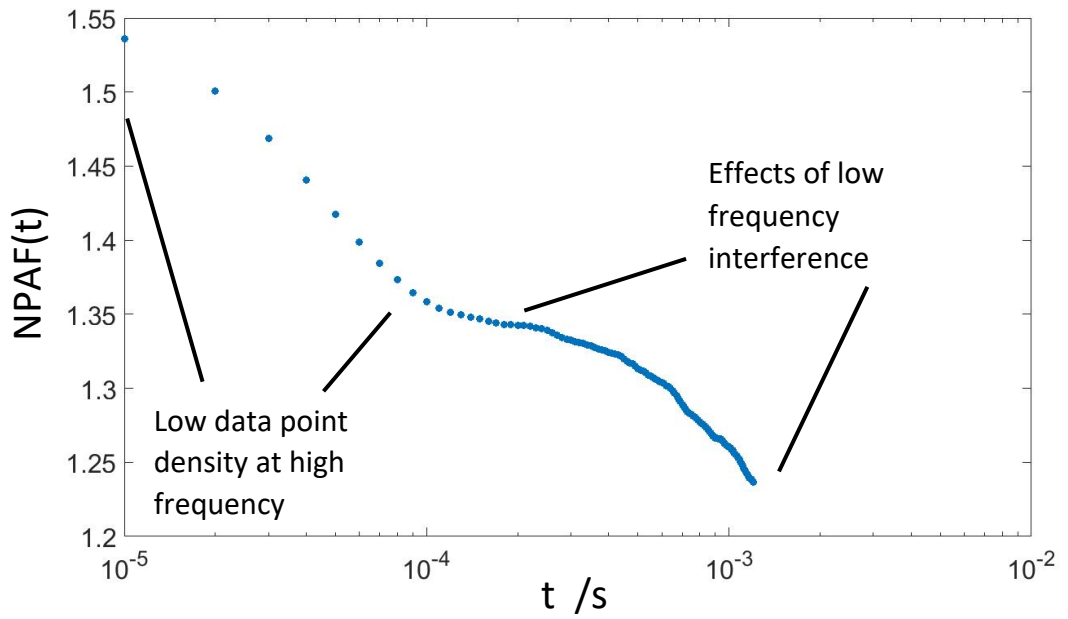


Figure 7.3.9 Normalised autocorrelation plot of the thermal fluctuations of a $1 \mu\text{m} \times 60 \mu\text{m} \times 0.48 \mu\text{m}$ cantilever submerged in water.

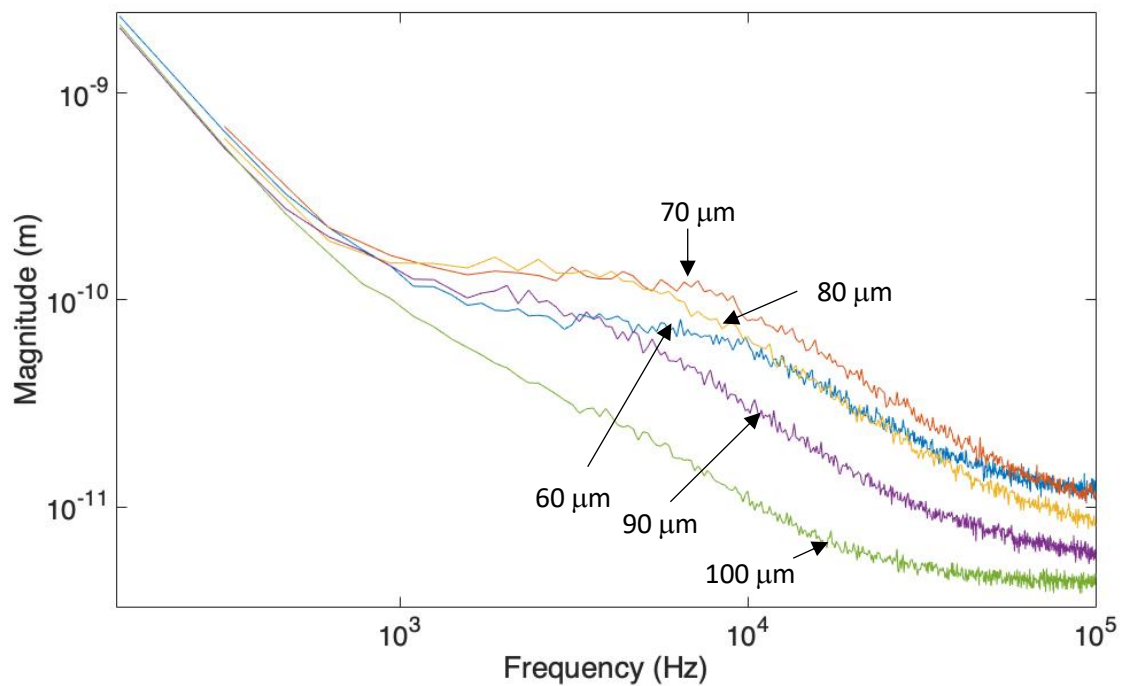


Figure 7.3.10 The frequency spectrum of thermal fluctuations in water for cantilever 60-100 μm in length. Blue: 60 μm , orange: 70 μm , yellow: 80 μm , purple: 90 μm and green: 100 μm .

Figure 7.3.10 shows the frequency response of five cantilevers ranging from 60 μm to 100 μm in length. The blue and red plots show the 60 μm and 70 μm long cantilevers respectively. It can be seen that the magnitude of displacement increases from the shorter to the longer beam as expected. The yellow, purple and green plots show the frequency response of the 80 μm , 90 μm and 100 μm beams respectively. We can see a reduction in magnitude in the cantilevers upwards in length from the 70 μm cantilever. This could be due to severe dampening by the surrounding fluid on the cantilevers, or alternatively this could be caused by destructive interference from low frequency noise, consuming the cantilever response. The noise floor at higher frequencies for all the longer cantilevers was visible from ~100-200 kHz and sample rates were set accordingly as not to capture this high frequency noise floor. As a result we have a low frequency resolution in these measurements and low data-point density for high frequency information in the corresponding NPAF plots for all the longer devices.

7.4 Device Summary

	Length (μm)	Width (μm)	Height (μm)	K (Nm^{-1})	F air (Hz)	Q air	F water (Hz)
Sample A	35	1	0.48	0.570	554700	30.6	148100
	40	1	0.48	0.380	424500	24.1	88750
	45	1	0.48	0.260	382300	19.7	60780
	50	1	0.48	0.220	261300	19.9	42030
Sample B	60	1	0.40	0.030	102800	4.40	*
	70	1	0.40	0.020	78280	3.72	*
	80	1	0.40	0.016	60940	3.57	*
	90	1	0.40	0.010	47660	3.31	*
	100	1	0.40	0.008	38750	2.20	*

Table 7.4.1 Summary of all PCD cantilever devices reported in this chapter that have had thermal response characteristics measured in air and water. Data pertaining to Q factor in water is absent as the figures were unobtainable from the captured data. The low frequency portion of the resonant peak was distorted by low frequency interference to the extent that the -3dB point was unresolvable. In water, above a length of 50 μm , the cantilever response becomes damped to the point that no resonant peak was resolvable and is marked on the table by *. Owing to the absence of a resonant peak, the Q factor in water for the devices marked * is assumed to be <1 .

7.5 Data Analysis Verification

In preparation for having captured raw data, an investigation into data analysis methods was undertaken. Based on the work of Tassieri *et al* [7.1], a MATLAB routine to evaluate the complex viscosity of a fluid surrounding a submerged cantilever was written. By using test data [7.10] provided by Dr Manlio Tassieri from the University of Glasgow captured from an optically trapped particle in water it was possible to verify the MATLAB routine. In addition to verifying the methods described by Tassieri *et al*, whereby the autocorrelation (or mean squared displacement) of a trapped particle is attained and normalised from the time series of the displacement signal, it was also possible to verify an alternative method by analysing the signal in the frequency domain. This is a method that better suits experimental constraints in terms of measurement length, as magnitude averaging in the frequency domain can be used as an alternative to long time measurements. To date, there has been no universal method presented to extract a fluid's viscoelastic properties from the power spectrum of the signal for either passive micro-cantilever or passive optical tweezer systems. Ongoing research elsewhere either utilises active devices, relies on building up a range of frequency data from several different measurements or frequency sweeps, or provides system specific solutions that may not yet be applied universally [7.11].

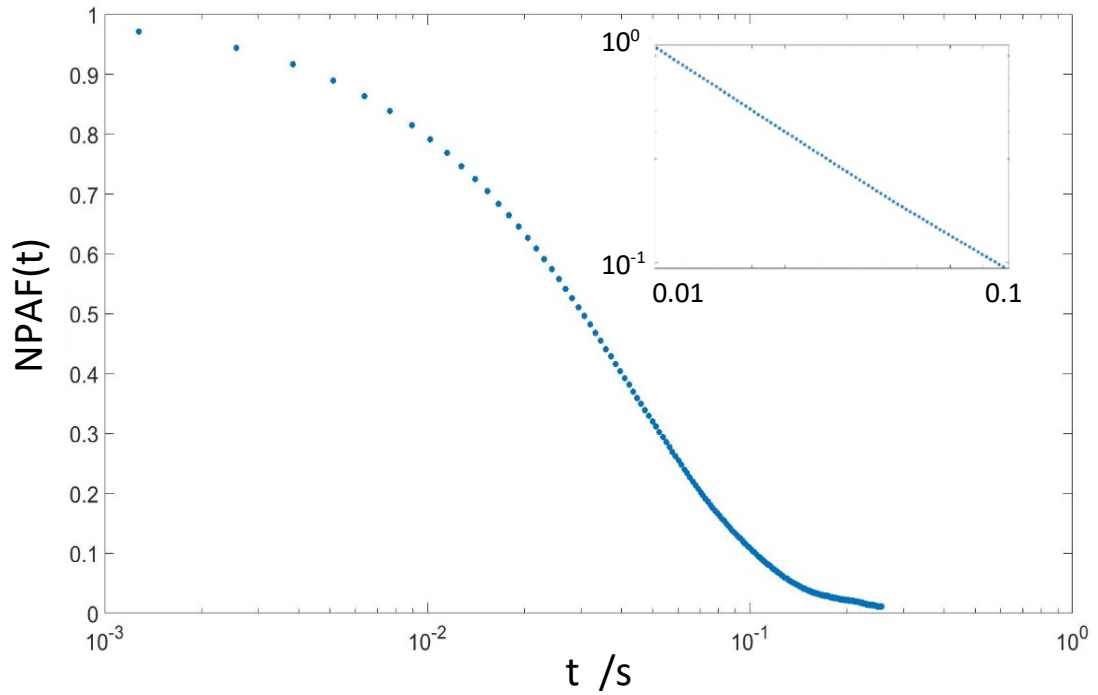


Figure 7.5.1 The log-linear plot (inset linear-log) of the normalised position autocorrelation function of an optically trapped particle in water, evaluated from the time series of the particle displacement. 770 Hz sample rate. Data provided by Dr Manlio Tassieri from the University of Glasgow.

Figure 7.5.1 shows the position autocorrelation function of a trapped particle in water sampled at 770 Hz, evaluated from a displacement/time data series. The plot has been normalised by the variance of the time signal. By plotting the same data on a linear-log axis as in **Figure 7.5.2** (inset) we see it is a straight line at short time scales, verifying that the NPAF has the form of a single decaying exponential.

Following the methods described by Tassieri *et al*, the complex modulus, $G^*(\omega)$, of the fluid surrounding the trapped particle can be evaluated by taking the Fourier transform of the autocorrelation function and applying the following relationship:

$$G^*(\omega) = \frac{k}{6\pi a} \cdot \frac{i\omega\hat{A}}{1 - i\omega\hat{A}} \quad (7.5.1)$$

Where \hat{A} is the Fourier transform of the autocorrelation, i is the imaginary unit and ω is angular frequency, k is the stiffness of the optical trap and a is the radius of the trapped particle.

From the complex modulus we can extract the complex viscosity η^* from their relationship in a Newtonian fluid:

$$\eta^* = \frac{G^*(\omega)}{i\omega} \quad (7.5.2)$$

As plotted in **Figure 7.5.3**. This yields a displayed average value for the viscosity of water as 9.04×10^{-4} Pa.s compared to the textbook value of 8.9×10^{-4} Pa.s, less than 1.7 % error. This error can be attributed to variation in the diameter of the trapped particle, with the manufacturer quoting a variation up to 10 %.

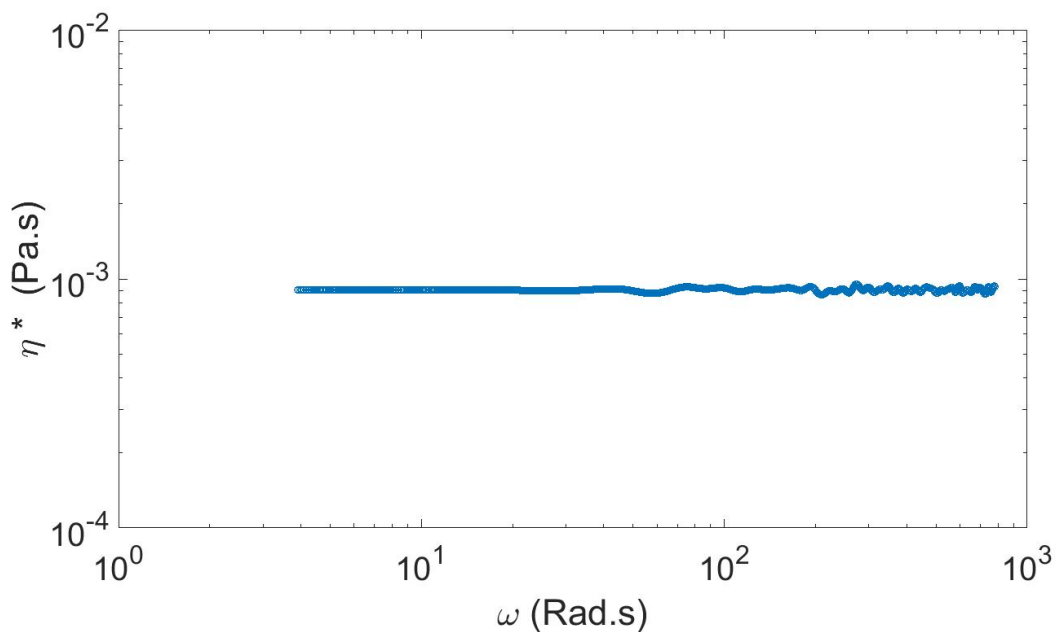


Figure 7.5.3 The complex viscosity of water evaluated from the time series of the position of an optically trapped particle. Data provided by Dr Manlio Tassieri from the University of Glasgow.

The above data analysis was achieved by calculating the autocorrelation of the position of a trapped particle in water from a time series of the particle's position. There now follows a method of evaluating and normalising the autocorrelation function from the frequency spectrum of the trapped particle's trajectories.

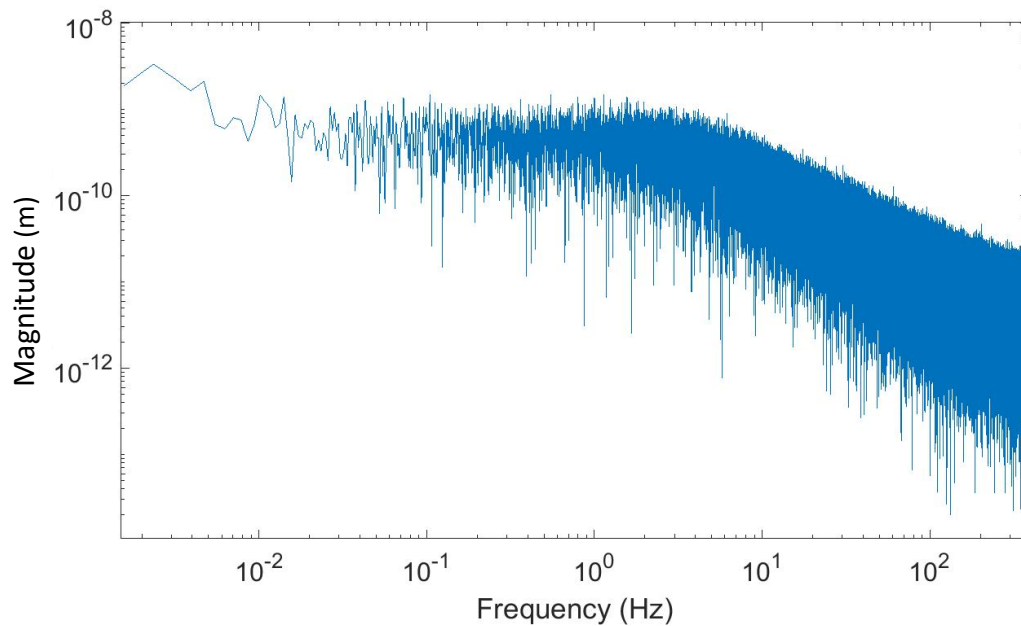


Figure 7.5.3 The frequency spectrum of an optically trapped particle in water. Data provided by Dr Manlio Tassieri from the University of Glasgow.

Figure 7.5.3 shows the frequency spectrum of an optically trapped particle in water. This plot was evaluated from the same time series data used to generate the plot in **Figure 7.5.1**. From the Wiener-Khinchin theorem it is known that the power spectral density (PSD) and the autocorrelation of a signal form a Fourier transform pair. By multiplying the Fourier transform of the time signal of the optically trapped particle in water by its complex conjugate we find its PSD, and the inverse Fourier transform (IFT) of the PSD reveals the autocorrelation of the signal. The RMS value of the signal is the square root of the total power in the PSD. In accordance with Parseval's theorem, the total power in the signal in the PSD is equal to the variance of the signal in the time domain. In the time series analysis performed previously, the autocorrelation function is normalised by the variance of the original time signal. Therefore, it should be possible to normalise the autocorrelation function by the total power in the PSD of the signal. Indeed, this is a method commonly used in correlation force spectroscopy and AFM calibration techniques [7.12], [7.13].

Figure 7.5.4 shows the normalised autocorrelation plot of a trapped particle in water evaluated from the frequency spectrum of the thermal fluctuation. To plot this data, the PSD of the signal in **Figure 7.5.3** is calculated by multiplying the signal by its complex conjugate, then the IFT of the PSD is then calculated and

normalised by the total power calculated from the area under the PSD plot. **Figure 7.5.5** shows the complex viscosity of water evaluated from **Equations 7.5.1 & 7.5.2**, using the normalised autocorrelation plot acquired from the power spectrum of the signal. The displayed average value in **Figure 7.5.5** is 9.04×10^{-4} Pa.s. This is the same value as shown in **Figure 7.5.3**, which is the data acquired from the original time series of the signal. This example shows that in the case of a Newtonian fluid it was possible to extract the fluid's complex viscosity from the frequency spectrum of a trapped particle's position. In principle this should also be a viable method for extracting the complex modulus and complex viscosity of non-Newtonian fluids.

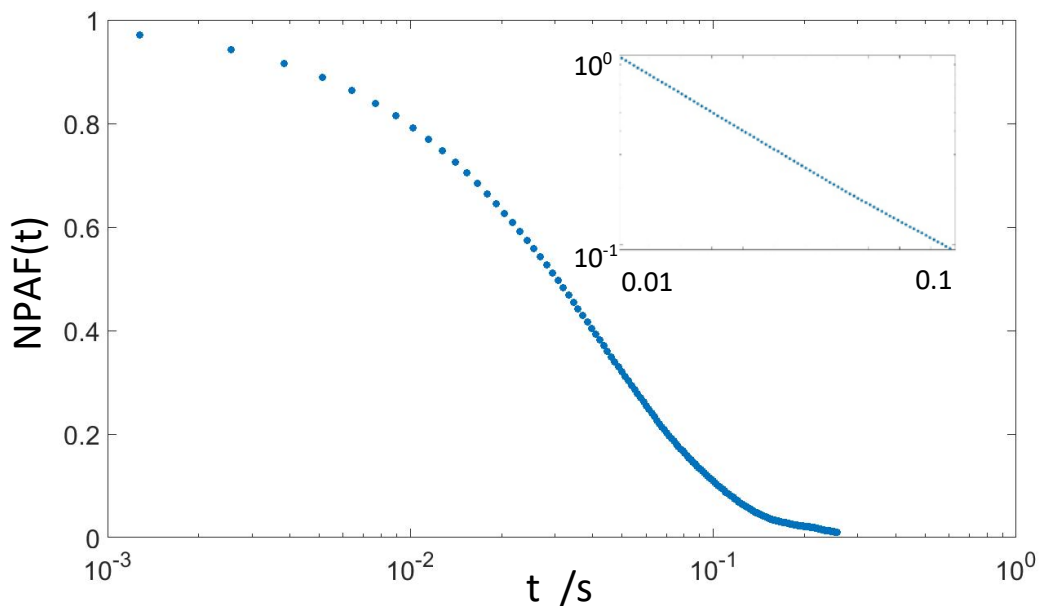


Figure 7.5.4 The log-linear plot (inset linear-log) of the normalised position autocorrelation function of an optically trapped particle in water, evaluated from the power spectrum of the particle displacement. 770 Hz sample rate. Data provided by Dr Manlio Tassieri from the University of Glasgow.

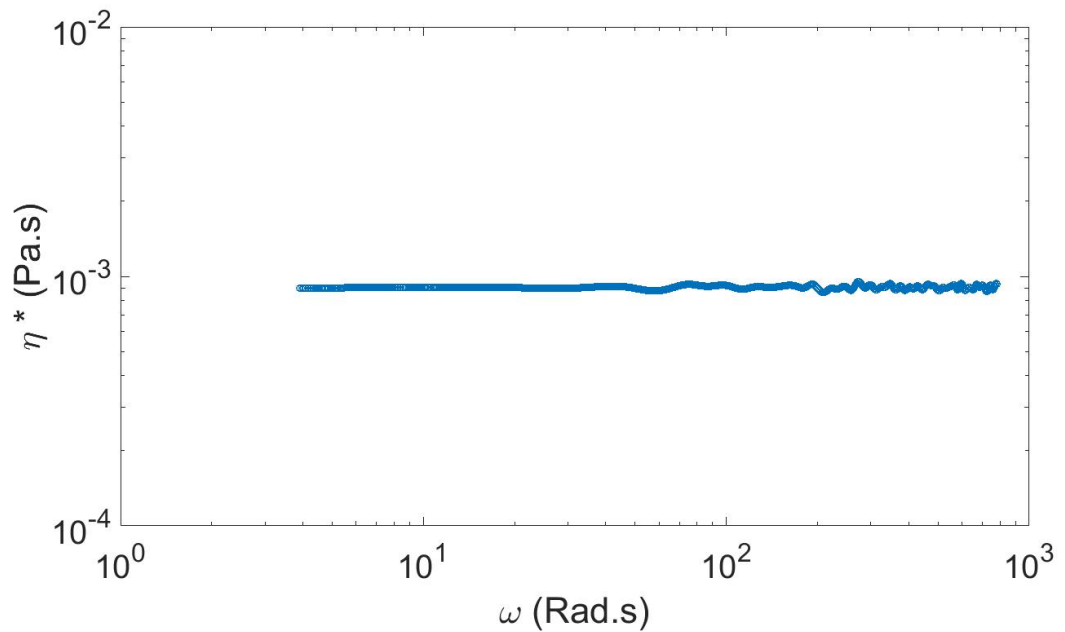


Figure 7.5.5 The complex viscosity of water evaluated from the power spectrum of an optically trapped particle. Data provided by Dr Manlio Tassieri from the University of Glasgow.

7.6 Chapter Summary

An extensive investigation into the viability of a PCD based device for micro-rheology has been presented. Using a variety of established manufacturing techniques and subsequent process development, micro-cantilevers were fabricated from PCD thin films on silicon with feature sizes ranging from $0.4\mu\text{m}$ to $150\mu\text{m}$. The thermal fluctuations of these devices were measured using an LDV system. Owing to the underdamped dynamic response of the cantilevers in air, further measurements of the thermal fluctuation in water were taken to induce a damped system?. Attempts were made to plot the autocorrelation of the thermal fluctuations of these devices from the time series and frequency spectrum of their displacement. The limiting factors in these measurements were the noise floor of the LDV system and the SNR of the thermal fluctuations.

Devices with a lower stiffness constant and hence greater thermal fluctuation magnitudes were fabricated, however, the noise present in the LDV system was still the limiting factor in calibrating the devices in addition to low frequency resolution available at low sample rates. Some silicon etching process development has been reported in relation to fabricating free standing cantilevers with minimal undercut. In the absence of useable raw data, some test data from an optically trapped particle in water was used to verify and expand on pre-existing data analysis methods. The limitations of the methods presented are apparent based on the results reported, however, this body of work covers necessary research that will be valuable for future investigations. The latter devices fabricated exhibit over-damped harmonic behaviour when submerged in water: the limiting factor was noise coupled related with the measurement system. Therefore, it is entirely feasible that these devices (or similar) will yield positive results with an improved measurement system and as such would be research worth continuing.

References

- [7.1] M. Tassieri and P. S. Publishing, *Microrheology with Optical Tweezers: Principles and Applications*. Pan Stanford Publishing, 2016.
- [7.2] V. Kara, "Nano fluidics of Single-Crystal Diamond Nanomechanical Resonators," *Nano Letters*, 15 (12), pp 8070-8076 2015.
- [7.3] Y. E. Kuzovlev, "Why nature needs $1/f$ noise," *Physics-Uspexhi*, vol. 58, no. 7, pp. 719-729, 2015.
- [7.4] S. J. Rothberg and B. J. Halkon, "Laser vibrometry meets laser speckle," vol. 44, no. 0, p. 280, 2004.
- [7.5] M. W. Sracic and M. S. Allen, "Experimental Investigation of the Effect of Speckle Noise on Continuous Scan Laser Doppler Vibrometer Measurements," *Proc. Int. Modal Anal. Conf. - IMAC*, no. Ldv, 2009.
- [7.6] L. Cohen, "Generalization of the Wiener-Khinchin Theorem," *IEEE Signal Process. Lett.*, vol. 5, no. 11, pp. 292-294, 1998.

- [7.7] E. Lugo, R. Doti, J. Faubert, N. Sanchez, "Increasing light-induced forces with photonic crystals," *SPIENewsroom* February 2015.
- [7.8] H. Butt, P. Siedle, K. Seifert, K. Fendler, T. Seeger, E. Bamberg, and A. L. Weisenhorn, "Scan speed limit in atomic force microscopy," *Journal of Microscopy*, vol. 169, pp. 75-84, 1992.
- [7.9] Y. Linzon, "Efficient parametric excitation of silicon-on-insulator microcantilever beams by fringing electrostatic fields" *Journal of Applied Physics* 113, 2013.
- [7.10] <http://dx.doi.org/10.5525/gla.researchdata.827>
- [7.11] K. Nishi, M. L. Kilfoil, C. F. Schmidt, and F. C. MacKintosh, "A symmetrical method to obtain shear moduli from microrheology," pp. 1-8, 2016.
- [7.12] B. Robbins, "Rheology of fluids measured by correlation force spectroscopy," no. April 2014, 2012.
- [7.13] I. Popa, P. Kosuri, J. Alegre-Cebollada, S. Garcia-Manyes, and J. M. Fernandez, "Force dependency of biochemical reactions measured by single-molecule force-clamp spectroscopy," *Nat. Protoc.*, vol. 8, no. 7, pp. 1261-1276, 2013.

Chapter 8: Device Characterisation Results II

The forthcoming chapter details characterisation of boron-doped PCD micro-cantilevers, the fabrication of which is presented in **Sub-Chapters 6.2-6.4**. The deflection sensitivity of the devices is reported, followed by a discussion of the nature of the piezoresistive effect within the structure of the devices. Possible sources of error are identified and investigated.

8.1 Characterising Piezoresistive Cantilevers

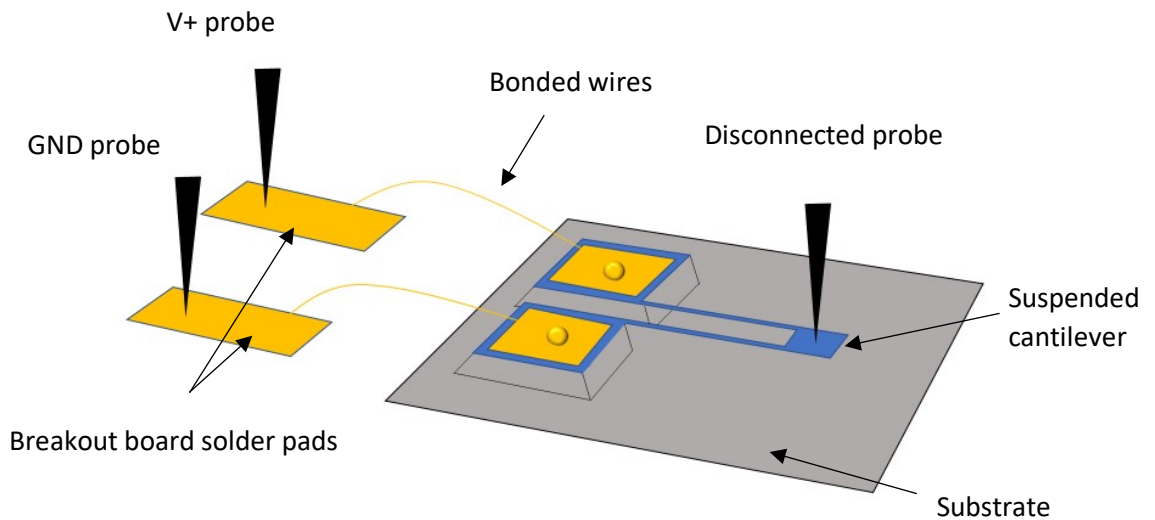


Figure 8.1.1 Schematic diagram showing components for characterising the piezoresistive effect in boron doped diamond cantilevers. Current is monitored through the V+ and GND probes as the disconnected probe is used to deflect the beam.

Figure 8.1.1 shows the experimental setup for observing the piezoresistive effect of the fabricated micro-cantilevers. An Agilent B1500 semiconductor parameter analyser is used to monitor the current through the cantilever beams. By applying two probes across the cantilevers via the solder pads on the breakout board, a voltage can be applied across the cantilever. The probe station then monitors the current through the network. A third probe is used to deflect the cantilever as the current is logged by the probe station. The position of the probes is controlled by a micro-manipulator. The maximum travel in the X, Y and Z directions are 250 μm and the controls are divided into 10 μm increments. By calibrating the manipulators against a device feature of known dimensions it is estimated that Z control can be manipulated with some accuracy by 5 \pm 1 μm increments. Monitoring the current over time as the cantilevers are displaced and applying ohm's law we can calculate the resistance change of the cantilever for each increment of Z deflection.

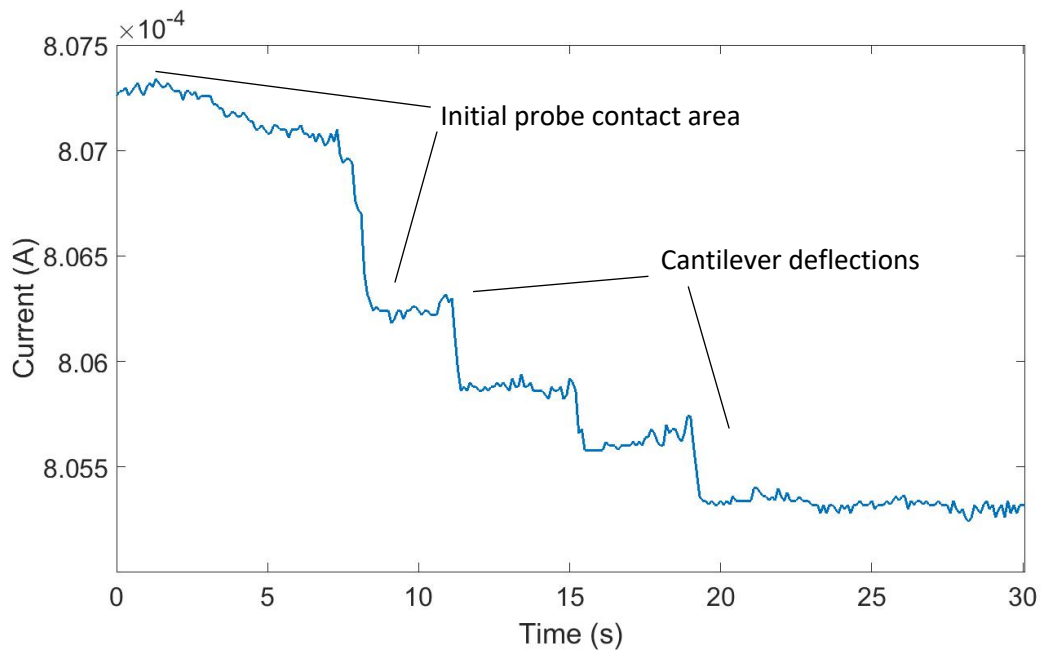


Figure 8.1.2 Plot of current vs time for cantilever C at four deflection increments.

Figure 8.1.2 shows the plot of current vs time for cantilever C as it is deflected by four increments. At short time scales when the cantilever is initially loaded by the deflecting probe there is an uncertainty relating to when the probe first makes actual contact with the cantilever tip. As this is monitored visually from above the cantilever it is impossible to determine the exact moment deflection begins in relation to the micro-positioner controls. Henceforth, the data used for further analysis is taken from the second deflection increment onwards, where the error in deflection can be minimised. From reviewing data published elsewhere we can expect the change in resistance for a given deflection distance to be linear, so it should be possible to extract the deflection sensitivity starting from any deflection increment [8.1]. The deflection sensitivity of the cantilever is given by:

$$S = \frac{\Delta R}{R} \frac{1}{\delta} \quad (8.1.1)$$

Where: ΔR and R are the change in resistance and initial resistance respectively, and δ is the cantilever deflection distance.

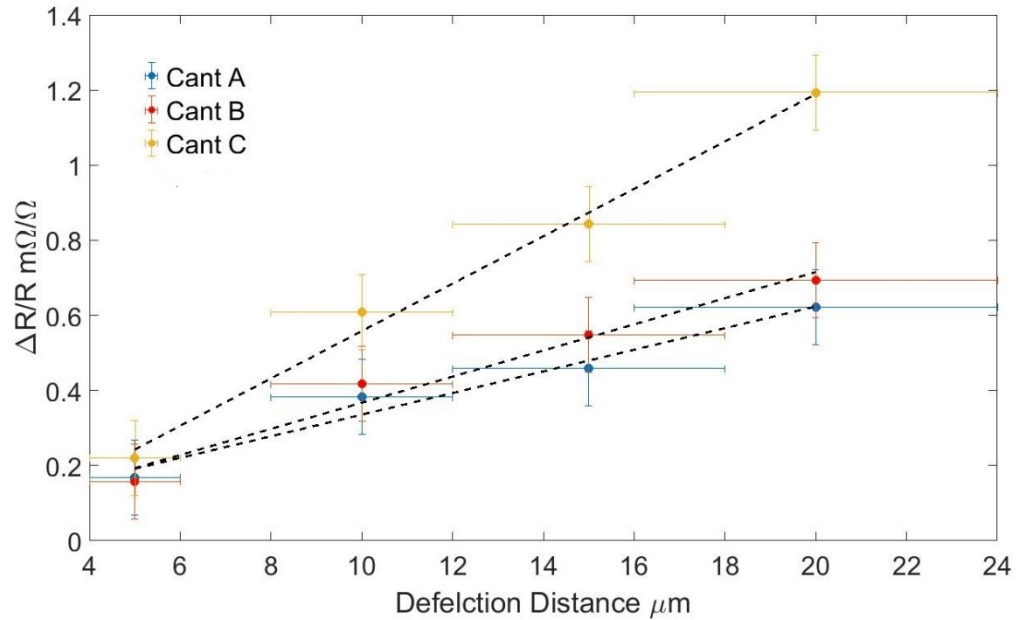


Figure 8.1.3 $\Delta R/R$ vs cantilever displacement for Cantilever A (blue) $l = 112 \mu\text{m}$, Cantilever B (red) $l = 96 \mu\text{m}$, and Cantilever C (yellow) $l = 62 \mu\text{m}$. X-data error bars correspond to a 75 % confidence interval ($\pm 1 \mu\text{m}$ per measurement, accumulative). Y-data error bars correspond to 90 % confidence interval.

Figure 8.1.3 shows $\Delta R/R$ vs cantilever displacement for cantilevers A, B and C. To calculate $\Delta R/R$, the average current value at each deflection interval is taken and divided by the applied voltage, which was kept constant at 1V across all measurements. From the linear fit to the data we find the deflection sensitivity for the cantilevers to be $S_A = 0.029 \text{ m}\Omega/\Omega\text{-}\mu\text{m}$, $S_B = 0.035 \text{ m}\Omega/\Omega\text{-}\mu\text{m}$ and $S_C = 0.063 \text{ m}\Omega/\Omega\text{-}\mu\text{m}$. This is notably lower than other comparable devices in literature, with Privorotskaya *et al* reporting up to $0.186 \text{ m}\Omega/\Omega\text{-}\mu\text{m}$ for an $l = 309 \mu\text{m}$ device, and only as low as $0.062 \text{ m}\Omega/\Omega\text{-}\mu\text{m}$ for an $l = 411 \mu\text{m}$ device [8.2]. As the accumulative deflection error becomes larger it is not possible to definitively extrapolate whether the deflection sensitivity is linear or not for these devices. As expected, however, we note a general trend of higher deflection sensitivity as the cantilevers decrease in length.

8.2 Nature of Piezoresistivity in Cantilevers

Consider a rectangular cross section cantilever beam made from a homogenous material subject to deflection from a point load in the Z direction, as shown in **Figure 8.2.1** below. The cantilever will experience tensile stress on the top surface of the beam and compressive stress on the bottom surface of the beam. For a homogenous material the tensile and compressive stress will be equal with the cantilever experiencing zero stress at the neutral axis positioned at the centre of the beam.

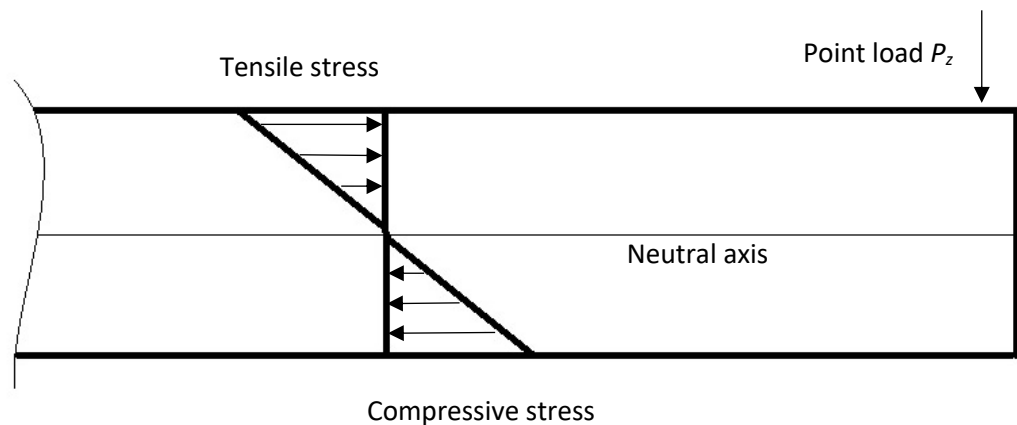


Figure 8.2.1 Stress distribution in rectangular cross section cantilever beam made from homogenous material.

Now consider the same cantilever beam but made from a piezoresistive material. We can model the resistivity of the cantilever as two parallel resistors R_1 and R_2 as shown in **Figure 8.2.2**. We find that for the same point load there is an increase in resistivity from the neutral axis to the top surface of the cantilever and a decrease in resistivity from the neutral axis to the bottom surface of the cantilever. In a purely homogenous material, ΔR_1 and ΔR_2 would be equal in magnitude and the net resistance change, ΔR_{total} would be equal to 0.

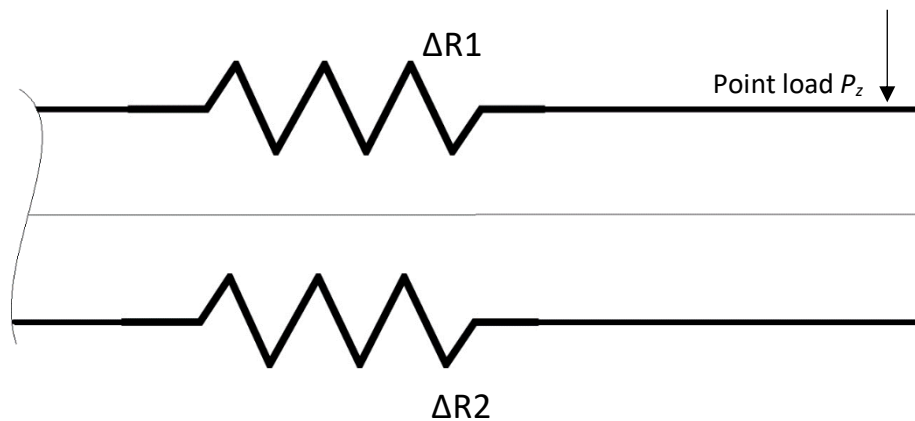


Figure 8.2.2 equivalent resistor network of homogenous piezoresistive cantilever beam.

We find, however, in cantilevers A, B and C that this is not the case. From deflecting the cantilevers, we find a net increase in resistance. In an attempt to explain this observation, we must look at the polycrystalline nature of the diamond material.

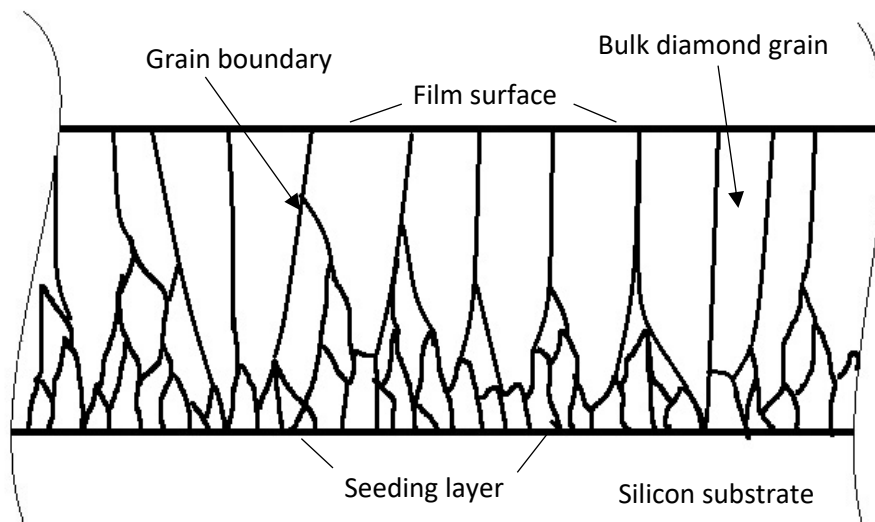


Figure 8.2.3 Cross sectional diagram of diamond thin film showing grain structure.

Figure 8.2.3 shows a cross sectional diagram of a polycrystalline diamond thin film. Throughout the thickness of the film the diamond grain growth is isotropic. The seeding layer of the diamond has a much higher content of non-diamond carbon which is also seen at the grain boundaries.

This uneven distribution of grain boundaries, crystal orientation and non-diamond carbon content leads to non-linear mechanical and electrical properties through the thickness of the film.

The nonlinearity of the mechanical and electrical properties of polycrystalline materials has been investigated extensively elsewhere and is subject to continued research across academia with many contradictory reports. Several possible contributing factors to the non-linearity of the piezoelectric effect in the devices in this study are brought to light by reviewing relevant literature; concerning the electrical properties of the polycrystalline film, it has been reported that the resistivity of a polycrystalline material changes with film thickness owing to several mechanisms [8.3]. One possible mechanism is charge scattering at grain boundaries. The seeding layer of the polycrystalline film has more grain boundaries which make it subject to higher resistivity when compared to the bulk-grain dominated thicker layers. In addition to this, it has also been reported that the piezoresistive effect is higher in single grains, and is reduced with the presence of grain boundaries [8.4]. With regards to mechanical properties, polycrystalline thin films have been shown to have a non-linear distribution of Young's modulus throughout the thickness of the film. Polycrystalline material experiences complicated microstructure effects caused by non-linear crystal alignment. In general, with increasing grain size throughout the film an increase in Young's modulus is observed [8.5], [8.6].

In strain gauges we find that the resistance change is a function of not only the change in resistivity but also includes a geometric factor derived from the material's Poisson's ratio, ν . For a strain gauge made from a homogenous material we find the relationship;

$$\frac{\Delta R}{R} = (1 + 2\nu)\varepsilon + \frac{\Delta\rho}{\rho} \quad (8.2.1)$$

Where ε is the strain applied and ρ is the material resistivity. In practice, a strain gauge would be located in an area of the deflecting structure that experiences maximum tensile or compressive stress. As such, the strain gauge only experiences the compression or tension coupled to it from the surface of the structure.

The polycrystalline cantilevers experience compressive and tensile stress simultaneously and thus cannot be considered strain gauges in the conventional sense. Without knowing the stress distribution through the cantilevers, it is not possible to determine the geometric contribution to the observed resistance change, however, it must be considered as contributing to the net result observed.

Consequently, the piezoresistive effect observed in cantilevers A, B & C is reasoned to be attributed to the net result of one or more of the above phenomena, with the possibility that one or more of the mechanisms described could be destructively interfering with one-another.

8.3 Contact Deformation in Undercut Area

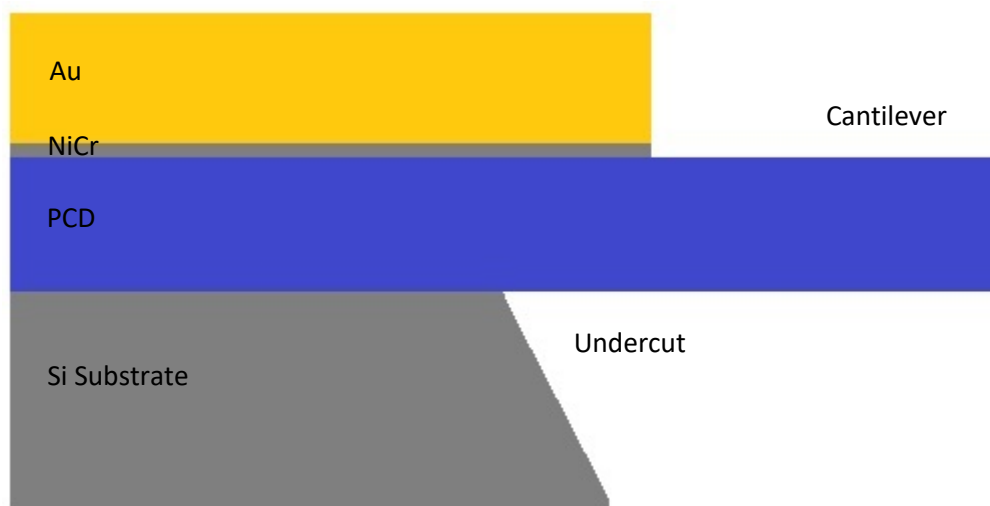


Figure 8.3.1 Cross sectional diagram of cantilever device showing undercut extending below the metal contacts.

Figure 8.3.1 shows a cross section schematic of the cantilever devices. It became apparent after fabrication that the undercut from the release etch extends under the metal contacts on the surface of the diamond film. NiCr (and Au to a lesser extent) is known to exhibit piezoresistive behaviour. Owing to the large undercut a portion of the metal contact is likely to be subject to mechanical deformation as the cantilevers are deflected. In an attempt to quantify any possible contribution to the net resistance change of the devices by contact deformation a simplified numerical analysis assuming worst case scenario conditions is investigated.

Consider cantilever A. If we assume cantilever A to be firmly base clamped, we can use the cantilever deflection formula as defined in **Chapter 2** to find that it takes a point load of 9.7 mN to deflect the beam tip by 20 μm . Now consider the undercut area under the contacts. This area can be modelled as triangular cantilever beam, the free end of which is the area where the cantilever is originally clamped (**Figure 8.3.2**). By extending the original length of the cantilever by adding the maximum undercut length and finding the deflection at the original base position when applying the same point load, an overestimated maximum value for deflection at the base of the undercut cantilever can be calculated. By using beam deflection formula described in **Chapter 2** the estimated maximum deflection at the theoretical free end of the triangular cantilever is 10 μm . In reality the value of deflection at this point would be much less as a result of the omitted material surrounding the cantilever legs resisting deformation.

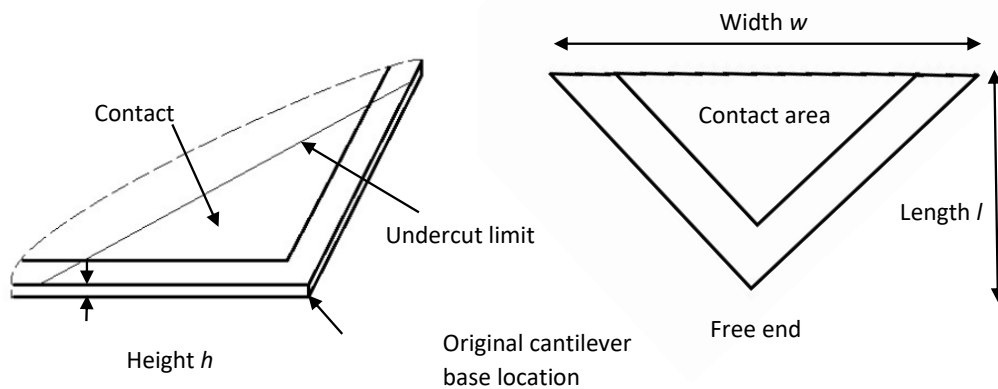


Figure 8.3.2 Undercut area modelled as triangular cantilever beam.

By taking the calculated value for maximum deflection we can calculate the maximum stress, and hence strain, on the contact. The strain is at maximum at the base of the triangular cantilever beam. The force, P required to displace a triangular cantilever beam by δ is given by:

$$P = \frac{2EI\delta}{L^3} \quad (8.3.1)$$

Where l is the cantilever length, E is the material Young's modulus and I the second moment of inertia for a rectangular cross section. The corresponding bending stress is given by:

$$\sigma = \frac{6 P L}{BH^3} \quad (8.3.2)$$

The relationship between stress and strain as provided by Hooke's law is:

$$\varepsilon = E \sigma \quad (8.3.3)$$

We can now relate the theoretical strain ε exerted on the NiCr contact to the potential change in its resistance ΔR and its gauge factor G by the relationship:

$$\Delta R = R G \varepsilon \quad (8.3.4)$$

Where R is the initial resistance of the NiCr. From the textbook value for the resistivity of NiCr and the dimensions of the contact area we find the theoretical resistance of the undercut portion of the NiCr layer to be $12 \mu\Omega$. From **Equations 8.3.2 & 8.3.3** we find the strain on the NiCr film at maximum end deflection to be 0.0048. From **Equation 8.3.4** and using a gauge factor of 2 for NiCr [8.7], this corresponds to a ΔR in the NiCr layer of $0.12 \mu\Omega$. As the contact resistance is dominated by the resistance between the NiCr layer and the diamond film and not the resistance of the contact metal, it can be reasoned that such a small percentage change in the resistance of the contact metal will have a relatively

small effect on the resistance of the entire network. The net change in resistance change in the network observed by deflecting cantilever beam A is 1.487Ω , which is many orders of magnitude larger than the worst-case scenario resistance change in the contacts. Therefore, it is reasonable to deduce that the piezoresistive effect observed can be attributed to deformation within the diamond cantilever.

8.4 Chapter Summary

An investigation into the piezoresistive properties of boron doped polycrystalline diamond was undertaken. Boron-doped samples supplied by an external collaborator were electrically characterised by TLM analysis. Titanium and Nichrome metals were investigated as potential adhesion layers for metal contacts. Time stability measurements on fabricated boron doped diamond micro-wires were performed and showed the material to be electrically stable for up to 60 seconds for various I/V measurements. After some process development, a process was established for fabricating suspended micro-cantilevers featuring metal contacts. Micro-cantilevers were fabricated from boron doped diamond thin films and the deflection sensitivity of these cantilevers is reported. The deflection sensitivity of the devices is likely to be significantly impaired by various described mechanical and electronic mechanisms in the polycrystalline material working against one-another reducing the net piezoresistive effect. The nature of the piezoresistive effect in the fabricated devices has been questioned and investigated, and possible sources of error in measurements and devices have been scrutinized. The possible error contribution of contact deformation resulting from etching undercut extending beneath the contacts has been explored.

References

- [8.1] U. Diamond, J. A. Carlisle, N. L. Privorotskaya, H. Zeng, S. Member, J. A. Carlisle, R. Bashir, and W. P. King, "Piezoresistive Microcantilevers From Piezoresistive Microcantilevers From Ultrananocrystalline Diamond," *Journal of MEMS*, Vol 15, no. 5, 2010.
- [8.2] Y. Bourezig, B. Bouabdallah, and F. Gaffiot, "Analysis of the resistivity in polysilicon thin film transistors study of film thickness effect," *Journal of Electrical and Electronic Engineering*, vol. 8, no. 2, pp. 733-738, 2008.
- [8.3] M. Adamschik, R. Müller, P. Gluche, A. Flöter, W. Limmer, R. Sauer, and E. Kohn, "Analysis of piezoresistive properties of CVD-diamond films on silicon," *Diamond and Related Material*, vol. 10, no. 9-10, pp. 1670-1675, 2001.
- [8.4] P. Hess, "The mechanical properties of various chemical vapor deposition diamond structures compared to the ideal single crystal," *Journal of Applied Physics*, vol. 111, no. 5, 2012.
- [8.5] O. a. Williams, a. Kriele, J. Hees, M. Wolfer, W. Müller-Sebert, and C. E. Nebel, "High young's modulus in ultra thin nanocrystalline diamond," *Chemical Physics Letters*, vol. 495, pp. 84-89, 2010.
- [8.6] M. A. Angadi and R. Whiting, "Longitudinal and transverse strain sensitivity of nichrome films," *Materials Science and Engineering B*, vol. 7, no. 1-2, pp. 1-4, 1990.
- [8.7] Online resource, <https://cleanroom.byu.edu/KOH>, accessed 14/07/2018

Chapter 9: Conclusions & Future Work

This body of work aimed to present the design, fabrication and characterization of polycrystalline diamond micro-electromechanical systems for passive micro-rheology and sensor applications.

One of the main achievements of this work is the fabrication process development presented. A common issue that limits the operation of micro-cantilevers fabricated from thin films is excessive undercut at the cantilever base [9.1]. By using a combination of top-side dry and wet etch processes, undercut has been minimized to less than 0.33 % of cantilever length in some devices. We present a cantilever with dimensions $L = 35 \mu\text{m}$, $W = 1 \mu\text{m}$ and $H = 0.48 \mu\text{m}$ which resonates in air at 555 kHz, comparable to a single crystal diamond cantilever reported by Kara *et al* of dimensions $L = 38 \mu\text{m}$, $W = 0.820 \mu\text{m}$ and $H = 0.530 \mu\text{m}$ which resonated in vacuum at 686 kHz [9.2].

The fabrication processes presented relating to boron-doped PCD devices provide a method for fabricating devices with integrated metal components that is compatible with silicon etching methods. The reported processes could prove to be a valuable resource for future PCD-based MEMS development [9.3].

The boron doped PCD cantilevers showed a relatively low deflection sensitivity of 0.029 mΩ/Ω-μm to 0.063 mΩ/Ω-μm. However, they are believed to be the first boron-doped PCD piezoresistive cantilevers fabricated from a single boron-doped layer of PCD [9.4]. This reduces the complexity of the material growth process.

This thesis also presents what is believed to be the highest width/length/height ratio micro-cantilevers reported of any material, having dimensions of $W = 1 \mu\text{m}$, $H = 0.4 \mu\text{m}$ and $L = 150 \mu\text{m}$. Linzon *et al* reported a silicon based micro-cantilever of dimensions $W = 16 \mu\text{m}$, $H = 5 \mu\text{m}$ and $L = 500 \mu\text{m}$ [9.5]. These devices could be relevant in studies where large amplitude deflection (relative to cantilever dimensions) devices are required.

It has been shown that the thermal fluctuations of intrinsic PCD micro-cantilevers can be characterized in a viscous medium at least up to the viscosity of water ($8.90 \times 10^{-4} \text{ Pa}\cdot\text{s}$). Other state-of-the-art micro-cantilever micro-rheometer devices rely on active electronics to drive the cantilever to resonance in order to overcome fluid dampening [9.6].

A verified data analysis method of extracting a fluids viscoelastic properties from the power spectrum of the damped thermal fluctuations of a submerged device is presented. This method reveals the fluid's viscoelastic properties across the entire frequency range of the measurement, up to the sample rate of the measurement system. Previously presented methods using micro-cantilevers merely use data at or around the resonant peak of actuated devices, and rely on multiple measurements in order to build up data spanning a frequency range [9.7]. In the absence of reliable raw data from the fabricated cantilevers owing to measurement system limitations, this method was verified using test data. However, this method could be universally applied and could be used as a resource for future researchers. The reliability of raw data could be increased by using a device with a higher signal-to-noise ratio, i.e. larger deflection amplitude from thermal fluctuations, or using a measurement system with a lower noise floor, preferably in a low noise environment.

Future Work

One of the main factors that was beyond the control of the author was diamond growth parameters. With the advent of CVD technology, thin diamond films can be tailored to specific purposes. A main focus for diamond growers is to achieve a high Young's modulus in order to maintain the favorable hardness of single crystal diamond [9.8]. However, there could be potential for a diamond thin film with a reduced Young's modulus. In boron-doped form, a reduced Young's modulus diamond thin film could be used to fabricate piezoresistive sensor devices that would deform more readily in response to microscopic forces. Such a device could still retain the same favorable thermal characteristics and chemical robustness as its stiffer counterparts. Similarly, a reduced Young's modulus PCD micro-cantilever micro-rheometer could exhibit greater out-of-plane displacement during thermal fluctuations. This would make the device more susceptible to fluid interaction, and the inherent restoring forces of the cantilever would be less likely to dominate the compound system. Increased displacement would also increase the signal-to-noise ratio in measurements.

The hydrophobicity of the diamond surface can be modified depending on the surface termination of the material [9.9]. The diamond used for this research is oxygen terminated and therefore exhibits hydrophilic behavior. In order to make the surface of the diamond hydrophobic the surface can be hydrogen terminated. Micro-cantilevers with hydrophobic and hydrophilic surfaces have been the subject of several studies and have been applied to evaluate the evaporation dynamics of water [9.10]. A device with the attractive material properties of diamond and tailored surface hydrophobicity could be the subject of further studies.

Ideally, a micro-rheometer device will have self-actuation and detection built in. This work has presented two separate devices that could potentially be combined in future research. A boron-doped PCD diamond micro-cantilever passive micro-rheometer with a piezo resistive detection mechanism could be realised following on from the disclosure presented herein. The potential for such a device, coupled with the ability to modify diamond material growth parameters leaves many potential future research paths wide open.

References

- [9.1] K. Gavan, E. W. J. M. van der Drift, W. J. Venstra, M. R. Zuiddam, H. S. J. van der Zant, "Effect of undercut on the resonant behavior of silicon nitride cantilevers," *Journal of Micromechanics and Microengineering*, Vol 19 No. 3, 2009
- [9.2] V. Kara, "Nano fluidics of Single-Crystal Diamond Nanomechanical Resonators," *Nano Letters*, 15 (12), pp 8070-8076 2015.
- [9.3] H.Jansen, H. Gardeniers, M. Boer, M.Elwenspoek, J. Fluitman, "A survey on the reactive ion etching of silicon in microtechnology," *Journal of Micromechanocs and Microengineering* Vol 6 pp. 14-28, 1996.
- [9.4] N. L. Privorotskaya, H. Zeng, S. Member, J. A. Carlisle, R. Bashir, and W. P. King, "Piezoresistive Microcantilevers From Ultrananocrystalline Diamond," *Journal of MEMS*, vol. 19, no. 5, pp. 1234-1242, 2010.
- [9.5] Y. Linzon, "Efficient parametric excitation of silicon-on-insulator microcantilever beams by fringing electrostatic fields" *Journal of Applied Physics* 113, 2013.
- [9.6] M. Youssry, B. Caillard, C. Ayela, C. Pellet, I. Dufour, and D. Int. Assoc. Sci. Technol, "Microrheology of Newtonian fluids using microcantilever," *NANA 2010*, pp. 540-546, 2016.
- [9.7] M. Papi, G. Maulucci, G. Arcovito, P. Paoletti, M. Vassalli, and M. De Spirito, "Detection of microviscosity by using uncalibrated atomic force microscopy cantilevers," *Applied Physics Letters*, vol. 93, no. 12, 2008.
- [9.8] O. A. Williams, A. Kriele, J. Hees, M. Wolfer, W. Müller-Sebert, and C. E. Nebel, "High young's modulus in ultra thin nanocrystalline diamond," *Chemical Physics Letters*, vol. 495, pp. 84-89, 2010.
- [9.9] M. Karlsson, P. Forsberg, F. Nikolajeff, "From Hydrophilic to Superhydrophobic: Fabrication of Micrometer-Sized Nail-Head-Shaped Pillars in Diamond," *Langmuir*, Vol 26 (2), pp 889-893, 2010
- [9.10] M. Lee, D. Lee, N. Jung, M.Yun, C. Yim, S. Jeona, "Evaporation of water droplets from hydrophobic and hydrophilic nanoporous microcantilevers," *Applied Physics Letters*, Vol 98, 2011.

Appendix A

MATLAB Code for Data Analysis

```
%This script plots the complex viscosity of a fluid from the
%power spectrum of the thermal fluctuations of a particle trapped in the
%fluid. To demonstrate, a test data set of an optically trapped 10um
%silica bead in water (trap stiffness 2.5 uN/m) is used and can be
%accessed here: http://dx.doi.org/10.5525/gla.researchdata.827
%This demonstration starts with performing an FFT on a time series. If
%data is already in FFT or PSD form then the FFT step can be skipped.
%Discussion of the theory used in this code can be found in Chapters 2 &
%7 of the thesis which this file accompanies.
%a.mcglone.1@research.gla.ac.uk.

oversampling=1;%oversampling factor: increase for more density in
autocorrelation
dpoints=250; %No. of points in autocorrelation function
K = 2.5; %trap stiffness micronewtons/m
rad = 10; %bead radius micrometers
scale = K/(6*pi*rad); %complex viscosity scaling factor
B = dlmread('k25rad10.txt', '\t'); %time series of trapped bead in water
gt = [B(:,1) B(:,2)];
D = B(:,2)-mean(B(:,2)); %subtract mean
Fx = (abs(fft(D))); %Fourier transform
PSRFx = Fx/length(Fx);
RFx = PSRFx(1:(length(PSRFx)/2)).^2; % create one sided PSD
torigx = gt(:,1)-gt(1,1) ;
dt = torigx(2);
maxfreq = 1/dt;
minfreq = 1/max(torigx);
freqfft = linspace(minfreq,maxfreq/2,length(RFx));
k = 1;
N = 2*length(RFx);
df= freqfft(2)-freqfft(1);
Fs = length(RFx)*df;
for k = 1:1:(N-1)/2
RFx(N+1-k)= conj(RFx(k+1)) ; % 1 <= k <= (N - 1)/2 create symmetrical PSD
end
tat = dt*(0:N-1);
A = N*ifft((RFx)); %Inverse fourier transform of symmetrical PSD
(autocorrelation)
NA =(A(2:end)./trapz(RFx)); %Normalise autocorrelation with PSD area
a=NA(1:dpoints); %Choose autocorrelation length
torig = linspace(dt,dt*dpoints,dpoints).';
t = linspace(dt,dt*dpoints,(dpoints*oversampling)-1).';
g = spline(torig, a, t);
GData = zeros(dpoints*oversampling,3);
frange = linspace(1/(torig(dpoints)),maxfreq,dpoints*oversampling);
g0 = 1;
eta = 0;
for ww = 1:dpoints*oversampling %this function performs fourier
transform on the autocorrelation function and multiplies by i*omega
w = frange(ww);
fta = ((1i*w*g0 + (1-exp(-1i*w*t(1)))*(g(1)-g0)/t(1) +
sum(diff(g)./diff(t).*(exp(-1i*w*(t(1:(size(t)-1)))))-exp(-
1i*w*(t(2:size(t)))))))/(-w.^2);
GStar = fta .* 1i*w ;
GData(ww,:) = [w real(GStar) imag(GStar)];
end
```

```

GTOT = complex(GData(:,2),(GData(:,3)));
GF = complex(GTOT./(1-GTOT)).*scale;
nF = (sqrt((real(GF).^2)+(imag(GF).^2))./frange. '); %Complex viscosity

figure('units','normalized','outerposition',[0 0 1 1])
subplot(2,1,2)
loglog(frang,nF,'-b')
ylim([0.0001 0.01])
xlabel('\omega(Rad.s)');
ylabel('\eta*(Pa.s)');
subplot(2,1,1)
semilogx(torig,a,'o')
hold on
semilogx(t,g,'x')
xlabel('t /s');
ylabel('A(t)');

```